TECHNICAL REPORT STANDARD TITLE PAGE

1. Report No.
FHWA/TX-92/1182-2

2. Government Accession No.

3. Recipient's Catalog No.

4. Title and Subtitle
Experimental and Analytical Study of a Two-Span Post-Tensioned Bridge Slab

5. Report Date
February 1992

Performing Organization Code

7. Author(s)
Roschke, P.N., Pruski, K.R., and Smith, C.D.

8. Performing Organization Report No.
Research Report 1182-2

9. Performing Organization Name and Address
Texas Transportation Institute
The Texas A&M University System
College Station, Texas 77843-3135

10. Work Unit No.

11. Contract or Grant No.
Study No. 2-5-88/0-1182

12. Sponsoring Agency Name and Address
Texas Department of Transportation
Transportation Planning Division
P. O. Box 5051
Austin, Texas 78763

13. Type of Report and Period Covered
Interim Report
September 1987-August 1991

14. Sponsoring Agency Code

15. Supplementary Notes
Research performed in cooperation with DOT, FHWA
Research Study Title: Evaluation of Factors Affecting Slabs Due to Localized Post-Tension Forces.

16. Abstract

This is the second in a series of reports documenting a research program aimed at detailed investigation of a new type of post-tensioned bridge structure that has a moderately thick concrete slab resting directly on columns without bent caps. In this program two scaled laboratory models, named Model 1 and Model 2, are tested along with instrumentation of a full-scale, three-span skewed bridge. This report deals with the second laboratory model.

A large, two-span 3/10ths scale model bridge is constructed and tested in the service, overload, and ultimate load ranges. Dimensions of the slab are 55.5 ft × 17.5 ft × 9 in. (16.9 m × 5.33 m × 0.229 m). In addition to uniformly distributed longitudinal post-tensioning, a band of tendons is placed in a narrow region directly above the supporting columns. Arrays of 185 strain gages, 18 LVDTs, 10 load cells, and 27 survey points serve to gather data for dead, live, and time-dependent loadings.

Response of the structure is studied in five stages. First, prestressing force and dead load are applied. Both short- and long-term effects of these loads are of interest. Special attention is given to the distribution of internal stresses due to transverse prestressing. Second, AASHTO design lane loads are applied statically to determine effectiveness of the transverse prestressing. Third, an AASHTO HS20-44 truck load is applied dynamically by means of a series of load actuators. Serviceability of the slab is checked for 200,000 cycles of the simulated truck. Fourth, a series of overloads are placed on the slab in a variety of critical locations. Lastly, ultimate loads are applied in the positive and negative bending moment regions followed by an ultimate shear load placed at the edge of the slab near the anchor heads of the transverse tendons. Complementary nonlinear finite element analyses of the dead, live, and time-dependent loadings provide confidence in the simulation capability of the code.

17. Key Words
Banded tendon, bridge, concrete, deflection, failure, finite element, plate, post-tensioning, prestressing, shear, slab, strain, transverse stressing

18. Distribution Statement
No restrictions. This document is available to the public through the
National Technical Information Service
5285 Port Royal Road
Springfield, Virginia 22161

19. Security Classif. (of this report)
Unclassified

20. Security Classif. (of this page)
Unclassified

21. No. of Pages
144

22. Price

Form DOT F 1700.7 (8-69)

Experimental and Analytical Study of a Two-Span Post-Tensioned Bridge Slab

by

Paul N. Roschke
Assistant Research Engineer

and

Kevin R. Pruski
Charles D. Smith
Graduate Research Assistants

Research Report 1182-2

on

Evaluation of Factors Affecting Slabs Due to Localized Post-Tension Forces
Research Study No. 2-5-88-1182

Sponsored by

Texas Department of Transportation

in cooperation with

The United States Department of Transportation
Federal Highway Administration

February 1992

Texas Transportation Institute
The Texas A&M University System
College Station, Texas 77843-3135

METRIC (SI*) CONVERSION FACTORS

APPROXIMATE CONVERSIONS TO SI UNITS

LENGTH

Symbol	When You Know	Multiply By	To Find	Symbol
in	inches	2.54	centimetres	cm
ft	feet	0.3048	metres	m
yd	yards	0.914	metres	m
mi	miles	1.61	kilometres	km

AREA

Symbol	When You Know	Multiply By	To Find	Symbol
in²	square inches	645.2	centimetres squared	cm ²
ft²	square feet	0.0929	metres squared	m²
yd²	square yards	0.836	metres squared	m²
mi²	square miles	2.59	kilometres squared	km²
ac	acres	0.395	hectares	ha

MASS (weight)

Symbol	When You Know	Multiply By	To Find	Symbol
oz	ounces	28.35	grams	g
lb	pounds	0.454	kilograms	kg
T	short tons (2000 lb)	0.907	megagrams	Mg

VOLUME

Symbol	When You Know	Multiply By	To Find	Symbol
fl oz	fluid ounces	29.57	millilitres	mL
gal	gallons	3.785	litres	L
ft³	cubic feet	0.0328	metres cubed	m³
yd³	cubic yards	0.0765	metres cubed	m³

NOTE: Volumes greater than 1000 L shall be shown in m³.

TEMPERATURE (exact)

Symbol	When You Know	Multiply By	To Find	Symbol
°F	Fahrenheit temperature	5/9 (after subtracting 32)	Celsius temperature	°C

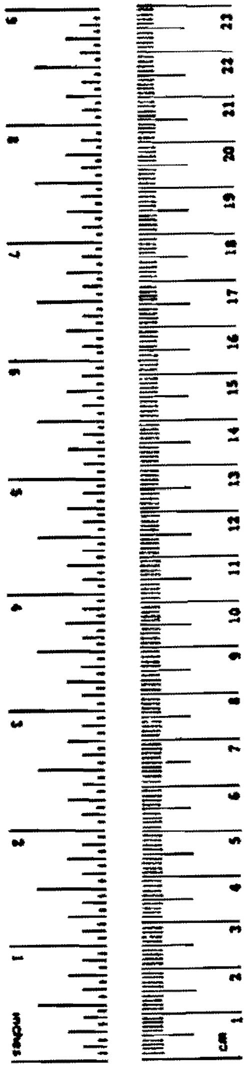

APPROXIMATE CONVERSIONS TO SI UNITS

LENGTH

Symbol	When You Know	Multiply By	To Find	Symbol
mm	millimetres	0.039	inches	in
m	metres	3.28	feet	ft
m	metres	1.09	yards	yd
km	kilometres	0.621	miles	mi

AREA

Symbol	When You Know	Multiply By	To Find	Symbol
mm²	millimetres squared	0.0016	square inches	in²
m²	metres squared	10.764	square feet	ft²
km²	kilometres squared	0.39	square miles	mi²
ha	hectores (10 000 m²)	2.53	acres	ac

MASS (weight)

Symbol	When You Know	Multiply By	To Find	Symbol
g	grams	0.0353	ounces	oz
kg	kilograms	2.205	pounds	lb
Mg	megagrams (1 000 kg)	1.103	short tons	T

VOLUME

Symbol	When You Know	Multiply By	To Find	Symbol
mL	millilitres	0.034	fluid ounces	fl oz
L	litres	0.264	gallons	gal
m³	metres cubed	35.315	cubic feet	ft³
m³	metres cubed	1.308	cubic yards	yd³

TEMPERATURE (exact)

Symbol	When You Know	Multiply By	To Find	Symbol
°C	Celsius temperature	9/5 (then add 32)	Fahrenheit temperature	°F

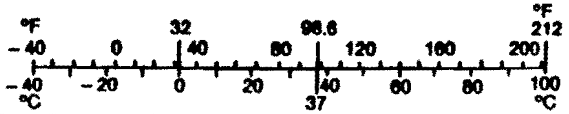

These factors conform to the requirement of FHWA Order 5190.1A.

---

* SI is the symbol for the International System of Measurements

ABSTRACT

This is the second in a series of reports documenting a research program aimed at detailed investigation of a new type of post-tensioned bridge structure that has a moderately thick concrete slab resting directly on columns without bent caps. In this program two scaled laboratory models, named Model 1 and Model 2, are tested along with instrumentation of a full-scale, three-span skewed bridge. This report deals with the second laboratory model.

A large, two-span 3/10$^{\text{ths}}$ scale model bridge is constructed and tested in the service, overload, and ultimate load ranges. Dimensions of the slab are 55.5 ft × 17.5 ft × 9 in. (16.9 m × 5.33 m × 0.229 m). In addition to uniformly distributed longitudinal post-tensioning, a band of tendons is place in a narrow region directly above the supporting columns. Arrays of 185 strain gages, 18 LVDTs, 10 load cells, and 27 survey points serve to gather data for dead, live, and time-dependent loadings.

Response of the structure is studied in five stages. First, prestressing force and dead load are applied. Both short- and long-term effects of these loads are of interest. Special attention is given to the distribution of internal stresses due to transverse prestressing. Second, AASHTO design lane loads are applied statically to determine effectiveness of the transverse prestressing. Third, an AASHTO HS20-44 truck load is applied dynamically by means of a series of load actuators. Servicability of the slab is checked for 200,000 cycles of the simulated truck. Fourth, a series of overloads are placed on the slab in a variety of critical locations. Lastly, ultimate loads are applied in the positive and negative bending moment regions followed by an ultimate shear load placed at the edge of the slab near the anchor heads of the transverse tendons. Complementary nonlinear finite element analyses of the dead, live, and time-dependent loadings provide confidence in the simulation capability of the code.

DISCLAIMER

The contents of this report reflect the views of the authors who are responsible for the opinions, findings, and conclusions presented herein. The contents do not necessarily reflect the official views or policies of the Texas Department of Transportation. This report does not constitute a standard, specification, or regulation; it is not intended for construction, bidding, or permit purposes.

The engineer in charge of this project is Dr. Paul N. Roschke, who is a registered professional engineer in the State of Texas (Serial Number 53889).

KEYWORDS

Banded Tendon, Bridge, Concrete, Deflection, Failure, Finite Element, Plate, Post-Tensioning, Prestressing, Shear, Slab, Strain, Stress, Transverse Stressing

ACKNOWLEDGMENTS

This study was conducted under a cooperative program between the Texas Transportation Institute, the Texas Department of Transportation, and the Federal Highway Administration. Randy Cox and Tim Bradberry worked closely with the researchers, and their comments and suggestions are appreciated.

IMPLEMENTATION STATEMENT

This report concentrates on one phase of a large study and needs to be read in the context of the other companion reports. Emphasis here is on a laboratory study of a large-scale model bridge. Complementary work on a field bridge that was instrumented with transducers and a special finite element code (see reports 1182-1, 1182-3, and 1182-4) will be helpful to design engineers.

Results of this study are available for immediate implementation by the Texas Department of Transportation.

TABLE OF CONTENTS

Page

LIST OF FIGURES

LIST OF TABLES

1. INTRODUCTION

1.1 Background

In recent years prestressed concrete structures have become increasingly popular. Reasons for this popularity include minimum maintenance, increased durability, and good aesthetics (Naaman 1982). One common type is a composite, prestressed girder and reinforced concrete slab bridge, which is typically used on highway overpasses for spans ranging from 40 to 150 ft (12.2 to 45.7 m). Typical cross-sections have depths ranging from 36 to 72 in. (91.4 to 182.9 cm). However, when clearance beneath the structure is coupled with approach considerations such as cost of embankment material or excessive side slopes stemming from existing roadways, the allowable depth of cross-section may be considerably less than that required to span between the supports, see Figs. 1 (a) and (b).

One solution to this problem is to eliminate the simple-span prestressed girders and substitute a continuous prestressed slab that provides the required moment capacity while decreasing the depth of the cross-section. This not only allows additional clearance but also creates a more aesthetic structure. To further enhance appearance the bent cap may be removed, as it is no longer needed to support girders between columns in the transverse direction - across the width. As a result the slab rests directly on the columns and is cushioned by reinforced neoprene bearing pads. However, this complicates design since the slab can no longer be considered one-way in the vicinity of the columns.

One such structure, that has been designed and built by the Texas Department of Transportation (TxDOT), is the Taft Street overpass in Wichita Falls, Texas. The current design consists of a cast-in-place, post-tensioned slab with uniformly distributed prestressing in the longitudinal direction, and banded prestressing in the transverse direction at the column lines, in lieu of support provided by bent caps, as shown in Fig. 2. The longest span length is 94.5 ft (28.8 m).

1.2 Current Design Method

In order to design the slab for a bridge of this type, TxDOT designers use the following simplifications. First, effects of skew are neglected and a strip method in conjunction with equivalent loads for the prestressing (load balancing) is used to analyze the structure in the longitudinal direction. A continuous strip from abutment to abutment is used in the analysis. Second, to analyze the banded prestressed region, a wedge-shaped stress distribution is assumed, see Fig. 3, and average stress due to post-tensioning is calculated at critical cross-sections in this area. A conventional slab analysis program is then used to calculate transverse stresses due to vertical dead and traffic loads. In-plane and bending stresses are superimposed to arrive at the necessary design stress values.

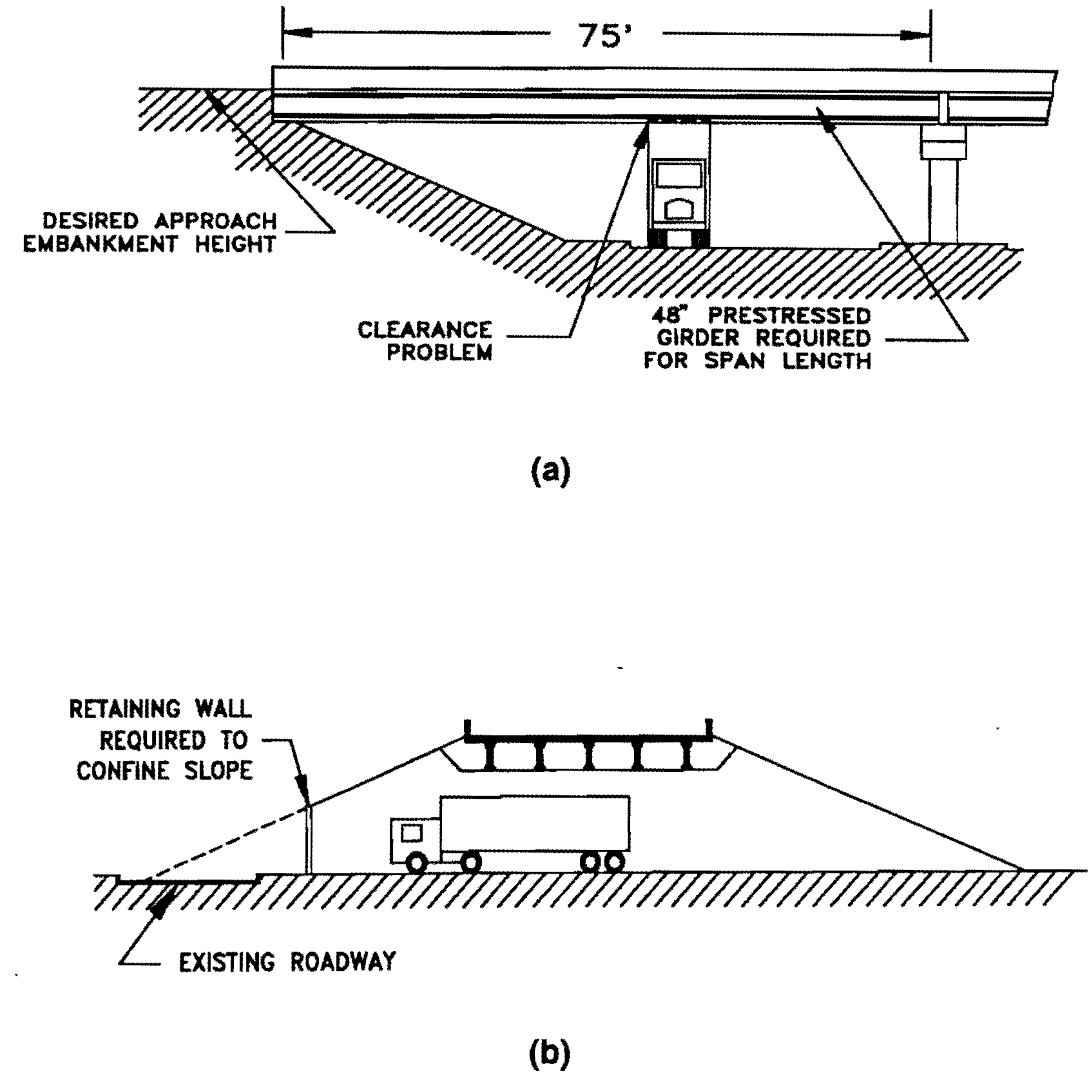

FIG. 1. Design Considerations that Reduce Allowable Section Depth: (a) Approach Embankment; (b) Existing Roadway

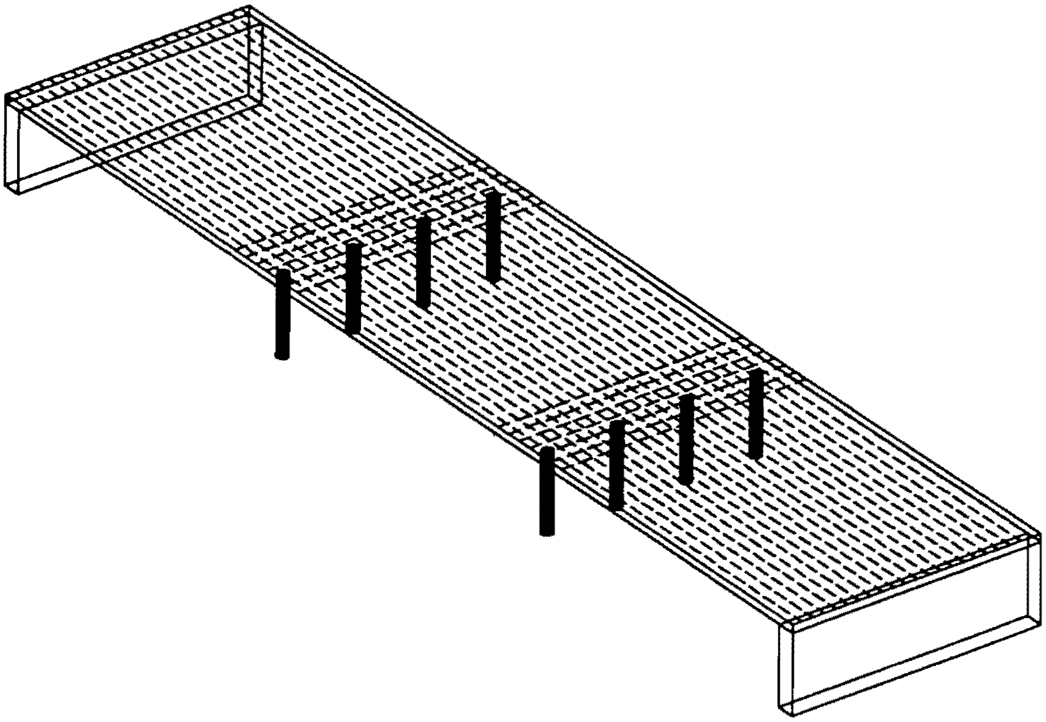

FIG. 2. Thin Slab Bridge with Banded Transverse Prestressing

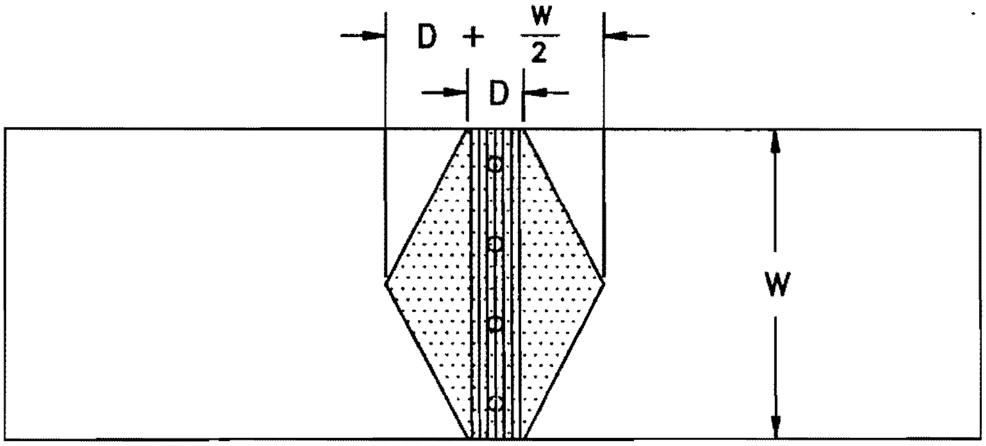

D = TENDON NUMBER x SPACING
W = SLAB WIDTH

FIG. 3. Assumption for Stress Distribution in Approximate Design Approach

Both simplifications result in some analytical error. First, the strip method inaccurately depicts the deflected shape and, consequently, the longitudinal stress distribution across the width of the slab. This error is due to assumed one-way plate action as opposed to the actual two-way plate action, and in the presence of skew, the error may become quite significant. Second, the transverse stress distribution caused by banded prestressing is more complex than assumed, and averaging stress over the region does not accurately depict its continuous nature. Therefore, predicted in-plane stress is higher than that of the actual structure at some points in the cross-section and lower at others (Roschke and Inoue 1990). Third, in order to apply these methods separately, a uniaxial state of stress must be assumed in each direction. It is known that concrete under biaxial stress has a higher strength than that under uniaxial stress (Kupfer, Hilsdorf, and Rusch 1969), which allows higher stress to be developed before failure occurs than is predicted by uniaxial analysis.

In the absence of an analytical tool that incorporates these concepts, the designer must apply a large degree of uncertainty and, consequently, may arrive at a very conservative design.

1.3 Review of Literature

To the best of the authors' knowledge there has not been, to this date, any experimental or analytical work accomplished on post-tensioned bridge decks with banded prestressing steel. There are, however, many publications dealing with factors germane to this study. A number of these contributions are discussed in what follows.

American Concrete Institute - American Society of Civil Engineers Committee 423 (ACI 1974) has suggested guidelines for post-tensioned flat plate design in buildings based primarily on tests and experience with unbonded tendons. It is maintained that these recommendations are applicable to bonded tendons as well. The load balancing procedure in conjunction with the equivalent frame method is noted as an accepted method of analysis. Allowable stresses are set for the equivalent frame method of analysis. These may be relaxed if a more rigorous method of analysis, such as elastic plate theory or finite elements, is used.

It is recommended that for continuous spans, 65 to 75% of prestressing tendons be placed in the column strip as defined in the Commentary to ACI 318-71 (ACI Specification 1971) and the rest in the middle strip (Lin, Scordelis, and Itaya 1959). Suggested maximum spacing of the tendons in the column strips and middle strips is four and six times the slab thickness, respectively. For shearing stress the more critical of two conditions should be considered: (1) the plate acts as a wide beam, or (2) two-way action causes diagonal cracks around a perimeter of the load or reaction. The latter is more likely for the bridge slab under consideration, due to the presence of high concentrated loads.

A minimum average normal stress, total prestressing force divided by total area of concrete, of 200 to 250 psi (1380 to 1725 kPa) is recommended to minimize cracking. To avoid excessive elastic shortening and creep the maximum recommended prestress is 500 psi (3,450 kPa). This does not apply to the class of slabs in question for this study since the long spans necessitate larger prestressing forces to offset flexural stresses. ACI-ASCE does not extend these guidelines to bridge slabs. This is reasonable since loading and design objectives of bridges differ greatly from that of typical flat slab structures.

Burns and Hemakom (1985) tested a 1/2-scale post-tensioned flat plate designed in accordance with the previous guidelines along with standard industry practice of banded tendons. The model had banded tendons in one direction, and uniformly distributed tendons in the other direction. It performed well at service and ultimate loads, with cracks occurring across the uniformly distributed tendons in all cases. Applied loads were uniform in nature, and, therefore, not consistent with loadings that occur on bridge decks.

Kupfer, Hilsdorf, and Rusch (1969) report strengths of concrete subjected to biaxial compression as high as 27% greater than the uniaxial strength in tests utilizing brush platens to apply various combinations of biaxial stress. An analytical method utilizing equivalent uniaxial stress-strain curves that reflect the increase in strength due to biaxial loading compares favorably with the experimental values determined by Kupfer et al. (Darwin and Pecknold 1977). This method is incorporated in the analysis program used in this study.

It is recognized that fatigue strength of concrete members is an important consideration when designing structures that experience repeated loads. ACI Committee 215 (ACI 1974) provides information intended to guide the engineer confronted with this situation. Su and Hsu (1988) also studied this behavior, refining the results given by ACI. This information is discussed in Section 7.3.

In order to gain information on the durability of post-tensioned bridge decks Poston, Carrasquillo, and Breen (1987) conducted a series of tests on concrete specimens exposed to corrosive environments. They found that prestressing is beneficial in controlling corrosion when it is used to prevent cracking.

1.4 Scope of Study

To aid the engineer in designing post-tensioned flat slab bridges an analytical tool that will accurately predict structural response is verified by experiment. Also, physical phenomena which occur due to prestressing are studied to determine their effects on this type of structure. The experimental program for this project consists of three phases:

1. A section of the structure is modeled (Model 1) to study effects of varying the number of transverse prestressing tendons, and to determine punching shear strength (Roschke and Inoue 1990).
2. A large scale model (Model 2) is built in the Structures and Materials Laboratory at Texas A&M University, to study stress distribution, structural response to design loads, and physical phenomena characteristic of concrete in a controlled environment. Effects of large environmental variations such as temperature and humidity are eliminated, and loads may be applied more accurately and with greater variation than in the field.
3. An actual bridge under construction in Wichita Falls, Texas is instrumented in order to study stress distribution, structural response to live load, and physical phenomena characteristic of concrete in a full-size structure (Roschke, Pruski, and Sripadanna 1992).

The second phase is the subject of this report.

Response of the laboratory model to loads is studied in four stages. First, prestressing force and dead load are applied. Both short-term and long-term effects of these loads are of interest. Of primary interest in this stage is the distribution of internal stresses due to the transverse prestressing. Second, American Association of State Highway and Transportation Officials' (AASHTO) HS20-44 design lane loads (*Standard* 1989) are applied statically to determine effectiveness of the transverse prestressing in replacing the bent cap. Third, an AASHTO HS20-44 truck load is applied dynamically to study the serviceability of the slab in the region of large stress gradients that are adjacent to the transverse prestressing. This effect, known as shear lag, may induce cracking or affect fatigue strength of the structure. Finally, a series of overload and ultimate loads are placed in various locations on the slab.

Important physical phenomena that are characteristic of concrete are shrinkage and creep. Loss of excess water through evaporation leads to a gradual shortening of concrete with time, which is termed shrinkage. Creep is an increase in strain with time, in excess of elastic strain, due to sustained load. Shrinkage and creep of concrete result in a loss of prestressing force which must be accounted for in the analysis and design (Naaman 1982). However, creep is potentially more damaging since it may result in undesirable deformation of the structure such as camber. Differential creep in the vicinity of the banded prestressing may induce unwanted stresses not accounted for in the design. Laboratory modeling of shrinkage and creep behavior is practically impossible due to greatly reduced thicknesses, which means that moisture conditions cannot be modeled. The best that can be expected is that basic behavior may be qualified (Zia, White, and Van Horn 1970).

Strain and displacement measurements are taken in order to study the response of the structure to loading and these phenomena. The data also serves to verify the analysis program (Roschke and Pruski 1992). Instrumentation is also discussed. Results from use of the finite element method (FEM) are reported where appropriate.

2. DESCRIPTION OF MODEL

When constructing scale models of structures two approaches may be utilized. One is indirect modeling, in which the loading does not necessarily match that of the real structure, or prototype. This type of modeling is useful for studying linear behavior. On the other hand, direct modeling, in which the loading is applied as it would be on the prototype, is useful in studying behavior of a structure up to and including failure (Preece and Davies 1964). The latter approach is used in this study.

2.1 Scale and Similitude

Two important factors that must be considered when designing a direct model are scale and similitude. As the relative size, or scale, of the model to the prototype decreases, it becomes more difficult to relate results of the model test to the prototype (Zia, White, and Van Horn 1970). Therefore, it is desirable to use the largest scale possible. In this study Model 2 is, in essence, a three-tenths scale, direct model of Taft Street overpass (see Fig. 4). However, due to limitations of laboratory facilities the model is a two-span structure rather than three spans as in the prototype. Two spans are satisfactory for purposes of verifying the analysis procedure and studying effects of the banded prestressing; in this sense Model 2 itself can be considered a prototype. A span-to-depth ratio of 37 is used for each span, which corresponds to the maximum span length of Taft Street overpass. Although the prototype has a slight skew, 6.6°, this is not considered in the model to avoid special complications and simplify construction.

Similitude is the process by which geometry and material properties of the model are related to the prototype. In theory all dimensionless products of the model should be equivalent to those of the prototype and, thus, scale factors may be calculated to relate model and prototype measurements (Preece and Davies 1964).

Strain, a dimensionless quantity, in the model must equal strain in the prototype by definition of a direct model. Also, desire to study time-dependent effects in this model makes it prudent to use the same material in the model as in the prototype due to the fact that these effects are very dependent on material. In this case, 5,000-psi (34,500-kPa) design 28-day compressive strength concrete is the primary material used in the model and prototype slabs. Thus, elastic moduli of materials are of equal magnitude. Combining these two relations results in a scale factor of 1.0 for stresses.

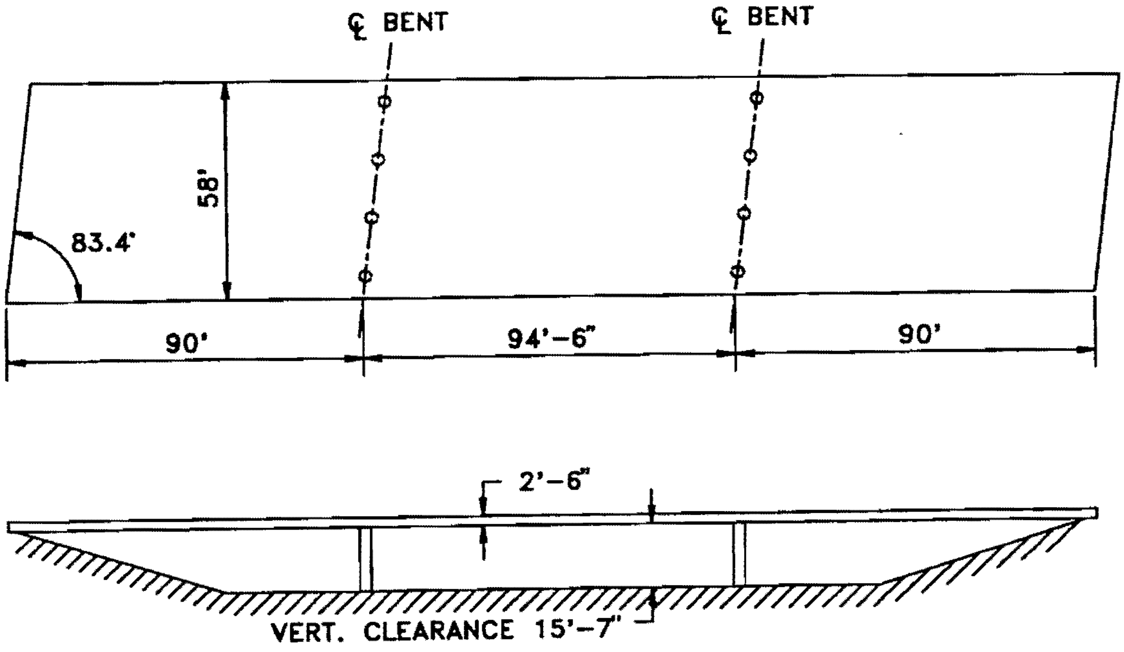

FIG. 4. Taft Street Overpass

These and other relations needed in this study are shown in Eqs. 1-9, where subscripts m and p indicate the model and prototype, respectively (Preece and Davis 1964).

(a) strain

$$\varepsilon_m = \varepsilon_p \qquad (1)$$

(b) elastic moduli

$$E_m = E_p \qquad (2)$$

Combining Eqs. 1 and 2 gives Eq. 3:

(c) stress

$$E_m (\varepsilon_m) = E_p (\varepsilon_p) \qquad (3)$$

or

$$\sigma_m = S_f (\sigma_p) \qquad (4)$$

giving $S_f = 1.0$, where S_f is the stress scale factor.

(d) geometry

$$L_m = S_L (L_p) \quad \text{.......} \quad (5)$$

where L_m and L_p are length dimensions, and $S_L = 0.3$ is the geometric scale factor.

(e) density

$$\rho_m = \frac{S_f}{S_L} (\rho_p) \quad \text{.......} \quad (6)$$

(f) uniformly distributed load

$$p_m = S_f (p_p) \quad \text{.......} \quad (7)$$

(g) point load

$$P_m = S_L^2 (P_p) \quad \text{.......} \quad (8)$$

(h) velocity

$$v_m = S_L^{0.5} \frac{1}{S_L} (v_p) \quad \text{.......} \quad (9)$$

The geometric scale factor, $S_L = 0.3$, is chosen primarily for convenience along with the desire to achieve as large a model as possible within laboratory limitations. These include loading frames and actuators, floor connections, and floor space.

Geometric similitude is applied to the model with the following exceptions. It has been shown that aggregate having different material properties also have different time-dependent characteristics. This is also true for aggregates of the same material having different maximum aggregate size (Troxell, Raphael, and Davis 1958). In order to observe geometric similitude for the concrete aggregate, a 1/4-in. (6-mm) maximum aggregate size would be needed. However, local commercially available aggregate of this size has considerably different characteristics from the 3/4-in. (19-mm) limestone used in the prototype. Therefore, 3/4-in. (19-mm) limestone is used for aggregate in the model. It is noted that some sacrifice in accuracy of the ultimate strength is often experienced due to this relaxation of similitude (Alami and Ferguson 1963). Also, diameter of each support column is slightly less than a true 3/10ths scale model to accommodate ease of forming. This does not create any problems because the bearing pad is the actual supporting member and it has the correct scaled dimension. Lastly, the diameter of passive reinforcement required to meet similitude is 3/16 in. (4.8 mm), which is not a readily available size of deformed bar. In view of the fact that the passive reinforcement is not of major structural significance, this requirement has been relaxed. Instead of scaling the size of each individual bar, the ratio of steel-to-concrete of the model is made to be equivalent to that of the prototype.

An important consideration in the design of the scale model is the scale factor for material density, as shown in Eq. 6, $S_f/S_L = 3.333$. Since concrete is the material for the model as well as the prototype, this relation can not be achieved. Therefore, additional load must be applied to the slab to compensate for this discrepancy. In the case of Model 2, dead load blocks equivalent to 21 in. (53.3 cm) of uniformly distributed concrete are suspended from the slab at 2-ft (0.6-m) intervals. This corresponds to the thickness of the prototype minus that of the model.

2.2 Model Summary

The model slab is 55-ft (16.8-m) long, 17.5-ft (5.33-m) wide, and 9-in. (22.9-cm) thick. As mentioned previously this coincides with the span-to-depth ratio of the maximum span length of the prototype. The slab is supported by abutments at the ends, and four 10-in. (25.4-cm) diameter columns spaced 4.5 ft (1.4 m) on center and located 27.75 ft (8.5 m) from each end. Support height is 5.3 ft (1.6 m) to allow placing of compensating dead load, and observance of cracks which may occur during testing. Each bearing surface is cushioned by a neoprene pad. Longitudinal prestressing is provided by 40 seven-wire strands that are 0.6-in. (1.5-cm) in diameter and spaced 5.125 in. (13.0 cm) on center. Transverse prestressing is provided by 7 of the same size strands spaced 5.4 in. (13.7 cm) on center. #3 reinforcing bars are used top and bottom for passive reinforcement, spaced 14.4 and 7.2 in. (36.6 and 18.3 cm) on center in the longitudinal and transverse directions, respectively. Post-tensioned grouted construction is used. Table 1 shows a comparison of prototype and model properties.

2.3 Model Design Details

Design of the model slab involves applying two scale factors to the prototype: those of geometry and stress, 0.3 and 1.0, respectively. All dimensions of the model, including tendon eccentricity, are scaled from the prototype with the three exceptions mentioned previously.

TABLE 1. Comparison of Properties of Prototype and Model 2

Description (1)	Prototype (2)	Model True 3/10ths scale (3)	Model As built (4)
Width, ft	58	17.4	17.5
Span, ft	94.5	28.35	27.75
Thickness, in.	30	9	9 0.125
Column diameter, in.	36	10.8	10
Bearing pad			
diameter, in.	33	9.9	9.75
thickness, in.	1.75	0.525	0.5
Passive reinforcement			
A_s/A_c ratio, %			
longitudinal	0.17	0.17	0.17
transverse	0.34	0.34	0.34
f_{pci} at anchor, psi			
longitudinal	955	955	860
transverse	930	930	782
f_{ci}', psi	3,500	3,500	6,200
$f_c'(28)$, psi	5,000	5,000	6,500
Dead load, psf	362.5	362.5	108.75
Dead load compensation, psf	——	——	253.75

[a]Actual strength
[b]Design strength
Note: 1 in. = 25.4 mm; 1 psi = 6.89 kPa; 1 psf = 48 Pa

Design of prestressing force in the prototype results in an average longitudinal compressive stress of 955 psi (6,590 kPa) in the concrete at the anchors. However, an error in interpretation of the original design calculations lead to use of 860 psi (5,934 kPa), a 10% reduction. This stress is used to determine the number of prestressing tendons required in the longitudinal direction. Applying the scale factor for stress requires that stress in the model is also 860 psi (5,934 kPa). Prestressing force in the transverse direction of the prototype results in an average concrete stress of 930 psi (6,417 kPa) within the width *D* (see Fig. 3) at the anchor heads. Again, a lower stress of 782 psi (5,396 kPa) is used due to an error in interpretation of an original design calculation.

Prestressing is achieved using a 0.6-in. (1.524-cm) diameter, 270-ksi (1,863-MPa) monostrand assembly. The ratio of prestressing steel area to concrete area is consistent with that of the prototype. Primary reason for the choice of this assembly is availability of materials. In addition, use of a monostrand instead of a multistrand tendon allows for smaller encasing ducts, which minimizes the area of grout in the cross section. Flexible metal conduit with an inside diameter of 0.75 in. (1.9 cm) is used for the ducts. This type of duct is chosen because its ribbed construction gives good bonding characteristics upon grouting. Grout openings are provided by 1/4-in. (6.35-mm) PVC pipe extending vertically out of the slab from a T joint at the tendon duct. These openings are located at the ends and the high point of each tendon profile. The anchor chosen is comprised of a 3.5 × 5.5 × 1/2-in. (8.89 × 13.97 × 1.27-cm) steel bearing plate with a separate anchor head in which the wedges grip the single prestressing strand (Fig. 5).

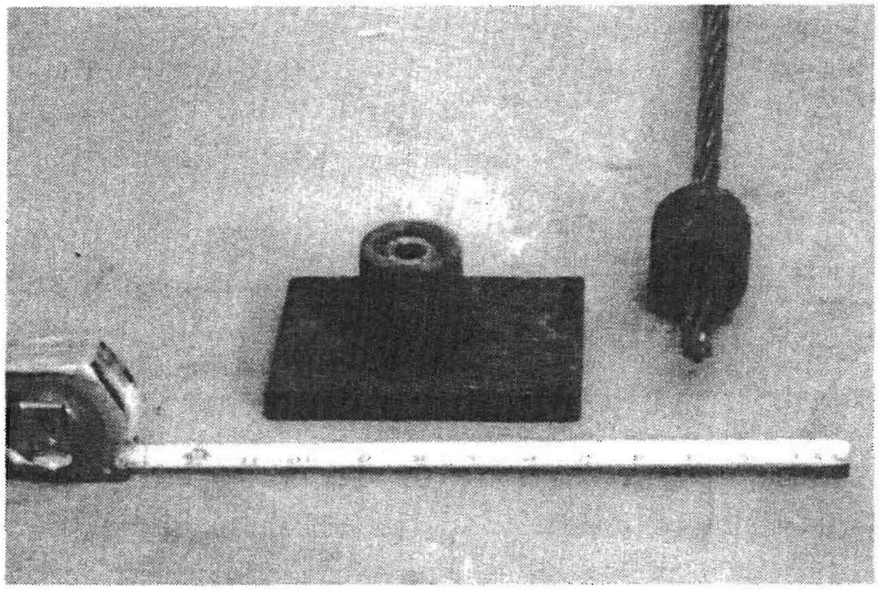

FIG. 5. Prestressing Anchor Assembly

AASHTO section 9.15.1 (*Standard* 1989) recommends an allowable stress of 0.70 f_{pu} or 189 ksi (1,304 MPa) at seating for stress-relieved strand. This corresponds to a force of 41.0 kips (184.6 kN). Therefore, to achieve design longitudinal prestressing, 40 tendons with a 5.125-in. (13.02-cm) center-to-center spacing are required.

In the prototype 7 tendons at a spacing of 18 in. (45.72 cm) are used to achieve prestressing in the transverse direction. Since the primary objective of this project is to study the effects of these transverse tendons, the same configuration is used for the model. Applying the geometric scale factor gives 7 tendons spaced at 5.4 in. (13.7 cm). The necessary prestressing force for the model is 38.0 kips (171 kN).

The layout of the tendons and the longitudinal profile are shown in Fig. 6. Transverse tendons are straight and lie in the middle plane of the slab.

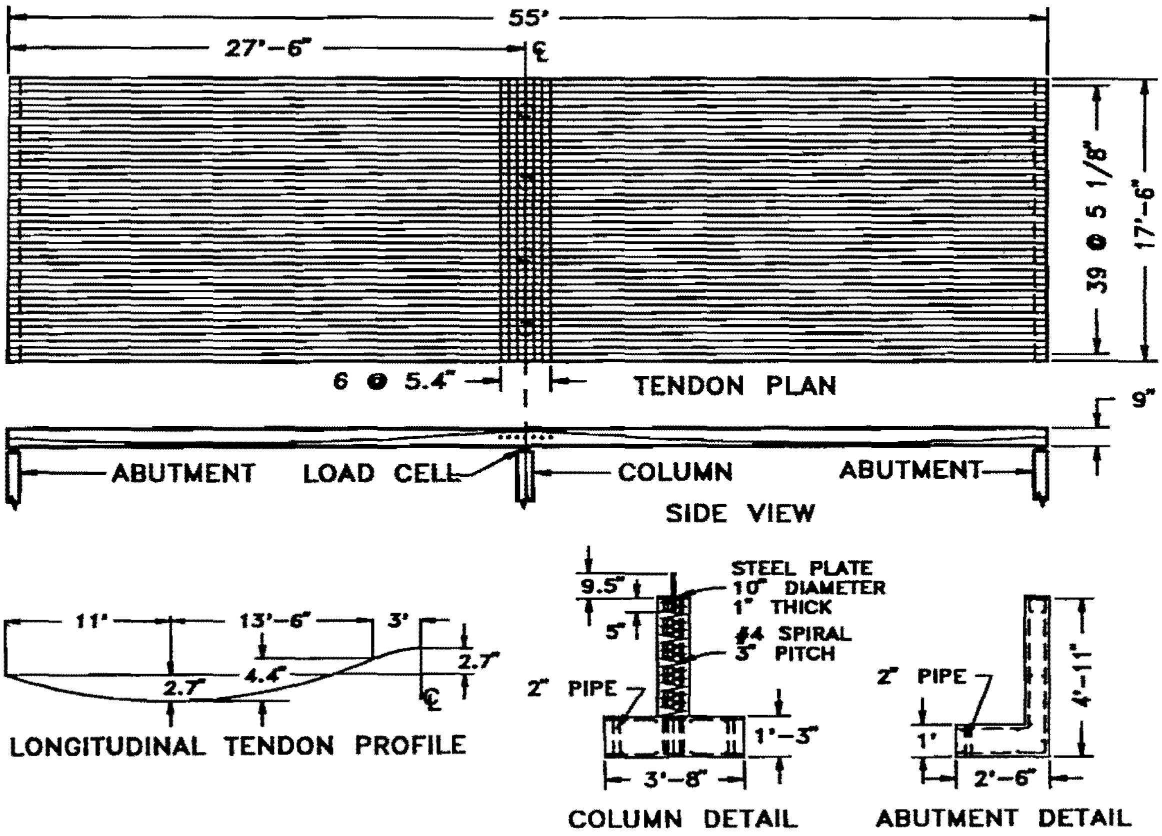

FIG. 6. Model 2 Overall Dimensions and Tendon Plan

Bearing stress due to prestressing at the anchor is of concern due to the possibility of spalling or bursting. Recent studies by Burdet (1990) and Breen et al. (1991) suggest that the effective concrete bearing compressive strength f_b used for design shall not exceed the following:

$$f_b \leq 0.7\phi f'_{ci}\sqrt{\frac{A}{A_g}} \quad \text{.......... (10)}$$

but

$$f_b \leq 2.25\phi f'_{ci} \quad \text{.......... (11)}$$

where f_b = maximum factored tendon load, P_u, divided by the effective bearing area A_b; f'_{ci} = concrete compressive strength at stressing; A = maximum area of the portion of the supporting surface that is geometrically similar to the loaded area and concentric with it; A_g = gross area of the bearing plate; and A_b = effective net area of the bearing plate calculated as the area A_g minus the area of openings in the bearing plate. Using the design values for material properties, tendon forces, and anchorage geometry leads to an estimated bearing stress in the concrete of 3.23 ksi (22.3 MPa), which is less than the critical values given by Eqs. 10 and 11.

Burdet (1990) also developed the following equation to estimate bursting force due to a single post-tensioned tendon:

$$T_{burst} = 0.25P(1-\frac{a}{h}) + 0.5P\sin\theta \quad \text{.......... (12)}$$

where P = the total factored tendon load; a = lateral dimension of the anchorage device; h = lateral dimension of the cross section; and θ = angle of inclination of the resultant of the tendon with respect to the centerline of the member. To guard against these bursting forces, additional reinforcing steel is placed near the anchorages: a #3 reinforcing bar is located above and below the anchorage horizontally, and between each anchorage vertically. The extra steel is positioned at the point of maximum tensile stress (Guyon 1953), approximately 3-in. (7.6-cm) from the anchor.

Also of concern is the location of the grout openings, which could create a stress concentration leading to crack development. Tests on a block of concrete with a section of prestressing duct embedded in it, and grout openings placed 6 in. (15.2 cm) from the bearing surface show no adverse effects. Therefore, this configuration is used.

Passive reinforcement in the prototype is provided by #5 reinforcing bars placed approximately 12 in. (30.5 cm) on center in the longitudinal direction and 6 in. (15.2 cm) on center in the transverse direction. This gives A_s/A_c ratios of 0.17% and 0.34%, respectively. As discussed previously this ratio is held in the model, resulting in #3 bars placed 14.4 in. (36.6 cm) on center longitudinally and 7.2 in.

(18.3 cm) on center transversely. For convenience, two 20-ft (6.1-m) bars and one 16-ft (4.9-m) bar are used to form the longitudinal reinforcement. A 12-in. (30.48-cm) lap splice located equidistant from bordering strain gage locations is used to link the bars together.

Columns are designed as prototype members in accordance with AASHTO specifications, i.e. exact scaling is not used as discussed previously. They are 10-in. (25.4-cm) in diameter with 5,000-psi (34,500-kPa) concrete and 10 vertical #4 reinforcing bars enclosed in a #4 spiral with a 3-in. (7.6 cm) pitch. The column-slab connection is provided by a 1-in. (2.54-cm) diameter bar which is not bonded to the slab. A footing is provided to fasten the column bent to the floor. Development length of the column reinforcement is the governing dimension for thickness of the footing. Four holes are provided, through which the footing is fastened to the laboratory floor with 1-in. (2.54-cm) diameter bolts. Minimum reinforcement for shrinkage and temperature is provided in the footing.

Abutments are designed as bearing walls in accordance with ACI specifications. They consist of a 8 × 210 × 60-in. (20.3 × 533.4 × 152.4-cm) wall of 5,000-psi (34,500-kPa) concrete with minimum reinforcement provided for shrinkage and temperature. Footings for the abutments are provided as per the columns. Again development length of reinforcement is the governing dimension. Two holes are provided for fastening each abutment to the floor. See Fig. 6 for details of columns and abutments.

Bearing pads at the columns supply the critical dimension to provide model similitude. They are 9.75-in. (24.77-cm) in diameter by 0.5-in. (1.27-cm) thick. Three elastomeric pads and two steel pads are alternately bonded together to create one reinforced bearing pad.

Bearing pads at the abutments have no affect on the behavior of the structure at the region of banded prestressing, and no special design consideration is given to them. An unreinforced elastomer supported by a continuous steel plate is used at this location.

3. INSTRUMENTATION AND DATA COLLECTION

Concrete strains are measured by attaching electrical resistance foil strain gages with a 0.24-in. (6.0-mm) gage length directly to the passive reinforcing bars at an array of locations as shown in Fig. 7. Gages are oriented in both the longitudinal and transverse direction in the top and bottom of the slab with the exception of locations 21, 26, and 46. At these locations additional strain gages are attached to short sections of rebar and tied into the top steel mat at an angle of 63.4° that matches two intersections of reinforcing bars. This is done to create a rosette configuration for calculating shearing strain. Location 46 has gages only on the top steel. Gages are arranged in this configuration to provide a large amount of redundancy in case of destruction during construction of the slab. Also, spacing is reduced in close proximity to the region of banded tendons to record the transition of strain from compression to tension as is expected. Additionally, extensometer points are embedded in the surface of the concrete at location 46 in the longitudinal and transverse directions to measure initial shrinkage, and to check the foil gages. A total of 185 foil gages and 3 extensometer points are embedded in the slab.

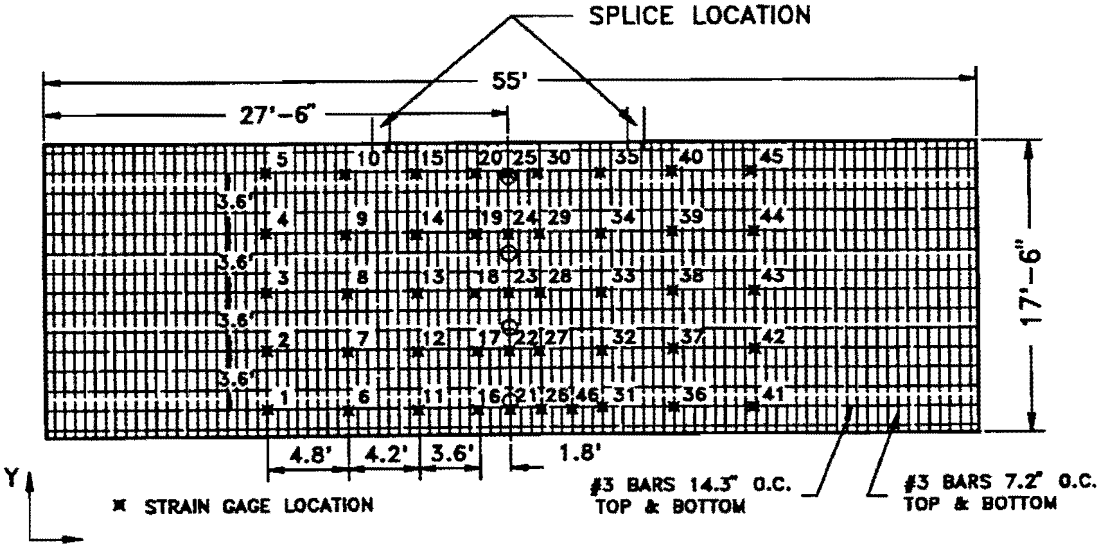

NOTES:
1. STRAIN GAGES ATTACHED IN X & Y DIRECTION TO TOP & BOTTOM REINFORCEMENT AT EACH LOCATION
2. STRAIN GAGE LAYOUT SYMMETRIC ABOUT CENTER LINE

FIG. 7. Strain Gage Locations

In order to gain some knowledge of the frictional characteristics of the prestressing duct, foil gages are also attached to two tendons, one located at the center line of the slab and the other 59 in. (150 cm) from the edge. Gage locations are 3 ft (0.9 m) from the jacking end of the first tendon, and 20 ft (6.1 m) from the jacking end of the other. Three gages are placed on the individual wires at each location. Application and protection is the same as for a deformed bar (see Sec. 3.1), with the exception of grinding the surface. Testing is conducted on a short length of a prestressing strand using a 0.062-in. (1.57-mm) strain gage and a 0.24-in. (6.0-mm) strain gage. Strain data are almost identical for both lengths, and the 0.24-in. (6.0-mm) gage is selected. Results of these tests are discussed later.

Displacements are measured using a total of 18 linear variable differential transformers (LVDTs). They are placed three abreast at each quarter point of the slab spans. Vertical deflection is also measured to the nearest 0.001 ft (0.0003 m) by surveying elevation implants embedded in the top of the slab (see Fig. 8).

Reactions at the supports are measured with 50-kip (225-kN) load cells placed between 1-in. (2.54-cm) thick steel bearing plates, with the slab bearing on neoprene pads atop the upper plate. Circular plates are used at the columns, and an 8-in. (20.32-cm) wide continuous strip is used at the abutments. Each column has one load cell, and each abutment has three placed at 3 ft (0.9 m) from both edges and at the center.

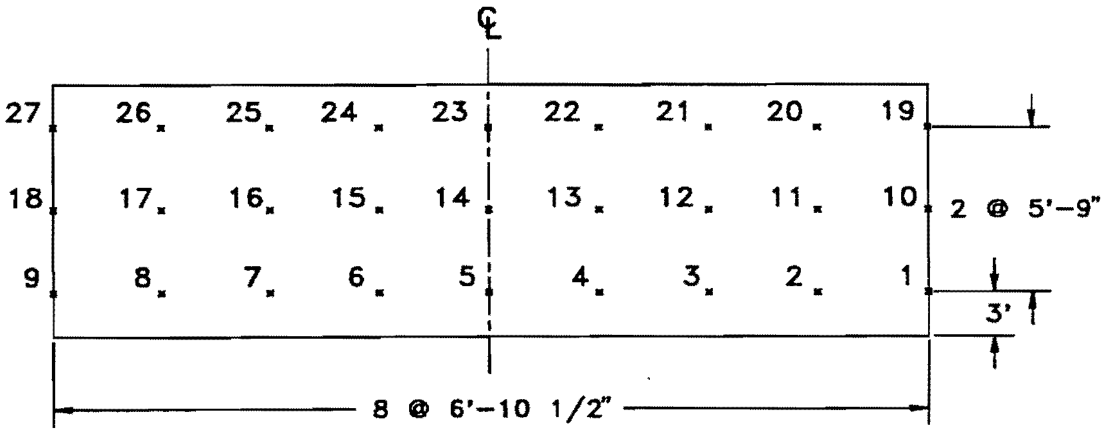

FIG. 8. Locations of Elevation Implants

3.1 Application of Strain Gages

Strain gages are mounted to the reinforcement prior to placing it in the form work using the following procedure:

1. Ridges on the deformed bar are ground off and the area is sanded smooth.
2. The bar is cleaned with a solvent and a neutralizer.
3. The gage is glued to the bar with a quick drying adhesive.
4. The gage is protected against moisture and damage with a layer each of Teflon, butyl rubber, neoprene rubber, foil, and nutrile rubber.

Stages of this procedure are shown in Fig. 9. Gages are only applied to one side of the rebar, neglecting any effects of bending. Tests conducted for a similar configuration (Scordelis, Bouwkamp, Wasti, and Anicic 1980) showed that loss of accuracy in a single gage, as opposed to double gage application is small. Each gage is equipped with an initial 3.3 ft (1.0 m) of lead wire, which eliminates soldering at the gage.

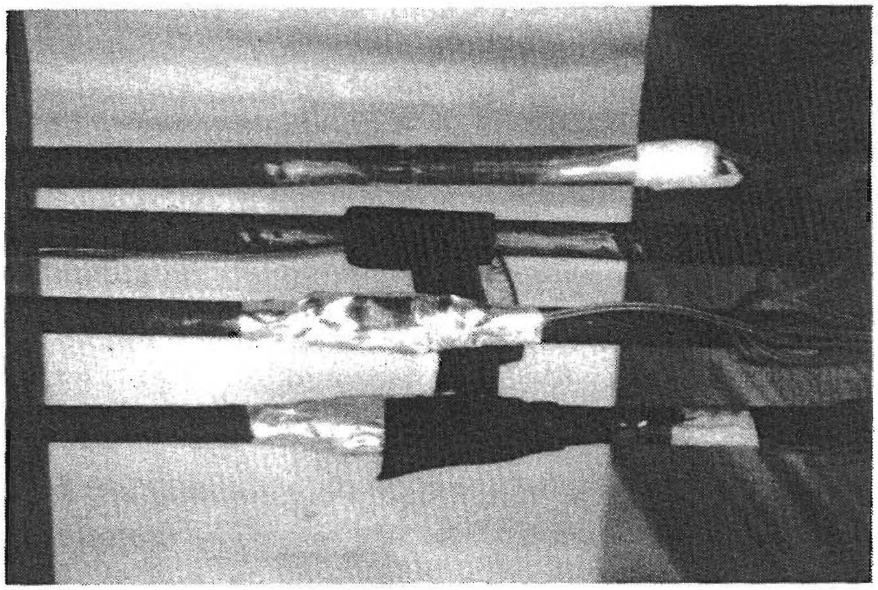

FIG. 9. Stages in Strain Gage Application

3.2 LVDT Calibration and Installation

A total of eighteen LVDTs are used to measure displacement. Seven of these transducers are manufactured by Scheavitz, and the other eleven by Trans-Tek. All LVDTs have a range of ±2 in. (5.1 cm). To calibrate the LVDTs, a scale with 1/60-in. (0.4-mm) increments is used to measure travel of the displacement plunger through full scale, corresponding voltage readings are taken, and a linear conversion factor is calculated.

LVDTs are placed under the slab at each location supported by individual timber or aluminum stands. Timber and aluminum is used to lower electrical interference. Each LVDT is calibrated while it is connected to its stand. LVDTs are placed under the slab after 100% of compensating dead load is in position.

3.3 Load Cell Calibration and Installation

A total of ten 50-kip (225-kN) load cells are used to measure reactions, all designed and constructed by A. L. Design, Inc. Calibration is achieved by loading with a 550-kip (2,475 kN) MTS testing machine recently calibrated by laboratory staff. Load and corresponding voltage are recorded and a linear conversion factor is calculated.

Load cells are placed in position between the bearing plates prior to completion of the deck form work. Load readings are then normalized to zero as an initial reading.

3.4 Collection Equipment and Software

Strain gage measurements are taken using a series of manual switch boxes, a Hewlett Packard digital voltmeter, and a micro-computer. The switch boxes are needed due to fact that the voltmeter can only read 30 channels of data at one time. The length of lead cable needed to connect the strain gages to the collection device necessitates use of a three wire shielded cable to reduce noise. Three sets of five lead cables are connected to the switch boxes which, in turn, are connected to the voltmeter. An IEEE-488 interface bus is installed in the micro-computer which allows communication with the voltmeter. A control program called Lotus Measure (Lotus 1986), that runs in conjunction with Lotus 123 (Lotus 1986), is used to control the voltmeter and collect data directly into a spreadsheet. A group of 6 switch boxes allows 30 gages to be read at each triggering of the voltmeter. The manual switches are then changed to allow the next round of 30 gages to be read.

3.5 Schedule of Measurement

In order to gain adequate data to verify the analytical tool, and to derive conclusions about the physical phenomena, data are collected as follows:

1. Strain measurements are taken daily during curing of the slab and begin immediately following construction. These measurements are used to study initial shrinkage of the structure. A 3-ft × 2-ft × 9-in. (0.91-m × 0.61-m × 22.9-cm) block of concrete, constructed at the same time as the slab itself, is monitored as a control specimen for shrinkage.
2. During transverse prestressing, strain measurements are taken after each pair of tendons is stressed. During longitudinal prestressing, strains are measured after extension of every eight tendons.
3. After completion of prestressing, as described later, displacement and strain are measured biweekly to study initial creep of the structure. The control specimen for shrinkage is also monitored in order to differentiate between strain due to creep and strain due to shrinkage. As changes in strain decrease, the frequency of measurements also decreases.
4. During design live loading, displacement and strain are measured at maximum load.

4. CONSTRUCTION OF MODEL

A combination of construction technologies is represented in the construction of Model 2. Substructure construction utilizes precasting techniques in that the structures are cast and then moved to their permanent locations on the laboratory floor. Also, any form work needed more than once is coated for ease of removal and used again. Cast-in-place techniques are used for slab construction. All fabrication of forms, placement of reinforcement, and pouring of concrete is undertaken by undergraduate and graduate students with the exception of concrete placement for the slab.

4.1 Calendar of Events

Significant events in the construction sequence along with their corresponding dates are

June 1, 1989:	Construction begins on model.
June 24:	First end abutment cast.
June 31:	Remove forms from abutment and move abutment into permanent location.
July 10:	Second abutment and columns cast.
July 20:	Remove forms from abutment and columns, and move abutment and columns into permanent locations.
July 25:	Work begins on shoring and form work for slab.
August 10:	Begin laying prestressing and reinforcing steel.
October 10:	Cast bridge slab.
October 30:	Remove sideforms and begin post-tensioning the transverse tendons, place elevation implants, take initial readings of elevations.
November 3:	Post-tension longitudinal tendons to 50% P_j.
November 17:	Drop shoring and form work; begin hanging dead load blocks.
December 18:	Post-tension longitudinal tendons to 100% P_j.
December 23:	Finish hanging dead load blocks.
December 28:	Take all initial readings for dead load testing.

4.2 Form Work

Abutment forms and column footing forms consist of 3/4-in. (1.9-cm) thick plywood with 2 × 4 ribbing spaced 2 ft (0.61 m) on center. Columns are formed using a 10-in. (25.4-cm) diameter Sonotube. Holes through the footings for bolts are formed by 2-in. (5.1-cm) diameter PVC pipe. Deck forms consist of 3/4-in. (19-mm) thick plywood supported by 8-in. (20.3-cm) deep, 18-ft (5.5-m) long aluminum joists, spaced 2 ft (0.61 m) on center, and supported by W6 × 12 I-beams at 7-ft (2.1-m) intervals to minimize deflections. This system, in turn, is supported by an adjustable height steel frame. Precise surveying is used to level the deck forms to within 0.005 ft (0.0015 m). Sideforms for the slab are provided by 2 × 10 boards planed to a 9 in. (22.9 cm) depth.

4.3 Casting of Substructure

The two abutments are cast one at a time, so that the same form work may be used for both of them. After placement of the reinforcing steel, the first abutment is cast using concrete provided by a local ready-mix supplier. Anchor bolts are placed in the face of the wall to provide pick-up points for moving the abutment to its final location. Steel bearing plates are also placed in the top surface. After 7 days the form work is stripped, and the abutment moved. The form work is then rebuilt, and the process repeated. The column footing is cast along with the second abutment. After casting the footing the Sonotubes are erected, and the columns poured. Pick-up points are provided for the columns by embedding rebar hooks in the top of the footing. After 7 days the form work is stripped, and the abutment along with the column bent are moved to their respective positions by an overhead crane.

4.4 Bridge Slab Construction

Upon final positioning of the abutments and columns, shoring and form work erection begin. After completion of the form work, the next step is to lay the bottom mat of passive reinforcement. Once this is completed the prestressing duct is placed on the steel. Since a flexible duct is used, the tendons must be inserted prior to casting so that the assembly is stiff enough to retain the desired profile during the concrete pour. After the tendons are inserted into their ducts, the top steel mat is positioned. Tendon ducts are tied vertically to the rebar and horizontally to the sideforms to achieve the desired profile. Care is taken to fasten the prestressing anchors at the proper inclination, 2.6° below horizontal, to prevent stress concentrations at the slab ends.

After all reinforcing is in place the slab is ready to be cast. Since casting of the slab is a relatively large undertaking, 28 cu yd (22.7 m^3) of concrete, and must commence smoothly for good quality in construction, a concrete construction crew is contracted for this phase of the project. They are in charge of the actual placement and finishing of the concrete. Project staff are responsible for slump testing, test cylinder construction, and crane operation for the drop bucket.

Six trucks of concrete delivered from a local ready-mix supplier are used to cast the slab. Concrete is placed starting at one end and commencing to the other. (Note that the technique of one continuous pour used to construct the laboratory structure differs from the multiple pours required to construct the prototype structure (Roschke, Pruski, and Sripadanna (1992)). As the concrete is delivered by the drop bucket, it is leveled and vibrated, with care taken to avoid strain gage locations. It is then screeded, jiggered, and floated to a tolerance of 1/8-in. (3.2-mm).

One problem in casting the slab arises from the fact that the flexible conduit used as prestressing duct is not watertight. Since bonded construction is used for the prestressing, it is necessary to keep cement paste from penetrating into the duct and causing blockage. Therefore, water content in the concrete is kept at a minimum, and a water reducing admixture is added to increase workability. As a further precaution, after casting is complete, pressurized air is forced through the ducts to clear them of any blockage. Slump of the concrete is shown in Table 2. As a result of the attempt to control blockage in the ducts, the concrete compressive strength is higher than the design value (Table 1).

Curing of the slab is accomplished by wetting the top of the slab and covering it with a sheet of polyethylene. This process is repeated daily during the curing period. After 7 days wetting is discontinued, and the sideforms are removed.

After 20 days sufficient strength is obtained to begin post-tensioning. This is a two phase operation, due to the additional dead load that must be applied for similitude. If 100% of the prestressing force is applied in one increment, the slab would crack as a result of the upward forces. Therefore, prestressing and dead load are applied in two increments — 50% at a time. After the first increment of prestressing, the shoring and bottom forms are removed. 50% of the dead load blocks are then suspended from loops of 3/8-in. (9.5-mm) cable embedded in the slab. Final prestressing and, subsequently, dead load is applied. Prestressing equipment consists of a mono-strand hydraulic jacking unit with a calibrated pressure gage designed and supplied by VSL, Inc. Details of prestressing procedures are discussed later.

Grouting of the tendon ducts completes the construction process. Grout consists of portland cement and water mixed with an expansion agent used to ensure bonding of the tendons. Grout expansion is limited to 4% of initial volume. Prior to prestressing, each tendon is pulled through its duct to further eliminate any blockage. Grout is then pumped into one end of the duct. The high point vent is left open until grout flows freely. It is then capped, and grout is pumped until it flows freely from the other end as per Post-Tensioning Institute recommendations (PTI Specification 1987). Figs. 10-15 show the sequence of slab construction.

TABLE 2. Slump of Concrete

Batch (1)	Slump[a] (in.) (2)
1	5.25
2	6.50
3	6.50
4	7.25
5	8.00
6	6.25

[a]Includes water reducing admixture

Note: 1 in. = 2.54 cm

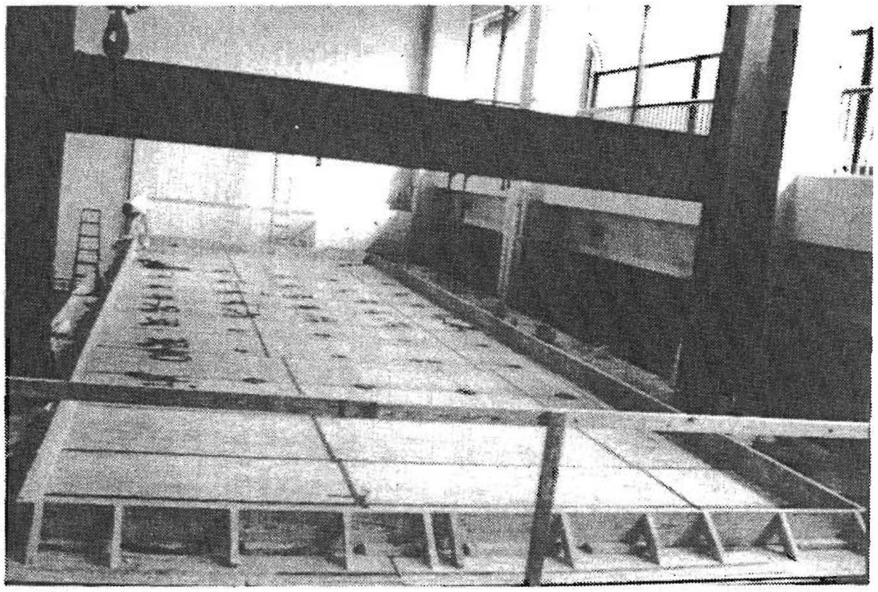

FIG. 10. Form Work for Slab in Place

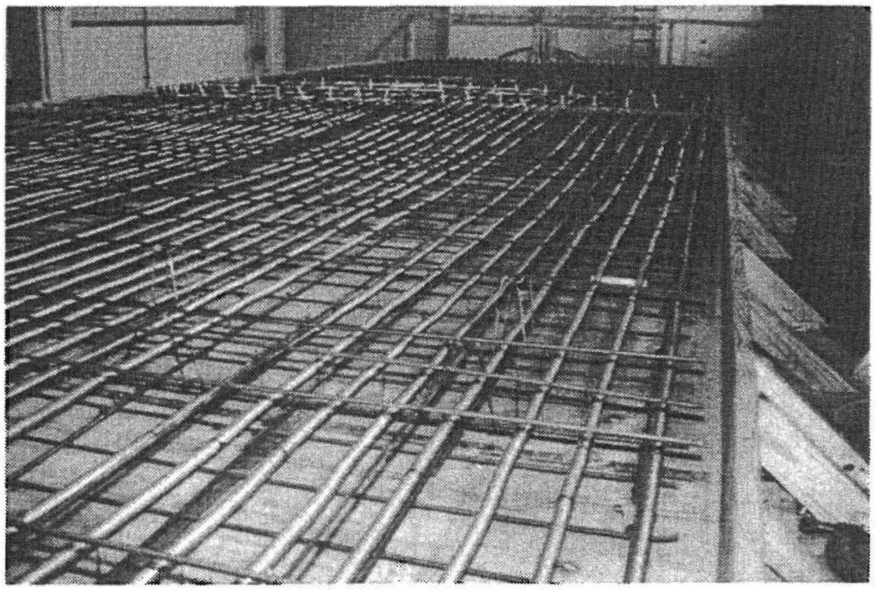

FIG 11. Prestressing and Reinforcing Steel Placed in Form

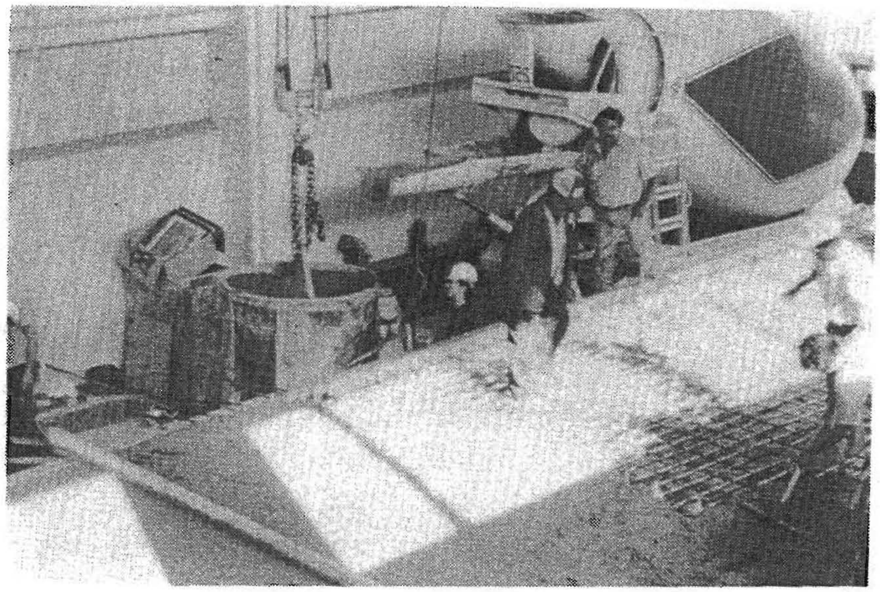

FIG. 12. Slab Being Poured

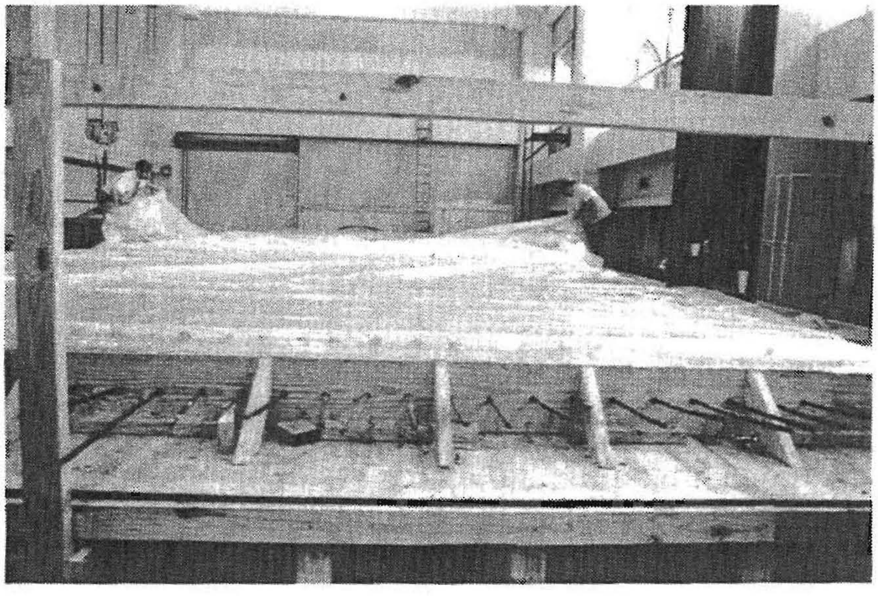

FIG. 13. Slab Covered for Curing

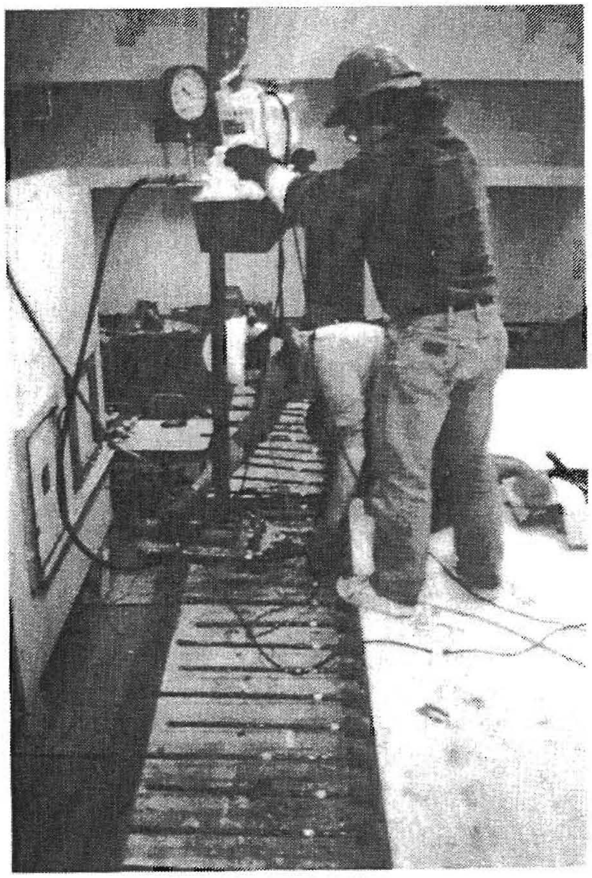

FIG. 14. Application of Prestressing Force

FIG. 15. Dead Weight Compensating Blocks are Suspended from Slab

5. MATERIALS

5.1 Concrete

Design compressive strength of concrete is 5,000 psi (34,500 kPa) with limestone coarse aggregate, maximum size of which is 3/4 in. (19.1 mm). The mix design is as shown in Table 3. A polymer-lignin-based water reducing admixture is added to increase workability. It has been shown (Brooks, Wainwright, and Neville 1981) that similar admixtures do not significantly affect shrinkage. These admixtures may, however, increase creep. Since creep is difficult to model in any case, this should not be a detrimental quality.

TABLE 3. Concrete Mix Specifications

Material (1)	Percent by Weight (2)
Cement	15.6 [a]
Aggregate	
Fine	31.9
Coarse	46.9
Water	6.2 [b]
Admixture	0.03

[a] 6.5 sack/cu yd
[b] 4.5 gal/sack
Note: Air content is 4%

Compression tests performed on cylinders at 7, 10, 14, 35, 64, and 170 days are used to determine the actual strength of concrete. The cylinders are 6 × 12 in. (15.2 × 30.5 cm); they are prepared and tested in accordance with ASTM standards C 192 and C 39 on a Soil Test compression testing machine. Results from these tests are summarized in Table 4, and shown graphically in Fig. 16. ACI Committee 209 (ACI 1971) recommends the following formula to evaluate strength of concrete versus age:

$$f_c(t) = \frac{t}{4 + 0.85t} f_c(28) \qquad (13)$$

where t = time in days after casting, and $f_c'(28)$ = 28-day uniaxial compressive strength in psi. A best curve fit of the measured values using this formula results in a 28-day compressive strength of 6,500 psi (44,850 kPa). Appendix III provides a detailed listing of the experimental results.

TABLE 4. Results of Concrete Strength Tests

Age (days) (1)	Average $f_c'(t)$ (psi) (2)	Average $f_t'(t)$ Experimental (psi) (3)	Average $f_t'(t)$ Calculated (psi) (4)
7	4,342	—	—
10	4,842	—	—
14	5,987	535	605
35	7,126	606	660
64	7,198	—	—
170	7,657	—	—

Note: 1 psi = 6.9 kPa

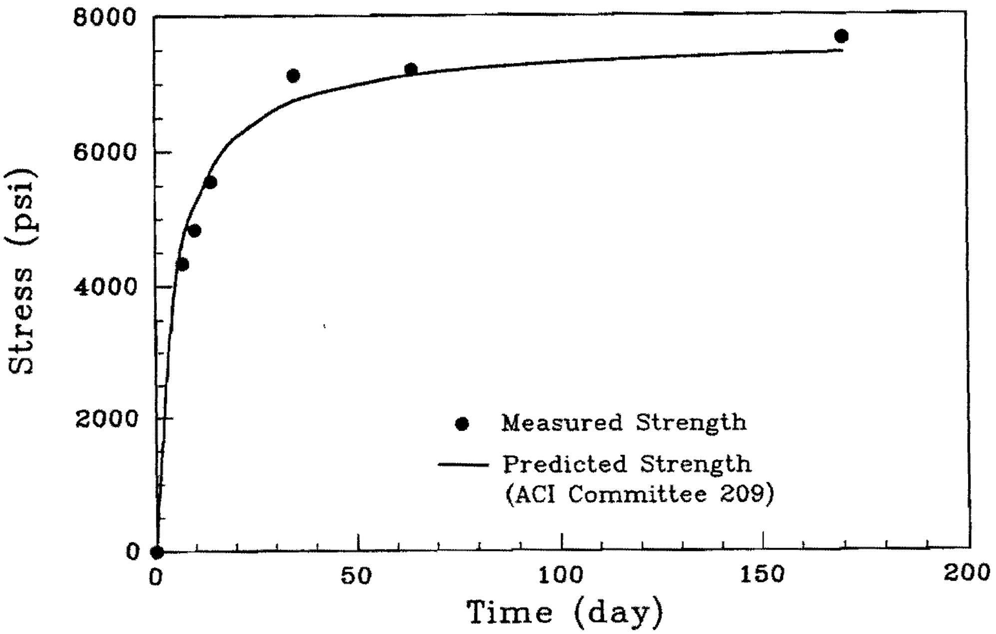

FIG. 16. Concrete Compressive Strength versus Age

Four-point bending tests are performed on 6 × 6 × 36-in. (15.24 × 16.24 × 91.44-cm) beams at 14 and 35 days to determine the modulus of rupture, f_t', for the concrete. Results of these tests are also shown in Table 4. Results compare adequately, within 10%, to values calculated using the following formula recommended by ACI Committee 209:

$$f_t'(t) = 0.65\left[w f_c'(t)\right]^{0.5} \quad (14)$$

where w = unit weight of concrete, and t = time in days after casting

An accurate measure of elastic modulus E_c is important for use in the analysis program, as discussed in chapter 6. E_c is determined from tests at 14, 35, and 170 days. Test results are tabulated in Appendix III, and summarized in Table 5 along with calculated values from the equation used by ACI committee 209

$$E_c(t) = 33.0\, w^{1.5} (f_c'(t))^{0.5} \quad (15)$$

where $E_c(t)$ = initial uniaxial tangent modulus in psi, and t = time in days after casting. Results at 14 and 35 days are imprecise due to errors in testing procedures and are not used in the analysis. After refinement of experimental procedures confidence in the value of E_c at 170 days is high. This is important because live load tests begin at this time. To determine E_c at 170 days, three cylinders are loaded to 50% of ultimate strength on a 550-kip (2,475-kN) MTS testing machine. Load is recorded by the machine's load cell readings. Four gage readings from a compressometer are averaged to give corresponding deflection measurements. The average modulus of the three cylinders is then taken as E_c. Results of this test are shown graphically in Fig. 17.

TABLE 5. Elastic Modulus of Concrete

	Average E_c	
Age (day) (1)	Experimental (ksi) (2)	Calculated (ksi) (3)
14	4,987	4,458
35	3,826	4,864
170	5,966	5,042

Note: 1 ksi = 6.9 MPa

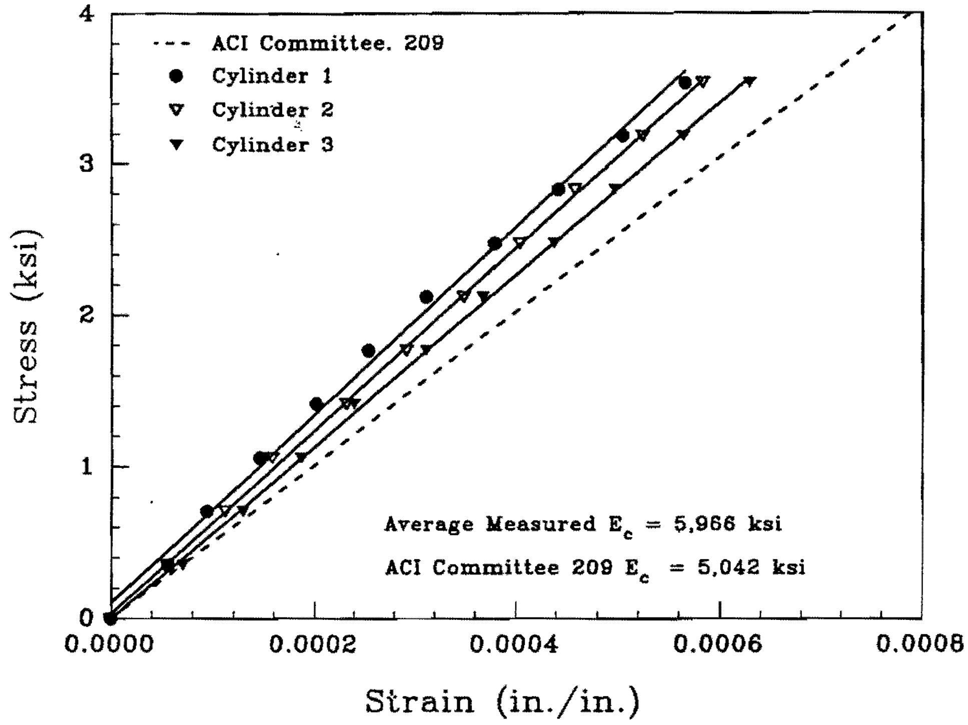

FIG. 17. Elastic Modulus of Concrete: 170 Days

5.2 Prestressing Steel

Prestressing is provided by single 0.6-in. (1.52-cm) diameter, stress-relieved, 7-wire strands. Ultimate stress is rated at 270 ksi (1,863 MPa). Nominal area of the strand, A_{ps}, is 0.217 in.^{2} (1.40 cm^2). Properties of the strand important for this study are the initial elastic modulus, E_{ps}; the 0.1% offset yield stress, f_{yps}; and stress-strain relations from zero to ultimate load. The first is needed to calculate required elongation to achieve seated prestressing force. The latter properties are needed as input for the analysis program.

Tensile tests are performed on a section of strand to determine these properties. The apparatus for testing consists of a MTS 550-kip (2,475-kN) testing machine, and end connections that use the anchor head to grip the tendon. Strain data are measured using an electronic clip gage with a 1-in. (2.54-cm) gage length and an accuracy of 0.00001 in. (0.000254 mm). In order to increase the gage length and reduce local elongation effects, an adapter is fabricated and affixed to the tendon. The clip gage is then fastened to the adapter (see Fig. 18). Load is measured through the testing machine's load cell. Results of the tests are shown in Fig. 19. Initial elastic modulus is 28,500 ksi (196.5 GPa), and 0.1% offset yield stress is 240 ksi (1,656 MPa). Input values for the analysis program refer stress-strain data that are needed; they are discussed later in the text.

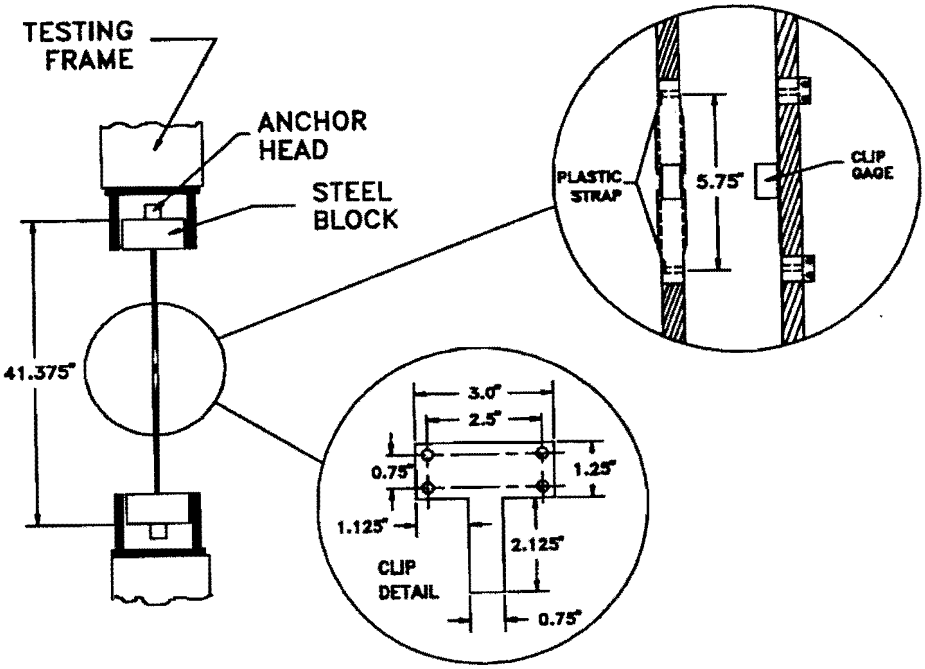

FIG. 18. Test Setup for Prestressing Tendons

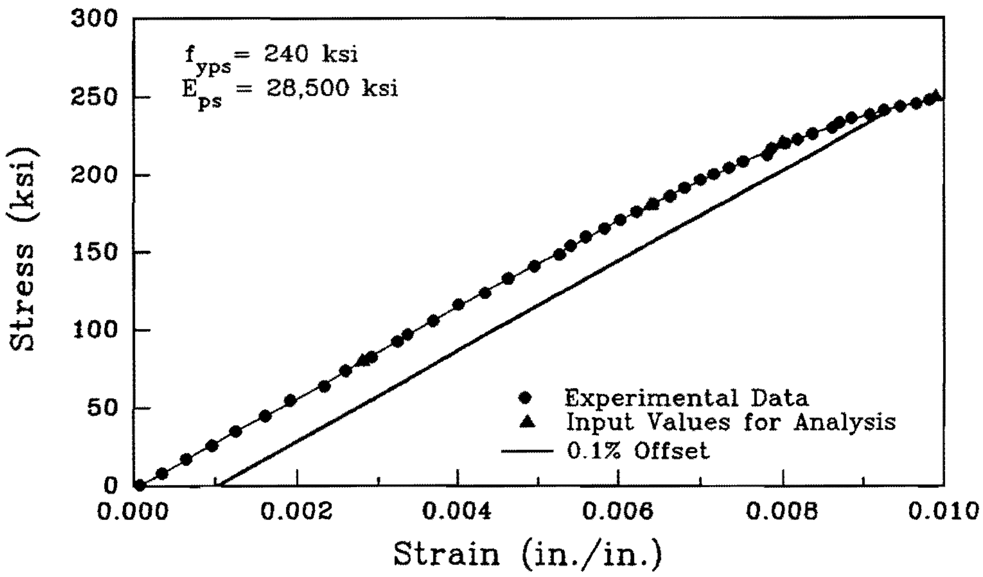

FIG. 19. Material Properties of Prestressing Steel

5.3 Reinforcing Steel

As discussed previously reinforcing steel is not of major structural importance. Common #3 deformed reinforcement bar is used, and material properties of this type of reinforcement are well known. Therefore, testing of the steel is not undertaken. The following values are used when analyzing the structure. Minimum yield stress is 60 ksi (414 MPa), and minimum tensile strength is 90 ksi (621 MPa) (ASTM specifications). Initial elastic modulus is 29,000 ksi (200.1 GPa) (ACI 318-83).

In the analysis program a simple bilinear constitutive model is used; the steel is assigned a reduced elastic modulus after yield. This is referred to as a strain hardening modulus. Dividing the minimum yield stress by the initial elastic modulus gives a strain at yielding of 0.0021 in./in. ASTM specifications report a minimum percentage of elongation at tensile strength of about 9% for #3 bars. Solving a linear relation between these two stress-strain equations gives a value of 340 ksi (2,346 MPa) for the strain hardening modulus. Nominal area of the bar is 0.11 in.^{2} (0.71 cm^2). Epoxy-coated rebar is used in the top layer of the prototype reinforcement but not in the model.

5.4. Elastomeric Pads

Testing is done to determine the load-deflection curves of the elastomeric pads, in order that these values may be used to calculate slab deflection due to the elastic support provided by the pads. Two column pads are placed, separately, between two square steel plates and compressed in the 550-kip (2,475-kN) MTS testing machine. Load is measured through the machine's load cell. Two dial gages are placed on opposite edges of the steel plates and their average is taken as the corresponding deflection of the pad. Fig. 20 shows the nonlinearity of these curves. As an approximation of this response a linear regression is performed to determine the average stiffness of the pads. The same test is repeated for a 12-in. (30.48-cm) long strip of the abutment pad, and stiffness is reported per inch (2.54 cm) of bearing length. Results for this unreinforced material are shown in Fig. 21.

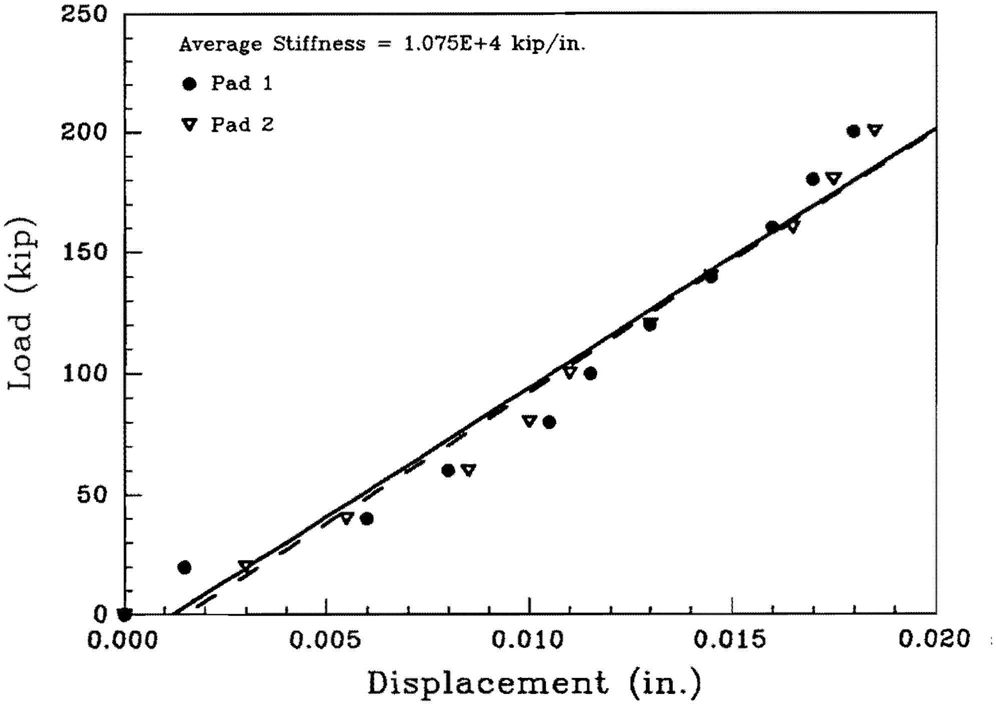

FIG. 20. Stiffness of Column Bearing Pad

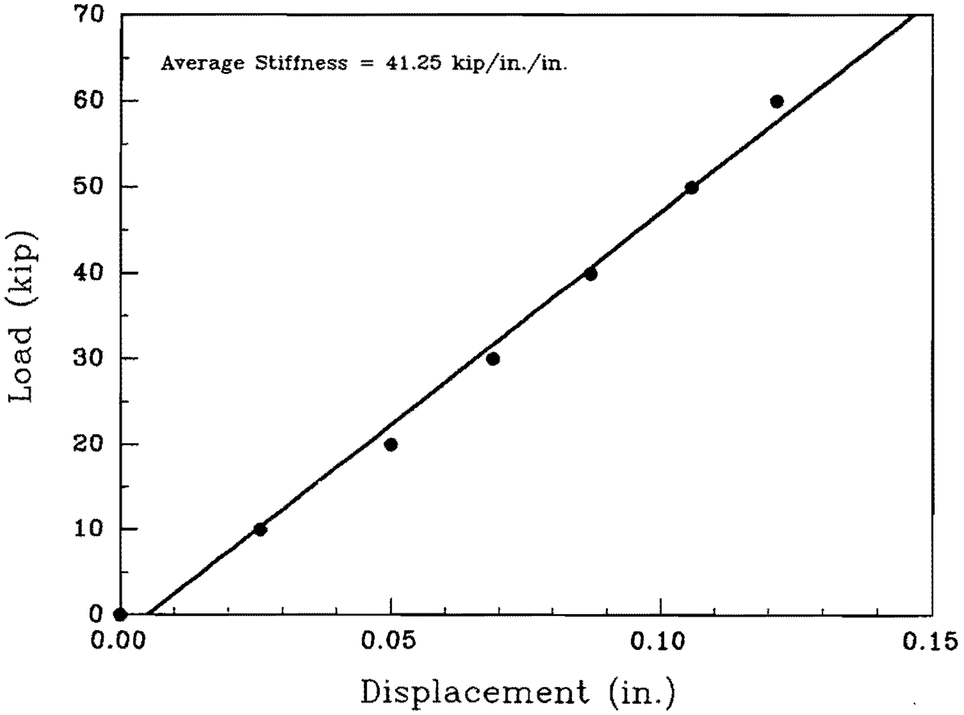

FIG. 21. Stiffness of Abutment Bearing Pad

6. ANALYSIS METHOD

6.1 Finite Element Method

Finite element analysis (FEA) is a well-known and accepted method of determining structural response. Numerous books (Zienkiewicz 1977) have been written detailing its formulation and use. Therefore, only a brief description is given herein.

The analysis is performed by dividing the structure into discrete sections or elements, thus reducing an infinite number of degrees of freedom to a manageable number at the boundary points or nodes of these elements. It is assumed that individual behavior of the elements can be modeled using an interpolation or shape function. Elements are then coupled by continuity constraints that lead to the following well-known formulation:

$$[K]\{u\} = \{P\} \quad \text{.......} \quad (16)$$

where [K] is the coupled stiffness matrix of the elements, {u} is the displacement vector of the nodes, and {P} is the applied load vector. This equation is then solved for displacements, and the strains are solved for using strain-displacement relationships. Stress can then be determined using material constitutive relations.

Two types of problems may be analyzed using FEA. One is a linear formulation in which the material is linear elastic and displacements are small. The other is a nonlinear formulation where either the material is nonlinear, the displacements are large, or any combination of the two. Analysis of reinforced and prestressed concrete for ultimate strength or time-dependent effects involve the latter formulation.

6.2 Analysis Program

For this study it is desired to verify a program that accurately predicts nonlinear behavior of prestressed concrete slabs up to and through the ultimate load. NOPARC (**NO**nlinear Analysis of **P**restressed **A**nd **R**einforced **C**oncrete Slabs and Panels) is a finite element program developed at the University of California, Berkeley, to:

> ...trace the quasi-static response of reinforced and prestressed concrete slabs and panels under short time and sustained load

> conditions. Time-dependent effects due to load history, temperature, creep, shrinkage and aging of concrete and stress relaxation in prestressing steel are incorporated. The load-deflection history of such structures through the elastic, inelastic and ultimate ranges is calculated. The ultimate failure of these structures due to in-plane membrane plus bending effects is then predicted considering local failures in steel and concrete along with the deterioration of the structural stiffness due to progressive cracking (van Greunen 1979).

Details of the operation of NOPARC are given by van Greunen (1979) and Roschke and Pruski (1992). However, considerations that apply to the successful use of this program as an analysis tool for Model 2 are discussed in what follows.

Precise material properties are needed to perform an accurate analysis. NOPARC allows for direct input of these properties for all materials. Properties that apply to concrete are compressive strength, tensile strength, initial elastic modulus, and strain at compressive strength. NOPARC also has a provision to generate the values for concrete as recommended by ACI Committee 209 (ACI 1971). Eqs. 13 through 15, along with the following equation suggested by Hognastad (1951), are used in NOPARC to compute concrete properties

$$\varepsilon_c(t) = \frac{f_c'(t)}{E_c(t)} \quad \text{......} \quad (17)$$

where $\varepsilon_c(t)$ = strain corresponding to peak stress $f_c'(t)$ at t days after casting. Shrinkage and creep parameters may be input, if available, or the following ACI formulas (ACI 1971) may be used:

(a) shrinkage

$$\varepsilon_{sh}(t) = K_s K_h K_H \frac{(t-7)}{35+(t-7)} \varepsilon_{shu} \quad \text{......} \quad (18)$$

where $\varepsilon_{sh}(t)$ = shrinkage at time t for concrete moist cured for 7 days; ε_{shu} = strain at ultimate shrinkage; K_s = correction factor for slump = 0.89 + 0.041 s; s = slump in inches; K_h = correction factor for the size of the concrete member determined from experimental curves; K_H = correction factor for relative humidity = 1.4 - 0.01

H (for $40 \leq H \leq 80$) and $= 3.0 - 0.03\ H$ (for $80 \leq H \leq 100$); H = percent relative ambient humidity; and

(b) creep

$$C_t = K_s K_H K_h K_\tau \frac{(t-\tau)^{0.60}}{10+(t-\tau)^{0.60}} C_u \quad \text{.......(19)}$$

where

$$C_t = \text{creep coefficient} = \frac{\text{creep strain at time t}}{\text{initial instantaneous strain}}$$

C_u = ultimate creep coefficient to be determined from experimental data

$$= \frac{\text{creep strain at infinite time after loading}}{\text{initial strain at time of loading}}$$

= 2.35 for standard conditions

K_s = slump correction factor

= $0.81 + 0.07\ s$

K_H = humidity correction factor

= $1.27 - 0.0067\ H$ (for $H \geq 40$)

K_h = size correction factor

= $1.0 - 0.0167(sz - 6.0)$ (for $sz > 6.0$)

= 1.0 (for $sz \leq 6.0$)

K_τ = age at loading correction factor

= $1.25\ \tau^{-0.118}$ for moist cured concrete for 7 days

sz = minimum dimension of member in inches

τ = age at loading in days

Other input parameters for concrete include ultimate shrinkage strain, slump, minimum size of member, relative humidity, and coefficient of thermal expansion. The first four parameters relate to shrinkage strain and the last, of course, to temperature-induced strain.

Properties needed for reinforcing steel include modulus of elasticity, yield stress modulus for strain hardening, and ultimate strain. These quantities are all determined from experimental data.

Properties needed for prestressing steel are the 0.1% offset yield stress, a relaxation coefficient, and five points on a stress-strain curve. These properties are also determined from experimental data. The relaxation coefficient is used in the following equation:

$$\frac{f_s}{f_{si}} = 1.0 - \frac{\log t}{c}\left[\frac{f_{si}}{f_{yps}} - 0.55\right] \quad \text{.......... (20)}$$

for $\frac{f_{si}}{f_{yps}} > 0.55$, where f_s = steel stress at time t; f_{si} = initial steel stress; f_{yps} = 0.1% offset yield stress; c = relaxation coefficient (10.0 for prestressing steel); t = time in hours after stressing of the steel.

Other information needed for prestressing pertains to the type of construction employed. This includes specifying whether the tendons are post-tensioned unbonded, post-tensioned bonded, or pretensioned. Also, frictional coefficients of the duct are required for wobble and curvature. The frictional coefficients are used to determine force at any point using the following equation (Lin and Burns 1981):

$$P(x) = P_o\, e^{-(\mu q + Kx)} \quad \text{.......... (21)}$$

where P_o = force in tendon at x = 0; P(x) = force in tendon at x; μ = coefficient of curvature friction; q = angle change in tendon over distance x; K = coefficient of wobble friction; and x = distance from jacking end.

An innovative approach to applying prestressing force is used by NOPARC. Most analyses of prestressed structures calculate equivalent loads for the prestressing forces and then input these values as a uniform load. NOPARC uses a method where the tendon profile is input along with a prestressing force, and the equivalent loads are then calculated within the program. This method allows for recalculation of the prestressing load vector as changes in geometry are determined.

Boundary conditions must be modeled adequately for an accurate analysis. NOPARC has provisions for solid and elastic supports, along with specified displacements for the supports. Details of how boundary conditions and material parameters effect the analysis are discussed with the results of this study.

7. DESCRIPTION OF TESTS

7.1 Prestressing and Dead Load

Of primary interest in this study are the stress distribution due to the transverse prestressing and the time dependent effects due to this distribution. Therefore, an important part of the testing program is the application of prestressing force and the compensating dead load.

When concrete compressive strength reaches 0.80 $f_c'(28)$ or greater, post-tensioning is applied, beginning with the transverse direction in the sequence shown in Fig. 22. Strain data is taken after the first tendon is stressed to determine the initial strain distribution due to transverse prestressing. Subsequently, data is taken after each pair of tendons is stressed.

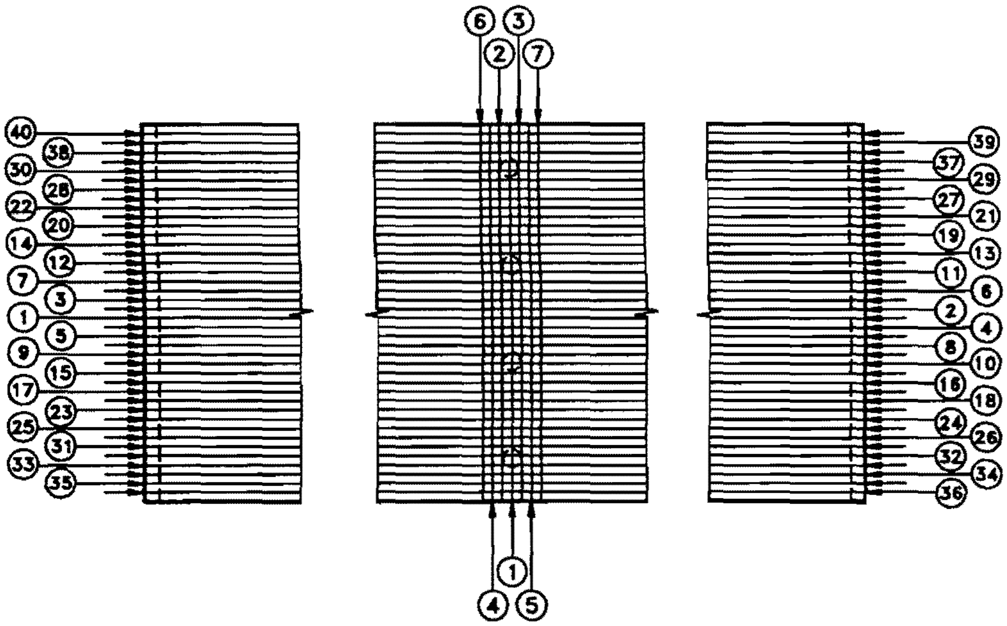

FIG. 22. Tendon Jacking Sequence

Elongation of each tendon is measured during the jacking operation to determine initial prestressing force. Required elongation for the transverse tendons is calculated using the following equations (Lin and Burns 1981):

$$\delta L = \frac{F_2 L}{E_{ps} A_{ps}} \; \frac{e^{\mu\alpha + KL} - 1}{\mu\alpha + KL} \quad \text{.........} \quad (22)$$

with

$$F_2 = F_1 e^{-(\mu\alpha + KL)} \qquad (23)$$

where A_{ps} = nominal area of tendon; E_{ps} = initial elastic modulus; F_1 = force at jacking end; F_2 = force at dead end; K = wobble coefficient; L = length of tendon; α = accumulated change in angle over the length of the tendon; μ = curvature coefficient.

Frictional coefficients, μ and K, are unknown prior to prestressing and must be assumed in order to calculate a target elongation. From AASHTO section 9.16.1 (*Standard* 1989): K/in. = 0.000125 (K/m = 0.0049) and μ = 0.25. Since the tendon profiles have small angle changes and the tendon lengths are short, small deviations from the assumed values should not cause significant errors in elongation determination. After more accurate values of the frictional coefficients are established from data collected during the post-tensioning procedure, prestressing force can be adjusted accordingly. For the transverse direction F_1 = 38.0 kip (262 MPa), α = 0.0, and L = 210 in. (5.33 m). Therefore,

$$F_2 = 38.0\, e^{-[(0.000125)(210)]} = 37.0 \text{ kip } (255 \text{ MPa})$$

and

$$\delta L = \frac{37.0(210)}{29{,}000(0.217)} \quad \frac{e^{[(0.000125)(210)]} - 1}{(0.000125)(210)} = 1.25 \text{ in. } (3.18 \text{ cm})$$

One important loss of prestressing force is anchor seating. The usual method used to overcome this loss is to overstress the tendon before releasing the force. However, in this case since the tendon length is relatively short, the amount of overstress required exceeds the stress in the tendon recommended by AASHTO or ACI. Also, seating distance of the tendons and wedges (see Fig. 5) may vary from one anchor to the next. Therefore, in order to achieve a uniform prestressing force in the transverse direction it is decided to shim between the anchor head and anchor plate to offset any loss, rather than overstressing. Thus, a nearly exact elongation can be achieved for each tendon in the laboratory model. No shimming operation is performed on tendons in the prototype structure.

Elastic shortening is ignored in the transverse direction because there are few tendons, and they are stressed from opposite ends. Therefore, effects of shortening of the concrete are minimal.

Stressing procedure for each transverse tendon is as follows:

1. Stress tendon to 20% of required initial force according to the calibrated pressure gage provided with the jacking equipment. Measure distance from the anchor head to a datum that is marked on the strand.
2. Stress tendon to 100% of required initial force according to gage pressure. Measure distance from anchor head to datum. Compare the difference of this measure and that for 20% of the final force to 80% of the elongation calculated using Eq. 22. Increase or decrease pressure as required to achieve the correct elongation measurement.
3. Release tendon back to 20% of the required initial force and measure distance to datum. The difference between this measure and that for 100% of the force is the anchor seat distance.
4. Shim the anchor head out to the anchor seat distance.

As described previously, prestressing of the longitudinal tendons is achieved in two stages. For the intermediate stage the initial force required is approximately 50% of the final design force. Steps 1 to 3 above are used for this process. However, in step 2 pressure is not adjusted to correct elongation because this stress is released for the final prestressing operation. Strain data is collected after stressing every eight tendons to determine the change in strain distribution in the region of the transverse tendons. Normally, in a tendon of significant length similar to that used in the prototype, the dead end is also stressed to eliminate loss of force due to friction. However, at this intermediate stage, loss of force is small and, thus, dead end stressing is impractical.

After this stressing, 50% of the compensating dead load is suspended from the slab. Strain and displacement data are then taken in order to record a strain history for the slab.

Final longitudinal prestressing is more complicated than for the transverse tendons. In the latter case anchor set is eliminated and, therefore, elongation of the tendon and prestressing force are influenced only by the force of friction acting against the jacking force. In the longitudinal direction anchor set is not eliminated and, thus, the force of friction also acts in the opposite direction against the decrease in force due to the shortening of the tendon. Since the frictional force acts in both directions, the elongation of the tendon can no longer be solved using Eqs. 22 and 23, which are derived with friction force in one direction.

A piecewise approximation of tendon elongation is accomplished using Eq. 21 to determine the stress in the tendon as a result of friction loss, and the "area lost" method (Naaman 1982) to determine the tendon stress reduction due to anchor set loss. The general idea behind the "area lost" method is as follows:

> ...the total area between the stress diagrams in the steel just before and after anchorage set is equal to $E_{ps}d$ (Naaman 1982).

Using this approximation, equations may be written to describe the stress distribution in the tendon due to anchor set. The derivation of these equations may be simplified further if it is assumed that the stress diagram for a tendon is approximately linear and, therefore, equations of area for simple geometric figures may be used.

Incorporating friction and anchor set loss equations into spreadsheet form results in a stress profile shown in Table 6. Total elongation after anchor set for the 41.0-kip design prestressing force is 4.6 in. (11.7 cm). Fig. 23 shows the calculated profile of the tendon stress after release. The overstress necessary to achieve 4.6 in. (11.7 cm) of elongation corresponds to a force of 49.9 kips (224.6 kN). Final prestressing force is applied by releasing the intermediate stress, applying 49.9 kips to the tendon and then resetting the wedge. Elongation and strain data are recorded as for the intermediate load step. The required pressure reading is also noted. For this final stage of prestressing the dead end of the tendon is stressed to eliminate loss of force due to friction. Using the recorded pressure readings for the jacking end force, and assuming a linear approximation of force vs. pressure required, pressure for the design force is calculated. This approximation is valid because only a small amount of additional force is required. The dead end anchor is then shimmed to retain the desired force. After the final stressing, the remaining dead load is suspended. Strain and displacement data are then recorded to continue recording the stress history.

Prestressing force and dead load are applied to the structure for the duration of the test. Effects of these loads, including structural support, creep, biaxial stress, and shear lag, are to be examined.

TABLE 6. Load and Elongation Calculations for Longitudinal Tendons

Distance from Jacking End, x (in.) (1)	P(x) (kip) (2)	Stress(x) (ksi) (3)	Average Stress in Section (ksi) (4)	δL (in.) (5)
0.00	40.23	185.4		
			186.41	0.1918
29.33	40.67	187.4		
			188.06	0.1232
48.00	40.95	188.7		
			189.71	0.1952
77.33	41.39	190.7		
			191.36	0.1254
96.00	41.66	192.0		
			193.01	0.1986
125.33	42.10	194.0		
			194.67	0.1275
144.00	42.38	195.3		
			196.32	0.2020
173.33	42.82	197.3		
			197.97	0.1297
192.00	43.10	198.6		
			199.62	0.2054
221.33	43.54	200.6		
			201.27	0.1319
240.00	43.82	201.9		
			202.74	0.1707
264.00	44.17	203.6		
			204.39	0.1721
288.00	44.53	205.2		
			206.45	0.1376
307.00	45.07	207.7		
			207.64	0.0364
312.00	45.05	207.6		
			205.78	0.1733
336.00	44.26	203.9		
			202.15	0.1702
360.00	43.48	200.3		
			199.03	0.1676
384.00	42.91	197.7		
			196.98	0.1659
408.00	42.58	196.2		
			195.51	0.1646
432.00	42.27	194.7		
			193.88	0.1995
461.33	41.88	192.9		
			192.43	0.1261
480.00	41.64	191.8		
			190.99	0.1966
509.33	41.25	190.1		
			189.56	0.1242
528.00	41.01	189.0		
			188.14	0.1936
557.33	40.64	187.2		
			186.73	0.1223
576.00	40.40	186.1		
			185.34	0.1907
605.33	40.03	184.4		
			183.95	0.1205
624.00	39.80	183.4		
			182.57	0.1879
653.33	39.44	181.7		
			181.20	0.1187
672.00	39.21	180.6		
				Total = 4.6

Note: 1 in. = 2.54 cm; 1 kip = 4.5 kN; 1 ksi = 6.9 MPa

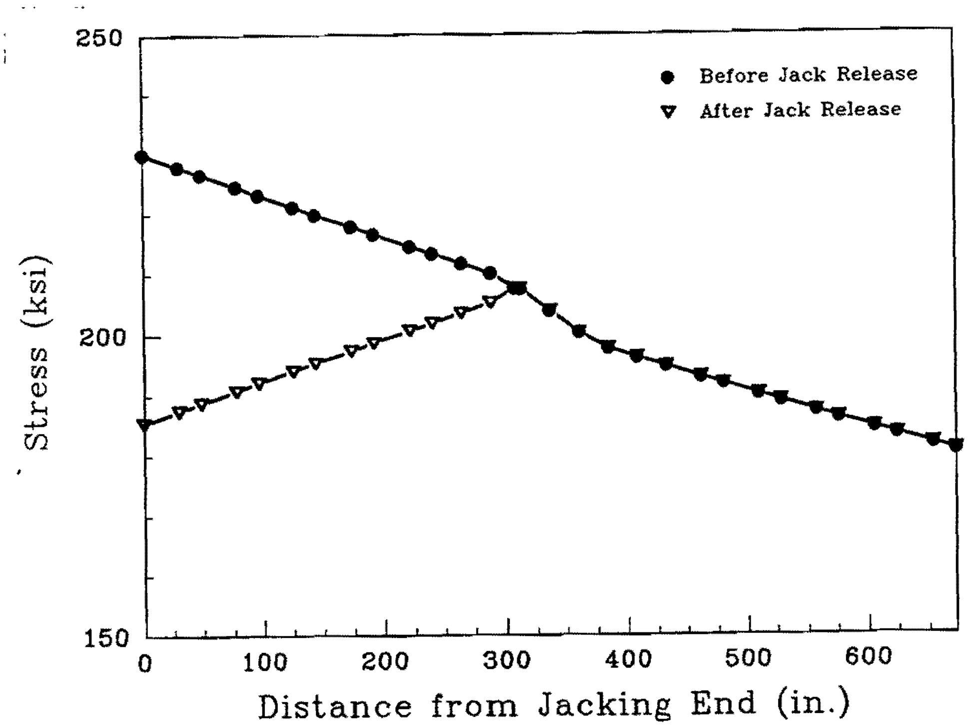

FIG. 23. Calculated Tendon Stress Profile

7.2 AASHTO Design Loads

In design of concrete bridge decks and from the perspective of corrosion due to deicing salts (Poston et al. 1987), it is desirable not to have any tension in the top surface of the slab. Therefore, it is important to accurately predict response of the structure to both dead and live loads. For long spans it is unlikely that live load will control, but as the span becomes shorter and dead load becomes less prominent, design live load may well control. It may also be desirable in future designs to reduce the slab depth from that used in the prototype for this study in order to economize. This reduction may also magnify effects of live load.

To measure the response of the model to live load, and to verify FEM's predictions of this response, a scaled AASHTO HS20-44 lane load (*Standard* 1989) is applied. The prototype loading consists of a uniform load of 64 psf (3,072 Pa) distributed over a 10 ft (3.05 m) wide lane, and a concentrated load of 18,000 lb (81 kN) in each span. According to the rules of similitude, this corresponds to 64 psf (3,072 Pa) distributed over a 3 ft (0.9 m) wide lane and a concentrated load of 1,620 lb (7.29 kN) per lane in each span. Two lanes of uniform load consisting of blocks of concrete capable of being moved from one location to another are used to supply this loading. Concentrated loads are applied in each span by hydraulic actuators attached to an overhead frame (Fig. 24). Different combinations of loads are applied to determine if predicted strains and displacements agree satisfactorily with measured strains and displacements.

7.3 Serviceability and Fatigue Considerations

An important consideration in the design of structures subjected to repeated loading is fatigue strength. During its lifetime a bridge, such as Taft Street overpass, can be expected to undergo 500,000 to 1 million significant stress cycles due to HS20-44 or heavier loads. If the stress range experienced is of considerable magnitude severe distress could occur.

It is generally accepted that the fatigue strength of concrete over a life of 10 million cycles (tension, compression, or flexure) is approximately 55% of its original static strength (ACI 1974). A linear decrease in strength with respect to number of cycles has been assumed in the past. However, Su and Hsu (1988) found that much of the decrease in strength occurs in the first 100,000 cycles. Over a 10-year period, this corresponds to about 30 stress cycles per day. Fatigue strength at 100,000 cycles of an HS20-44 truck is estimated as 67% of static strength.

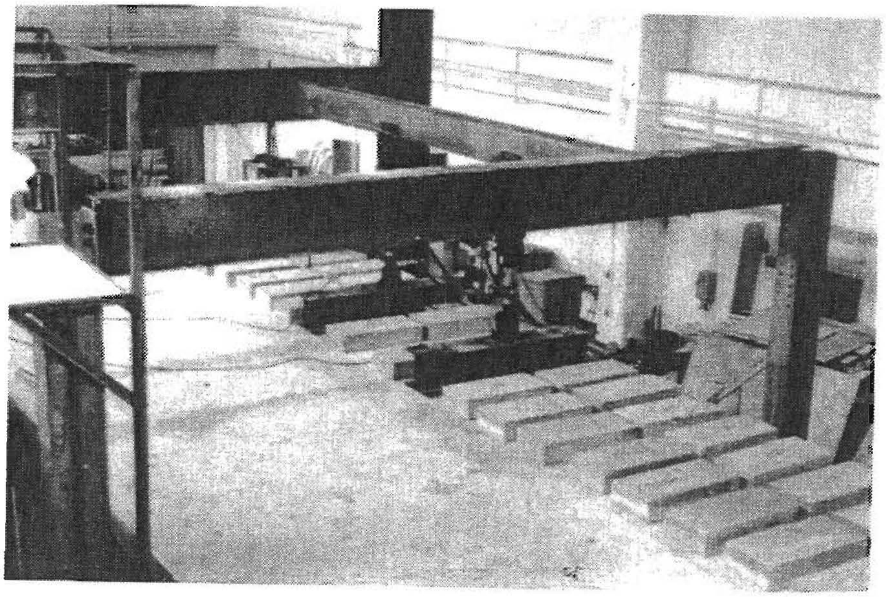

FIG. 24. Hydraulic Actuators and Overhead Frame

One characteristic of fatigue failure of concrete is increased micro-cracking, which can lead to a reduction of strength. This condition can also effect additional corrosion in a reinforced concrete member and thereby cause further damage. It is also known that the range of cyclical stress has a major influence on fatigue strength (ACI 1974). For instance, if the minimum stress applied is 0 psi, then the fatigue strength of concrete is 55% of static strength at 10 million cycles. This reduction in strength holds true for tension, compression, or flexure. As the minimum stress increases, the maximum stress that can be endured for this number of cycles also increases. However, the incremental increase in maximum stress is less than the incremental increase in minimum stress. That is, the two extreme levels of stress form an envelope. As the minimum stress level increases, the stress range that the concrete can undergo decreases.

In general, service load compressive stresses in the concrete are low. Therefore, fatigue failures usually occur when reinforcing or prestressing steel undergo maximum tensile stresses that are above their fatigue strength. This means that the fatigue strength of the concrete is not usually of major importance when predicting fatigue failure. However, it is possible that as the strength of the concrete is reduced during repeated loading, cracking of the concrete may occur. It is recommended by ACI Committee 215 (1974) that a limit of 20 ksi (138 MPa) and 0.1 f_{pu} be placed on the tensile stress range for reinforcing steel, and prestressing steel, respectively, to avoid failure.

In this study a fatigue failure is not expected. However, due to the complex stress distribution caused by the banding of transverse prestressing, as shown in Fig. 25, the high stress gradient in the region of transition from compression to tension may experience a significant amount of microcracking when repeated loads are applied. In corrosive environments or when deicing salts are used, cracking leads to corrosion of the reinforcing steel which could eventually lead to deterioration of the concrete surface. Poston et al. (1987) found that although application of prestressing may close cracks after live loading is released, chloride concentrations nevertheless rise above levels that cause corrosion. It is suggested that, when practical, cracking should be prevented.

A preliminary FEA is used to study the effect of a scaled AASHTO HS20-44 truck load which has been multiplied by specified impact and overload factors of 1.30 and 1.67, respectively. Fig. 26 shows the location of the loads and the area of the slab represented in the stress plots that follow. The contour plot of Fig. 27 shows the transverse stress in the bottom fiber of Model 2 due to prestressing and dead load. Fig. 28 shows total transverse stresses in the same bottom layer caused by the additional HS20-44 live load. Subtracting stresses due to dead and prestressing loads (Fig. 27) from the total stress in Fig. 28, leads to the change in stress due to live load (Fig. 29). From Figs. 25 and 29 it can be seen that application of live load causes regions of the slab in compression to become regions in tension. Although stress ranges due to live load are small, i.e. approximately 50 psi (345 kPa), it is still uncertain what damage may occur, due to the complex nature of stress in this region.

In most fatigue studies, cyclical concentrated loads are applied at a fixed location. Using a moving wheel load, Perdikaris, Beim, and Bousias (1989) found that the fixed location method results in higher fatigue strengths at a higher number of stress cycles for concrete bridge decks. A variation on the fixed location method utilizes a step-wise moving concentrated load. In this case failure strength is also lower and occurs at fewer cycles (Okada, Okamura, and Sonoda 1978).

This study uses four load locations to represent passage along the slab of wheel loads from a truck (see Fig. 30). Two loads, one for each wheel, are applied at each of the four locations. The number of locations is limited only by the number of available actuators in the laboratory. Ideally, an infinite number of actuators would be used to simulate continuous passage of the vehicle. A varying load in a given time interval is applied at each location. By correct sequencing of loads at the four locations, dynamic effects due to high speed passage of a truck are more closely approximated. Also, front and rear wheel interaction is included in the stress wave patterns. Traffic is assumed to flow from right to left in Fig. 30.

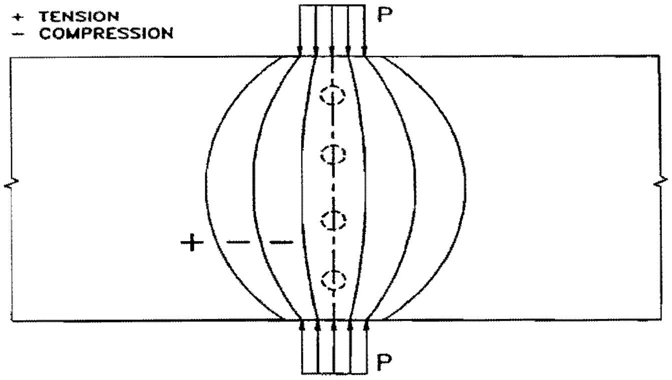

FIG. 25. Distribution of Transverse Normal Stress Due to Uniform Longitudinal and Banded Transverse Prestressing

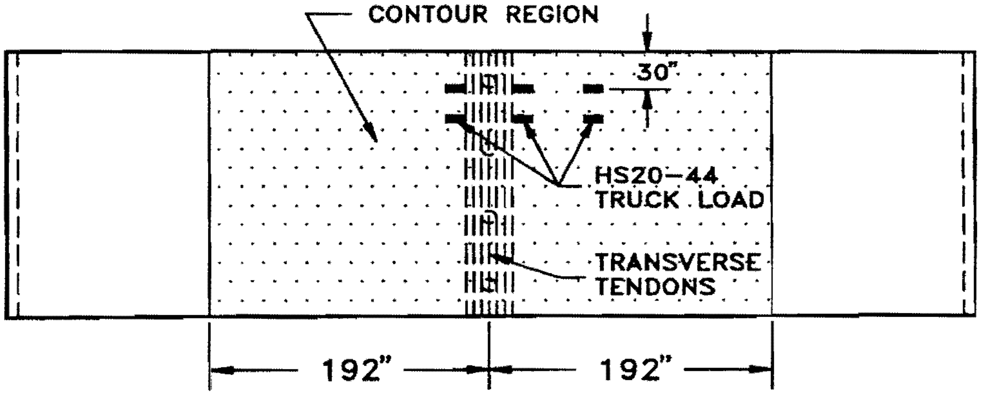

FIG. 26. Preliminary Load Location and Contour Area

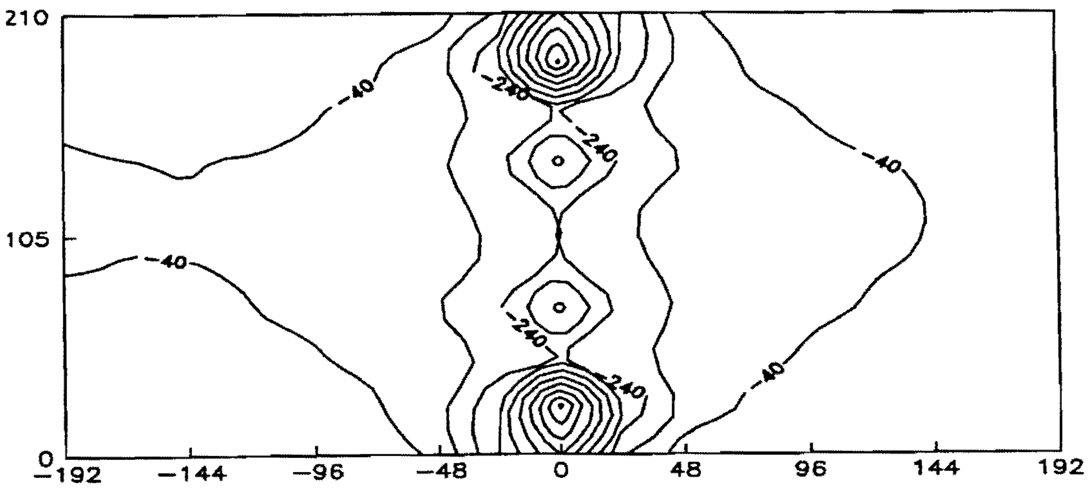

FIG. 27. Transverse Normal Stress Due to Dead Load and Prestressing

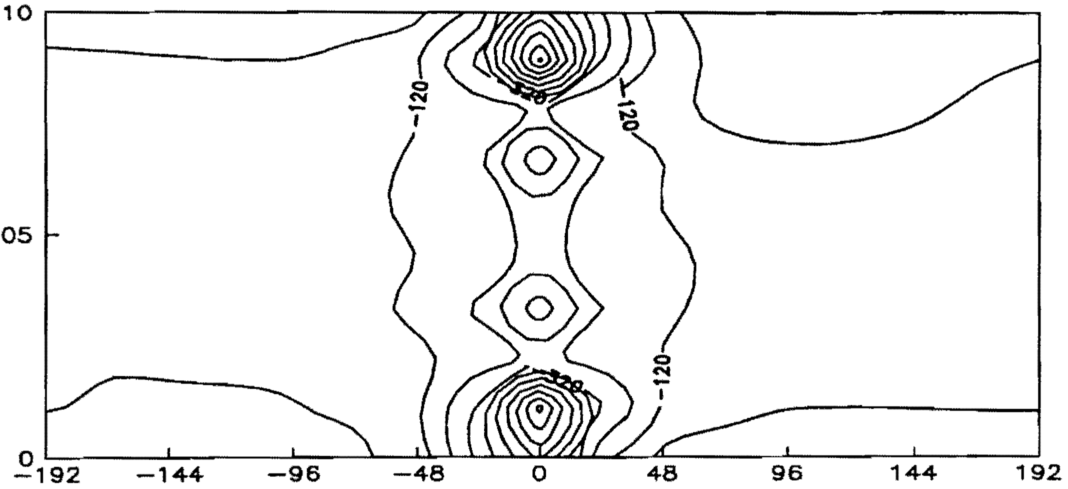

FIG. 28. Transverse Normal Stress Due to Dead Load, Prestressing, and Live Load

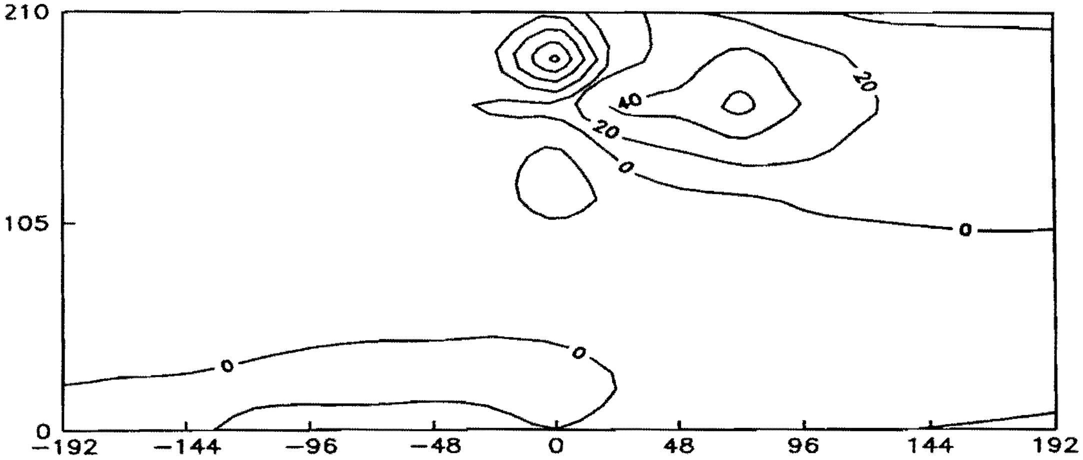

FIG. 29. Change in Transverse Normal Stress Due to Live Load

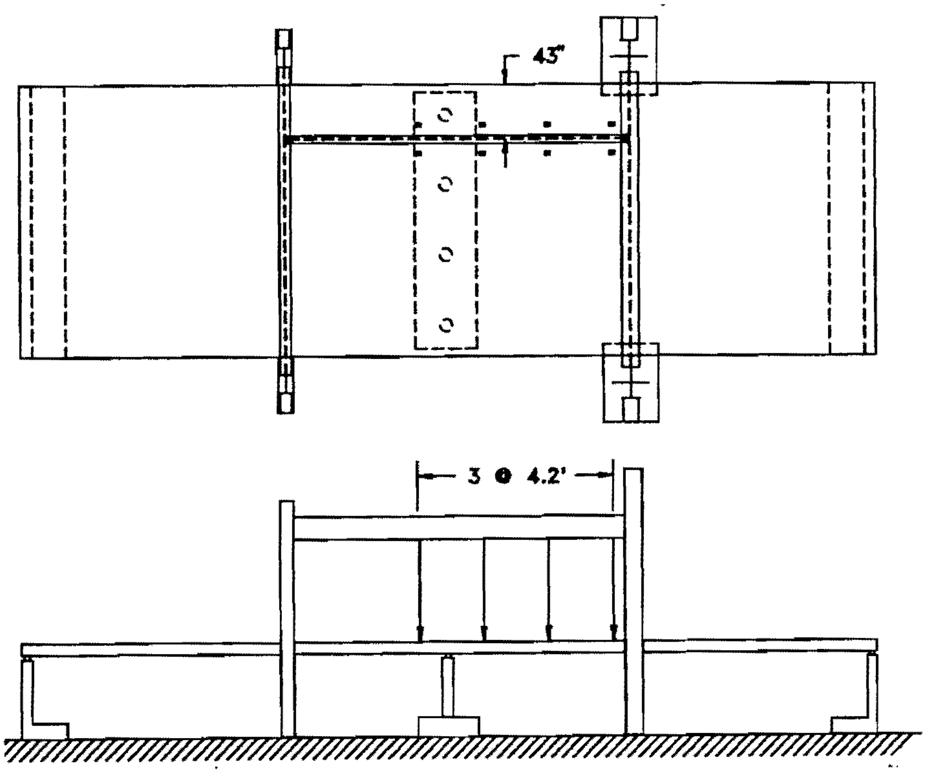

FIG. 30. Setup for Cyclic Load

Four MTS hydraulic actuators are used to apply the vertical loads. A beam attached to each actuator with a pin-connection is used to transfer the load to pressure pads that are spaced equidistant from the center of the truck's line of travel. These pads, which have the scaled dimensions of the area of contact of a truck tire, in turn apply load to the bridge deck. Spacing and magnitude of the loads are determined by applying geometric and loading scale factors, along with impact and overload factors, to the dimensions and load magnitudes of an AASHTO HS20-44 truck load (see Figs. 31(a) and (b)). The distance between actuators is equal to that of the wheelbase of the truck loading. This means that the actuator loads correspond to the given scaled truck loads at those instances in the loading cycle when the simulated truck coincides with the actuator locations. Also, the actuators are placed in a region of the slab that maximizes the change of stress in the high gradient regions. Impact is determined according to the following equation from AASHTO 3.8.2.1 (*Standard* 1989):

$$I = \frac{50}{L + 125} \quad \text{.......} (24)$$

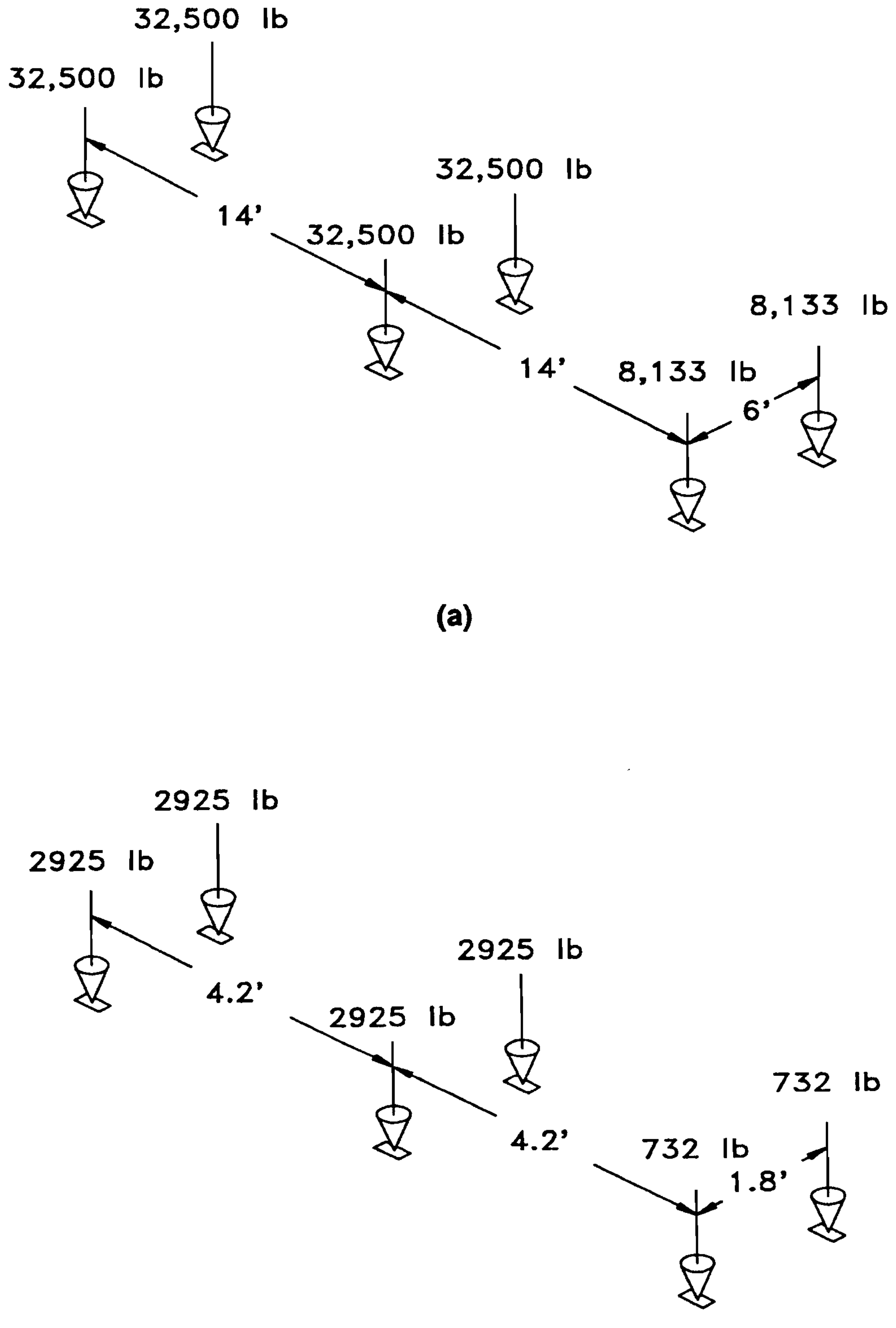

(a)

(b)

FIG. 31. Factored AASHTO Truck Load: (a) Full Scale; (b) 3/10 Scale

where I = impact fraction (maximum 30 percent); L = length in feet of the portion of the span that is loaded to produce the maximum stress (for L = 27.5 ft and I = 0.32, use 0.30). Overload is assumed as

$$\mathrm{OVL} = \frac{5}{3}(\mathrm{L} + \mathrm{I}) \quad \text{(25)}$$

where L is the live load.

To obtain the load-deflection relations for this test, a flexibility approach is used. The basic equation of flexibility is

$$\mathrm{P} \cdot f = \mathrm{u} \quad \text{(26)}$$

where P is an applied load at a specified location j on a structure, f is the deflection or flexibility coefficient at any location i due to a unit load applied at j, and u is the deflection at i due to the load P. Using superposition this relation may be expanded to include n load locations as follows:

$$\sum_{j=1}^{n} \mathrm{P}_j f_{ij} = \mathrm{P}_1 \cdot f_{i1} + \mathrm{P}_2 \cdot f_{i2} + \mathrm{P}_3 \cdot f_{i3} + \cdots + \mathrm{P}_n \cdot f_{in} = \mathrm{u}_i \quad \text{(27)}$$

In this study four actuators are used to apply load at the locations shown in Fig. 30. Therefore, four equations may be written to describe the behavior of the slab for each load case. Dividing the load applied by an actuator into two equal loads (two wheels per axle) results in the following equation for the average deflection under actuator 1:

$$\frac{\left[\mathrm{A}_1(f_{11a} + f_{11b}) + \mathrm{A}_2(f_{12a} + f_{12b}) + \mathrm{A}_3(f_{13a} + f_{13b}) + \mathrm{A}_4(f_{14a} + f_{14b})\right]}{2} = \frac{(\mathrm{u}_{1a} + \mathrm{u}_{1b})}{2} \quad \text{(28)}$$

where

A_j = load applied by actuator j, assuming $\mathrm{A}_j/2 = \mathrm{A}_{ja} = \mathrm{A}_{jb}$ with A_{ja} and A_{jb} being the loads that are transferred to the slab at actuator j;

f_{1ja} = flexibility coefficient at each actuator for left actuator load (left and right defined by looking in the direction of traffic);

f_{1jb} = flexibility coefficient at each actuator for right actuator load;

u_{1a} = deflection of slab at actuator 1 for left load;

u_{1b} = deflection of slab at actuator 1 for right load.

Similar equations may be written for the other three actuator locations. In matrix form the four equations become

$$\begin{bmatrix} (f_{11a}+f_{11b}) & (f_{12a}+f_{12b}) & (f_{13a}+f_{13b}) & (f_{14a}+f_{14b}) \\ (f_{21a}+f_{21b}) & (f_{22a}+f_{22b}) & (f_{23a}+f_{23b}) & (f_{24a}+f_{24b}) \\ (f_{31a}+f_{31b}) & (f_{32a}+f_{32b}) & (f_{33a}+f_{33b}) & (f_{34a}+f_{34b}) \\ (f_{41a}+f_{41b}) & (f_{42a}+f_{42b}) & (f_{43a}+f_{43b}) & (f_{44a}+f_{44b}) \end{bmatrix} \begin{Bmatrix} A_1 \\ A_2 \\ A_3 \\ A_4 \end{Bmatrix} = \begin{Bmatrix} (u_{1a}+u_{1b}) \\ (u_{2a}+u_{2b}) \\ (u_{3a}+u_{3b}) \\ (u_{4a}+u_{4b}) \end{Bmatrix} \quad \text{..........} (29)$$

Four equations may also be written that relate truck loads to the deflection at the actuator locations. In matrix form they become

$$\begin{bmatrix} (f^*_{11a}+f^*_{11b}) & (f^*_{12a}+f^*_{12b}) & (f^*_{13a}+f^*_{13b}) \\ (f^*_{21a}+f^*_{21b}) & (f^*_{22a}+f^*_{22b}) & (f^*_{23a}+f^*_{23b}) \\ (f^*_{31a}+f^*_{31b}) & (f^*_{32a}+f^*_{32b}) & (f^*_{33a}+f^*_{33b}) \\ (f^*_{41a}+f^*_{41b}) & (f^*_{42a}+f^*_{42b}) & (f^*_{43a}+f^*_{43b}) \end{bmatrix} \begin{Bmatrix} P_1 \\ P_2 \\ P_3 \end{Bmatrix} = \begin{Bmatrix} (u_{1a}+u_{1b}) \\ (u_{2a}+u_{2b}) \\ (u_{3a}+u_{3b}) \\ (u_{4a}+u_{4b}) \end{Bmatrix} \quad \text{..................................} (30)$$

where

P_j = axle load;

f^*_{ija} = flexibility coefficient at the actuator for the left wheel load;

f^*_{ijb} = flexibility coefficient at the actuator for the right wheel load.

Applying the condition that the deflections on the right side of Eq. 29 be equivalent to those on the right side of Eq. 30, leads to the following relationship for time t:

$$[f]\{A\} = [f^*]\{P\} \quad \text{..} (31)$$

Flexibility coefficients are determined using FEA by applying a load of 1 kip (4.5 kN) that is in-line with the locations of the actuator pads at 2 ft (0.61 m) intervals. Varying the location of the truck load by 2-ft (0.61-m) increments, beginning with the rear wheels at the right end of the bridge deck, and solving Eq. 31 for each location gives the resulting load curve shown in Fig. 32(a).

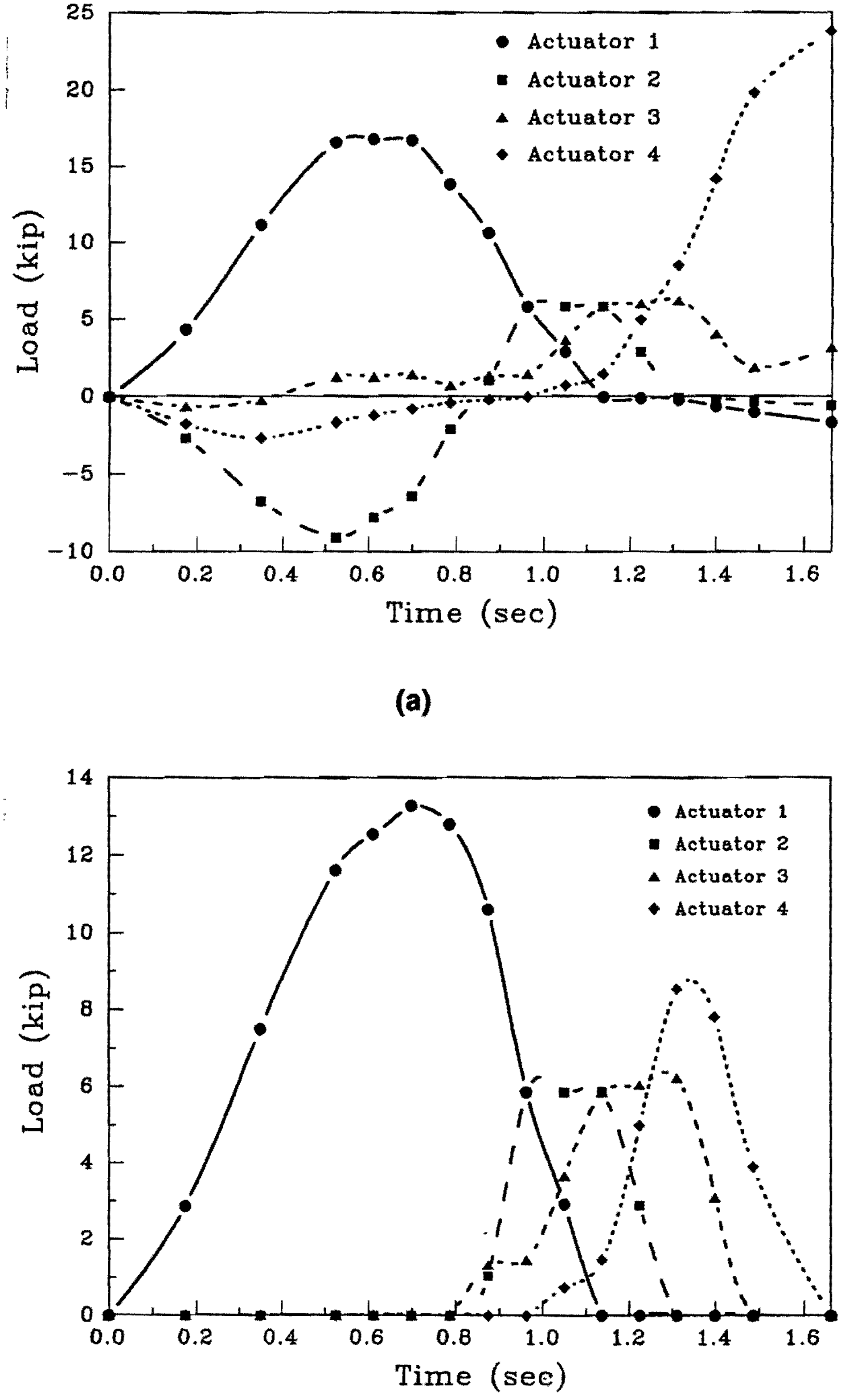

(a)

(b)

FIG. 32. Load Curves for Application of Cyclical Load: (a) Tensile Forces Allowed; (b) No Tensile Forces

Note the negative (tensile) values of load that result as the actuators try to create the complex curvature of the structure. Since the actuators may not apply tensile force to the slab, a further approximation must be incurred. Eq. 31 is solved for each truck location with only one, two, or three actuators applying load. The combinations which result in no tensile load are used to create the necessary deflections. The resulting load curve is shown in Fig. 32(b). Note that in the unmodified curves actuator 4 load becomes very high. This is due to the fact that one actuator is applying all of the load to achieve the deflection caused by the truck loads at midspan on the left side of the bent. Since this is not a realistic approximation, load is reduced to zero after the simulated truck moves past the center bent. Resulting vertical displacement of the slab at 21 ft (6.4 m) from the beginning of the bridge along a line that bisects the two lines of actuators is shown in Fig. 33. This result is compared to actual displacements later.

Mechanical constraints of load actuators determine the speed of load application. One full cycle, representing 38 ft (11.6 m) of travel by the scaled vehicle, may be applied in 1.6625 sec. By applying the scale factor for velocity (see Sec. 2.1), it is determined that this corresponds to a truck traveling on the prototype at 30 mph (48 km/h).

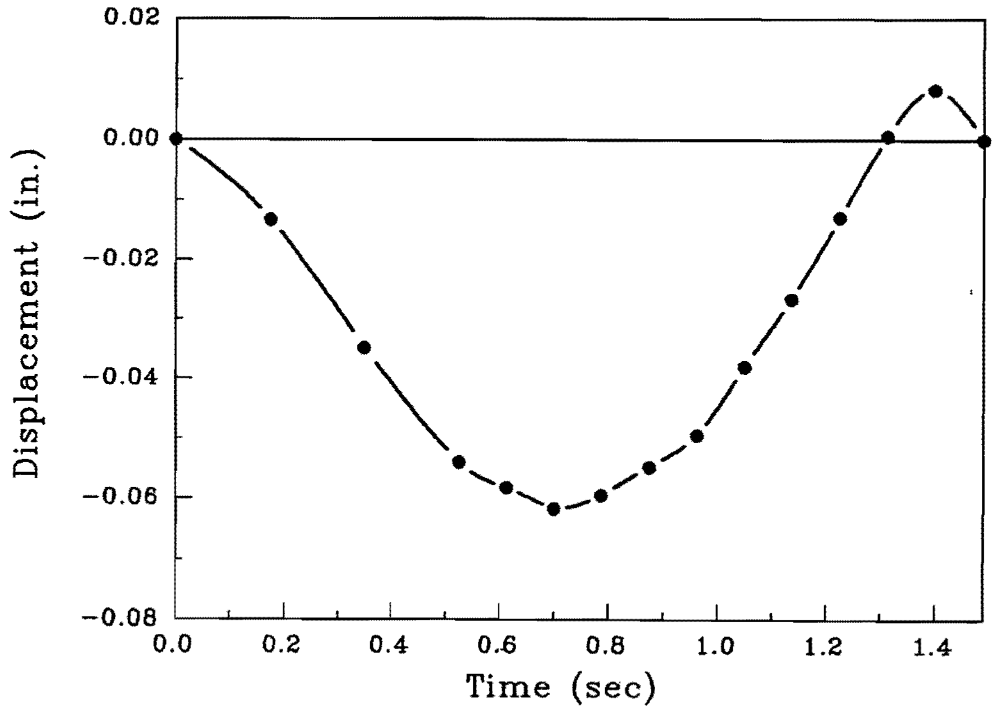

FIG. 33. Approximate Displacement of Slab Due to One Cycle of Load

Two aspects of the structure's response to repeated loading are studied: (1) change in strain with respect to the number of cycles and, (2) cracking of the top and bottom concrete surface. Strains are measured statically, applying load as if a truck were at rest at locations 3, 4, and 5, and dynamically during the first 100 cycles as a datum for comparison. Thereafter strains are measured every 10,000 cycles: statically, as before, and dynamically for several cycles in order to establish a pattern of strain variation. Cracking is monitored while the static load is being applied.

The objective of this test is to better understand the effect of repeated loading on regions of stress transition caused by banded prestressing. 200,000 cycles of load are applied at each actuator location.

8. PRESENTATION OF RESULTS

8.1 Shrinkage

In order to eliminate shrinkage strains from the total time-dependent strains and as a result isolate strains due to loads on the structure, shrinkage is monitored. This is done prior to prestressing the slab and in a continuous manner by means of a control specimen that is external from the slab. Table 7 shows strain measurements for the longitudinal and transverse direction on the slab, and the control specimen. Fig. 34 shows these results graphically, along with the curve predicted by the ACI Eq. 18 (ε_{shu} = 500 μin./in.; s = 5 in.; K_h = 1.0; and H = 50%). It is shown that most shrinkage in Model 2 occurs during the early life of the concrete, a well established characteristic. However, the ACI formula assumes moist curing for 7 days and predicts a lower rate of shrinkage strain for the early life of the structure. The measured shrinkage shows that steps taken to cure the model did not prevent shrinkage prior to the end of the 7 day curing period. Shrinkage values are not shown for the slab locations after 20 days, because prestressing occurs at that time. Shrinkage readings for the control specimen at 57 and 91 days are very close to predictions of the ACI formula. Therefore, for long term considerations the ACI values are used to eliminate the shrinkage strains from the total time-dependent strains recorded in the model.

Table 7. Measurement of Shrinkage Strain

Time (day) (1)	Control (in./in.) (2)	46X (in./in.) (3)	46Y (in./in.) (4)	ACI[1] (in./in.) (5)
1	-84	-142	-125	—
14	-222	-193	-205	-76
15	-196	-185	-200	-84
16	-225	-214	-230	-93
17	-232	-194	-209	-101
20	-240	-184	-236	-123
57	-275	—[2]	—[2]	-267
91	-316	—	—	-320

[1] ACI Committee 209 equation (see Eq. 32)

[2] Measurements on the slab include prestressing after day 20

Note: 1 in. = 2.54 cm

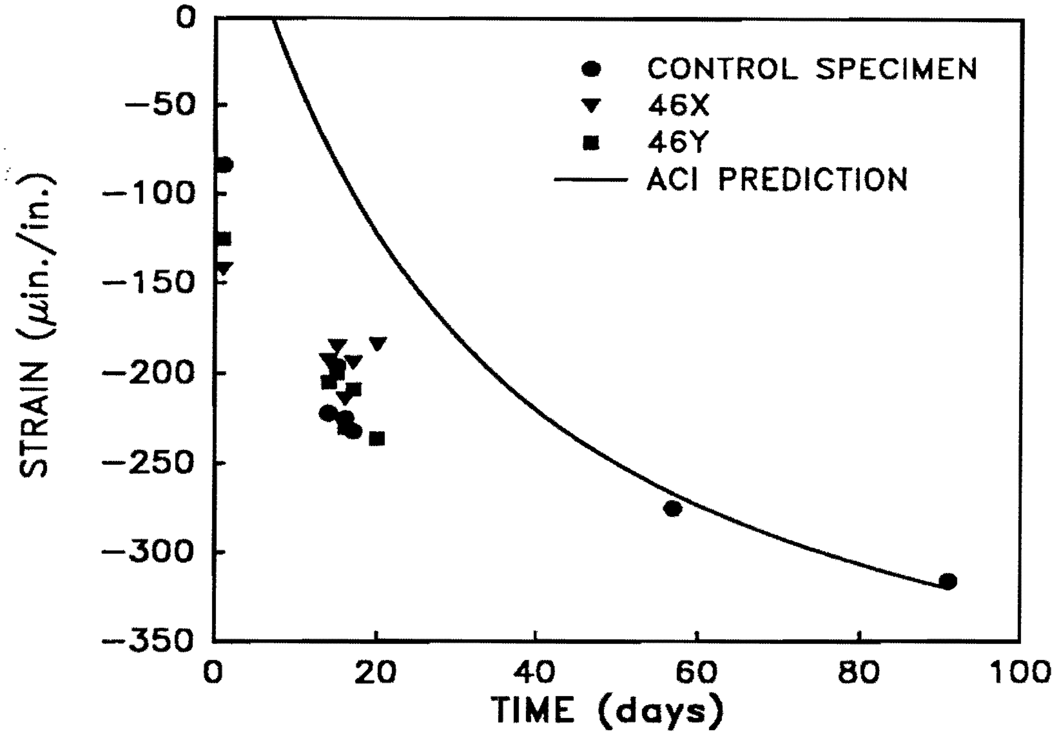

FIG. 34. Measured and Calculated Shrinkage Strain

8.2 Prestressing and Dead Load

Prestressing of the model is accomplished as described in section 7.1. Elongation measurements range from 4.25 in. (10.8 cm) to 4.875 in. (12.4 cm), with an average value of 4.55 in. (11.55 cm), and a standard deviation of 0.15 in. (0.38 cm). Target elongation for the required prestress force is 4.6 in. (11.7 cm). Unfortunately, only one of the strain gages mounted on the prestressing strand survived construction of the model. Therefore, study of the frictional characteristics of the tendon is inconclusive. However, strain readings from the one gage, coupled with pressure gage readings from the dead end jacking procedure (see section 7.1) indicate that friction coefficients are comparable to values normally used for determination of prestressing force. Values used in the analysis for this study are taken as $K = 0.0002/\text{in.}$ (0.008/m), and $\mu = 0.35/\text{radian}$.

Structural integrity of the slab is maintained throughout the prestressing operation. Cracking of the concrete did not occur during the transverse or longitudinal prestressing operation.

The measured response of the slab and a comparison with FEM's predictions of that response, both initial and time-dependent, are shown in the following.

8.2.1 Effects of Transverse Prestress

Of primary concern is the distribution of strain and stress due to the banded transverse prestressing force. Figs. 35 - 38 show distribution of the transverse strain near the top surface of the slab as measured by the embedded strain gages and predicted by FEM for prestressing force applied by 1, 3, 5, and 7 transverse tendons, respectively. Numerically predicted values are represented by the contour lines, and the measured values are shown as point values. Missing values are due to gage failure as a result of construction. See Table 8 for corresponding strain values at the gage locations.

Fig. 39 shows a further comparison of measured strain with predictions of FEM and elasticity theory as described in the first report of this series (Roschke and Inoue 1990). Longitudinal sections are taken through the strain gage locations. Predictions of FEM and elasticity theory both concur with experimental values. Observations made in the previous report also apply for this study.

8.2.2 Effects of Total Prestress and Dead Load

Predicting the response of a post-tensioned structure to self weight is difficult even under optimal circumstances. In this study the large amount of dead load necessary to achieve similar strains in the laboratory model as in the prototype requires that the longitudinal prestressing and the dead load be applied in two steps. This is necessary to prevent cracking that may reduce ultimate strength. Also, it is not possible to numerically model the interaction of the formwork with the structure during the initial prestressing procedure. Further complicating the analysis is the differential vertical displacement experienced at the support columns after removal of the formwork supporting the slab, see Fig. 40. Along with these deflection measurements, load cell readings at the supports did provide reactions that allow the use of boundary elements (van Gruenen 1979) to model displacement of the columns.

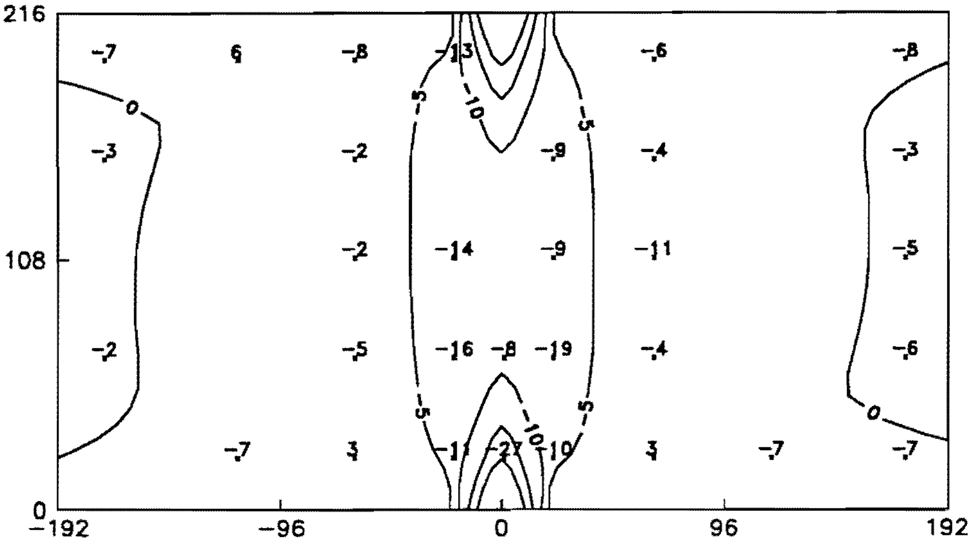

FIG. 35. Top Surface Transverse Strain with One Transverse Tendon Stressed

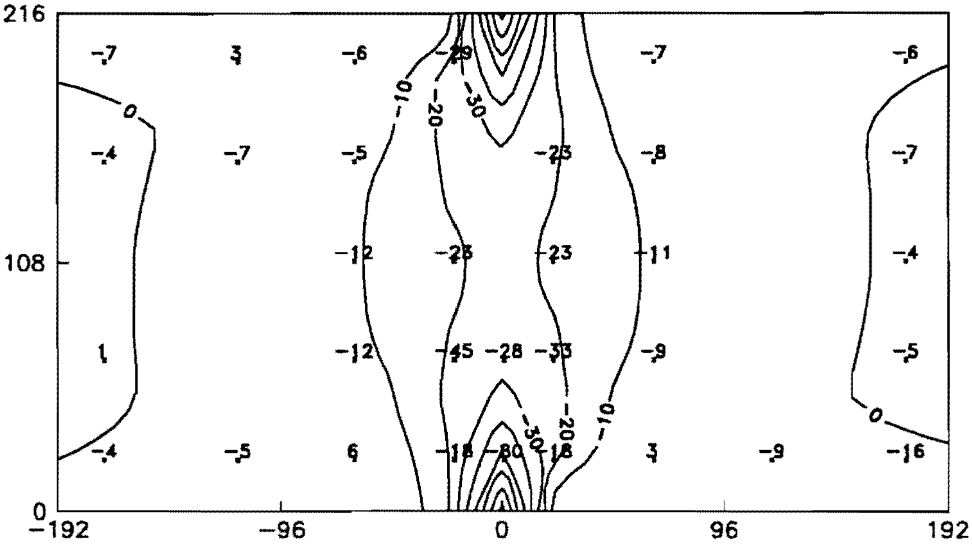

FIG. 36. Top Surface Transverse Strain with Three Transverse Tendons Stressed

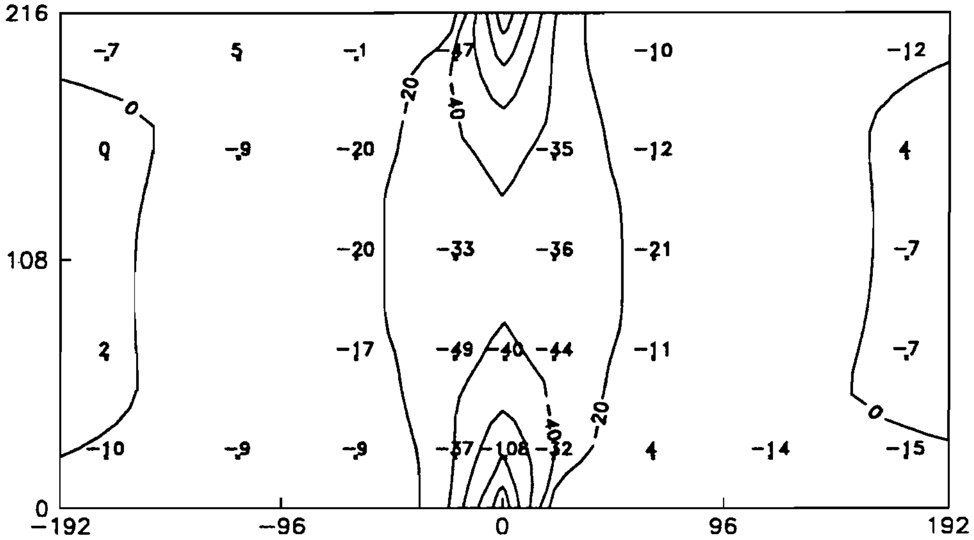

FIG. 37. Top Surface Transverse Strain with Five Transverse Tendons Stressed

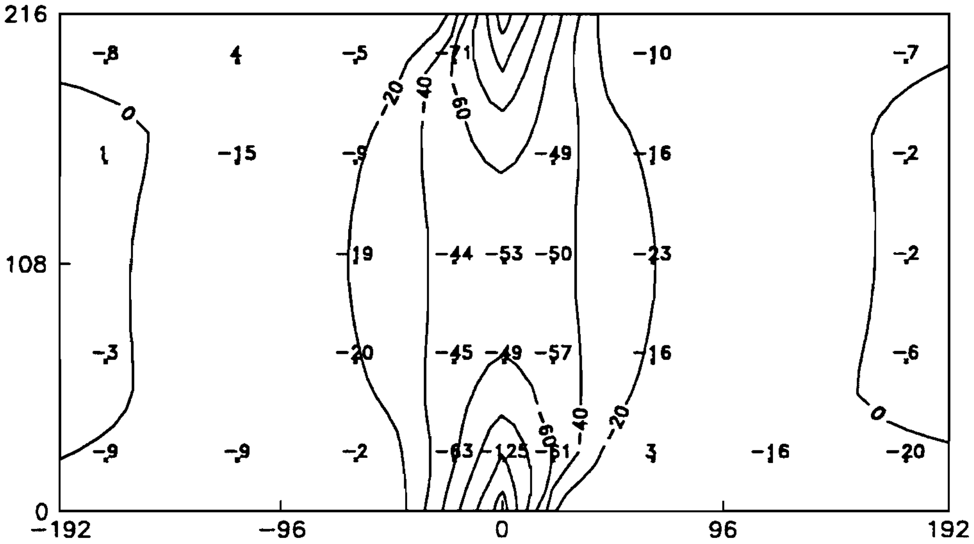

FIG. 38. Top Surface Transverse Strain with Seven Transverse Tendons Stressed

TABLE 8. Experimental and FEM Strains Due to Transverse Prestress Force

	Experimental Strain (μin./in.)				FEM Strain (μin./in.)			
Gage Location (1)	1 Tendon (2)	3 Tendons (3)	5 Tendons (4)	7 Tendons (5)	1 Tendon (6)	3 Tendons (7)	5 Tendons (8)	7 Tendons (9)
1	-17	-4	-10	-9	0	0	0	0
2	-2	1	2	-3	0	0	0	0
3	-	-	-	-	0	0	0	0
4	-3	-4	0	1	0	0	0	0
5	-7	-7	-7	-8	0	0	0	0
6	-7	-5	-9	-9	0	0	-1	-1
7	-	-	-	-	0	-1	-2	-3
8	-	-	-	-	-1	-2	-3	-4
9	-22	-7	-9	-15	0	-1	-2	-3
10	6	3	5	4	0	0	-1	-1
11	3	6	-9	-2	0	-2	-3	-4
12	-5	-12	-17	-20	-2	-7	-12	-17
13	-2	-12	-20	-19	-3	-9	-15	-21
14	-2	-5	-20	-9	-2	-7	-11	-17
15	-8	-6	-1	-5	0	-1	-2	-3
16	-11	-18	-37	-63	-7	-22	-39	-57
17	-16	-45	-49	-45	-7	-21	-36	-50
18	-14	-23	-33	-44	-7	-19	-32	-45
19	-	-	-	-	-8	-22	-37	-52
20	-13	-29	-47	-71	-8	-24	-43	-63
21	-27	-80	-108	-125	-21	-56	-85	-106
22	-8	-28	-40	-49	-9	-27	-45	-61
23	-	-	-	-	-7	-22	-36	-50
24	-	-	-	-	-9	-27	-45	-61
25	-	-	-	-	-21	-56	-84	-106
26	-10	-18	-32	-61	-7	-24	-43	-62
27	-19	-33	-44	-57	-7	-22	-37	-52
28	-9	-23	-36	-50	-7	-19	-32	-45
29	-9	-23	-35	-49	-7	-21	-36	-50
30	-	-	-	-	-7	-22	-39	-58
31	3	3	4	3	0	-1	-2	-3
32	-4	-9	-11	-16	-2	-7	-12	-17
33	-11	-11	-21	-23	-3	-9	-15	-21
34	-4	-8	-12	-16	-2	-7	-12	-17
35	-6	-7	-10	-10	-1	-2	-3	-5
36	-7	-9	-14	-16	0	0	-1	-1
37	-	-	-	-	0	-1	-2	-3
38	-	-	-	-	-1	-2	-3	-4
39	-	-	-	-	0	-1	-2	-3
40	-	-	-	-	0	0	-1	-1
41	-7	-16	-15	-20	0	0	0	0
42	-6	-5	-7	-6	0	0	0	0
43	-5	-4	-7	-2	0	0	0	0
44	-3	-7	4	-2	0	0	0	0
45	-8	-6	-12	-7	0	0	0	0

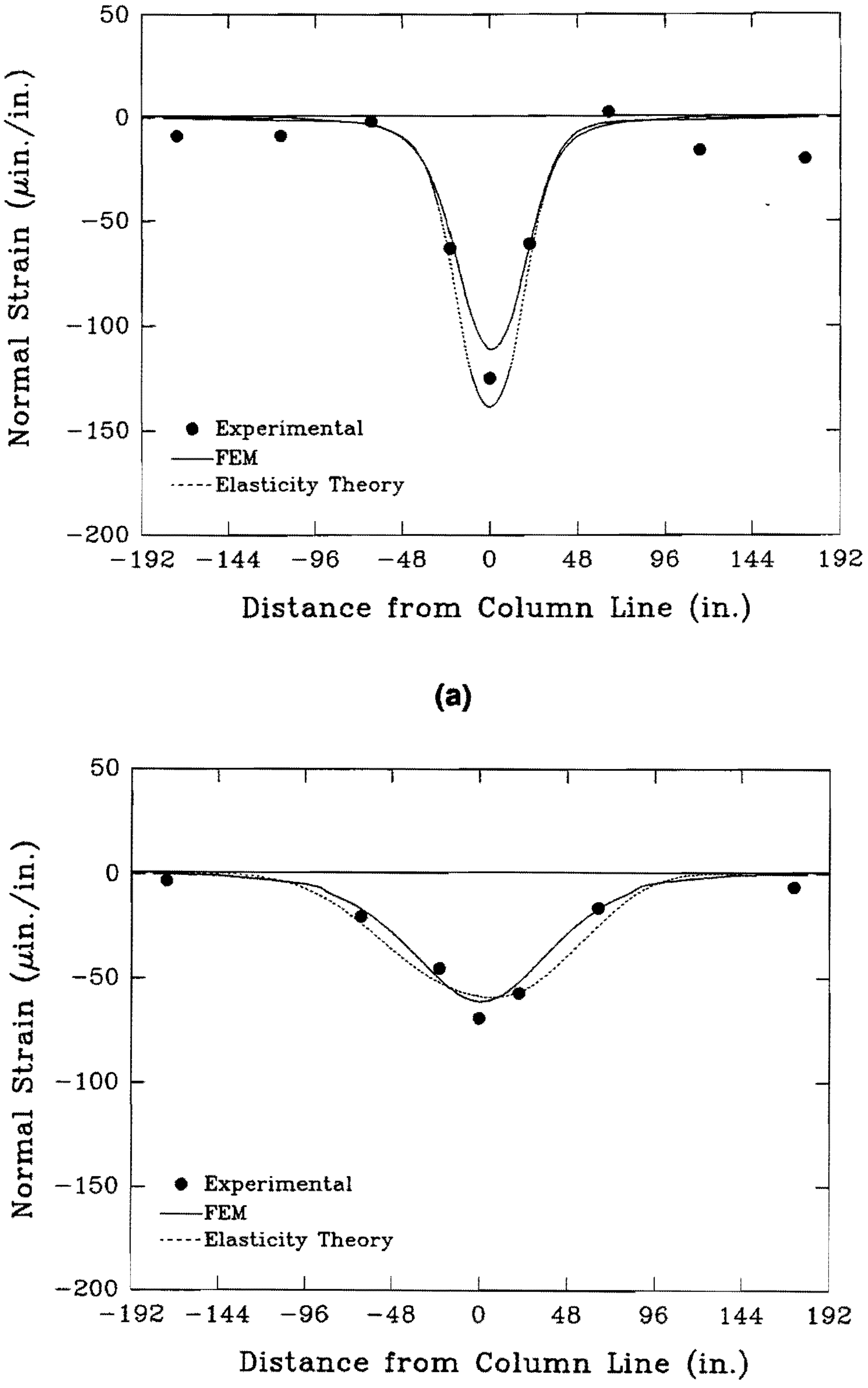

(a)

(b)

FIG. 39. Comparison of Transverse Strains: (a) Gages 1, 6, 11, 16, 21, 26, 31, 36, and 41; (b) Gages 2, 7, 12, 17, 22, 27, 32, 37, and 42

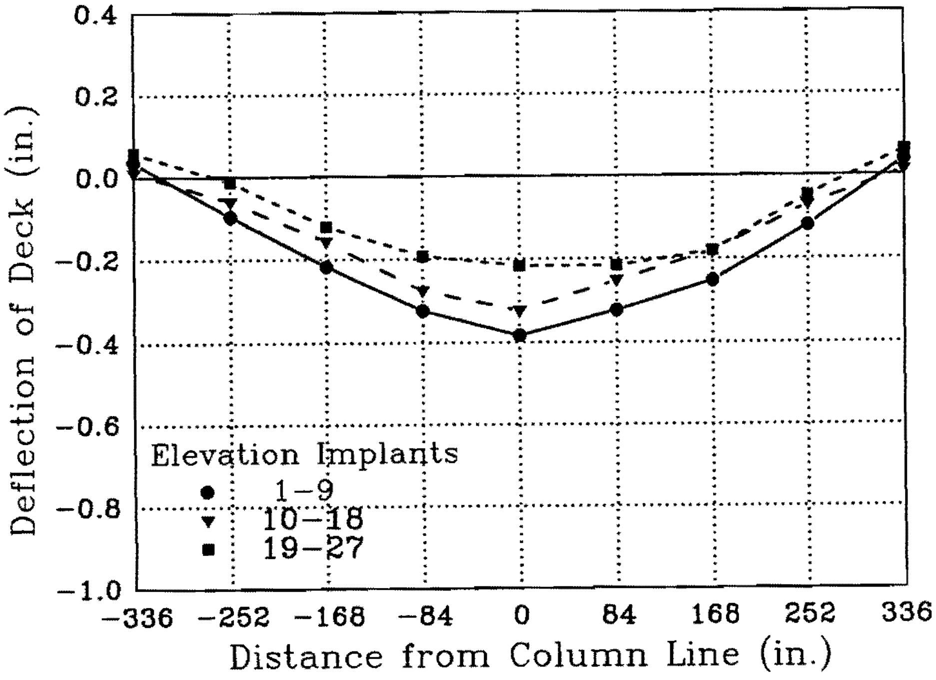

FIG. 40. Deflection of Bridge Deck Due to Longitudinal and Transverse Prestressing and Dead Load

Finally, along with other factors the time-dependent creep strain is a function of the initial elastic strain created by each loading. Figs. 41 - 42 are contour plots of predicted top and bottom surface strains, respectively, in the transverse and longitudinal directions at 79 days after casting. The analogous comparison at 310 days after casting is shown in Fig. 43. Tables 9 and 10 provide a complete listing of experimental and FEM normal strains at 79 and 319 days, respectively, after casting. Strains predicted by FEM due to loading and time-dependent effects of shrinkage and creep are greater than those measured in the model. This results in a conservative estimate of prestress loss. These tables and figures show that direct comparison of strains measured in the model with those predicted by FEM does not give conclusive evidence that FEM can accurately predict response of the structure due to the different loading steps of construction and creep.

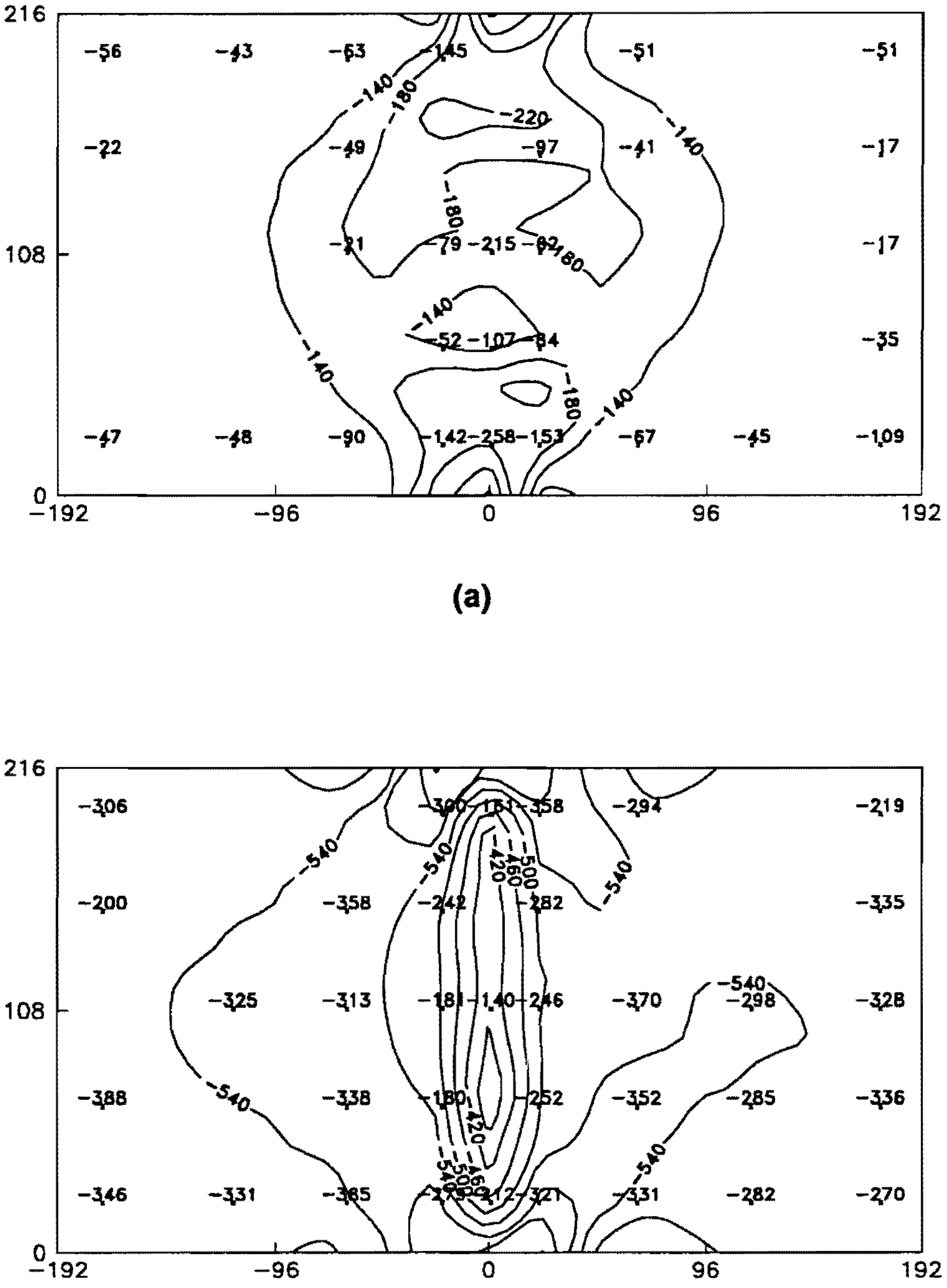

(a)

(b)

FIG. 41. Strains near Top Surface due to Longitudinal and Transverse Prestressing and Dead Load at 79 Days After Casting: (a) Transverse; (b) Longitudinal

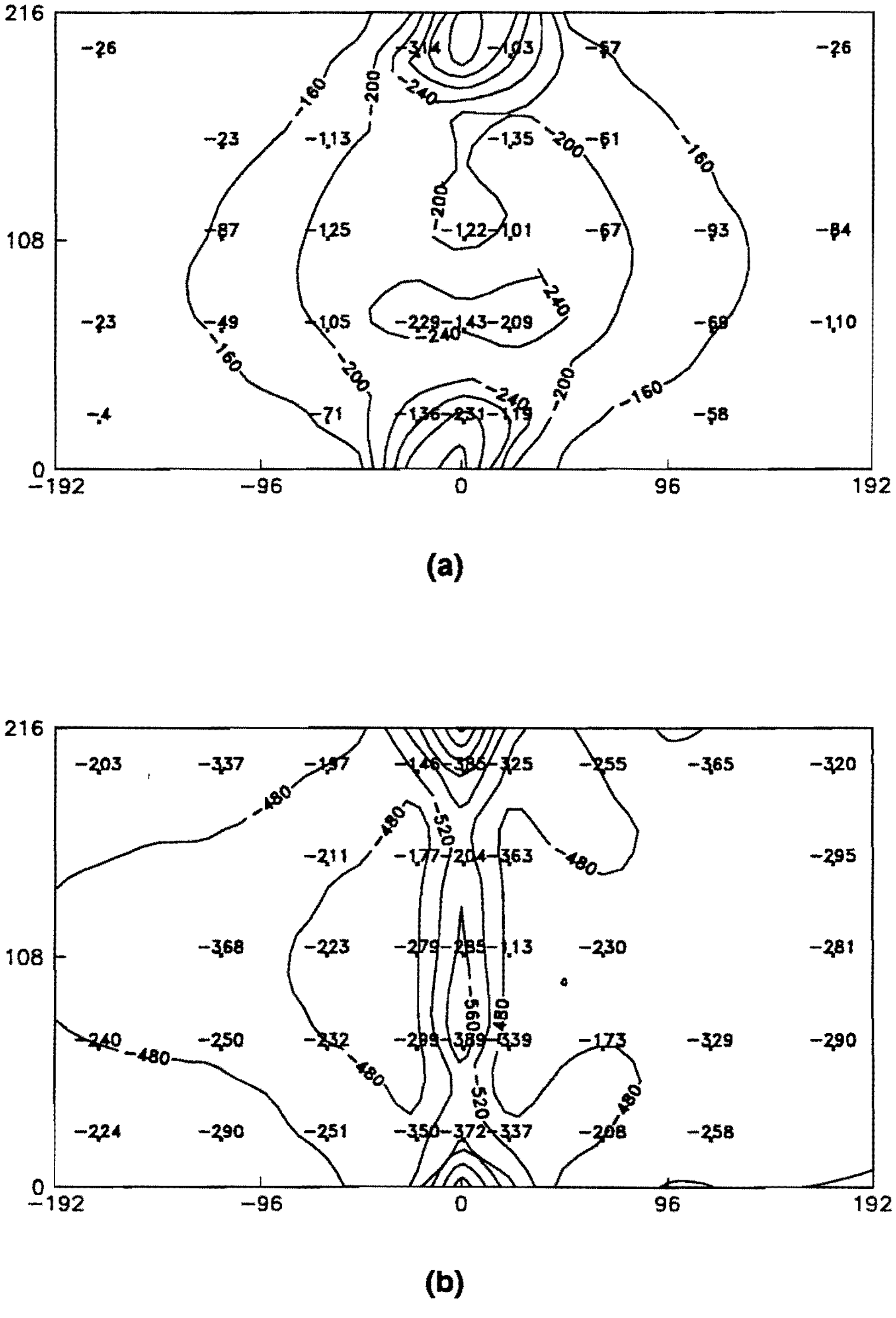

FIG. 42. Strains near Bottom Surface due to Longitudinal and Transverse Prestressing and Dead Load at 79 Days After Casting: (a) Transverse; (b) Longitudinal

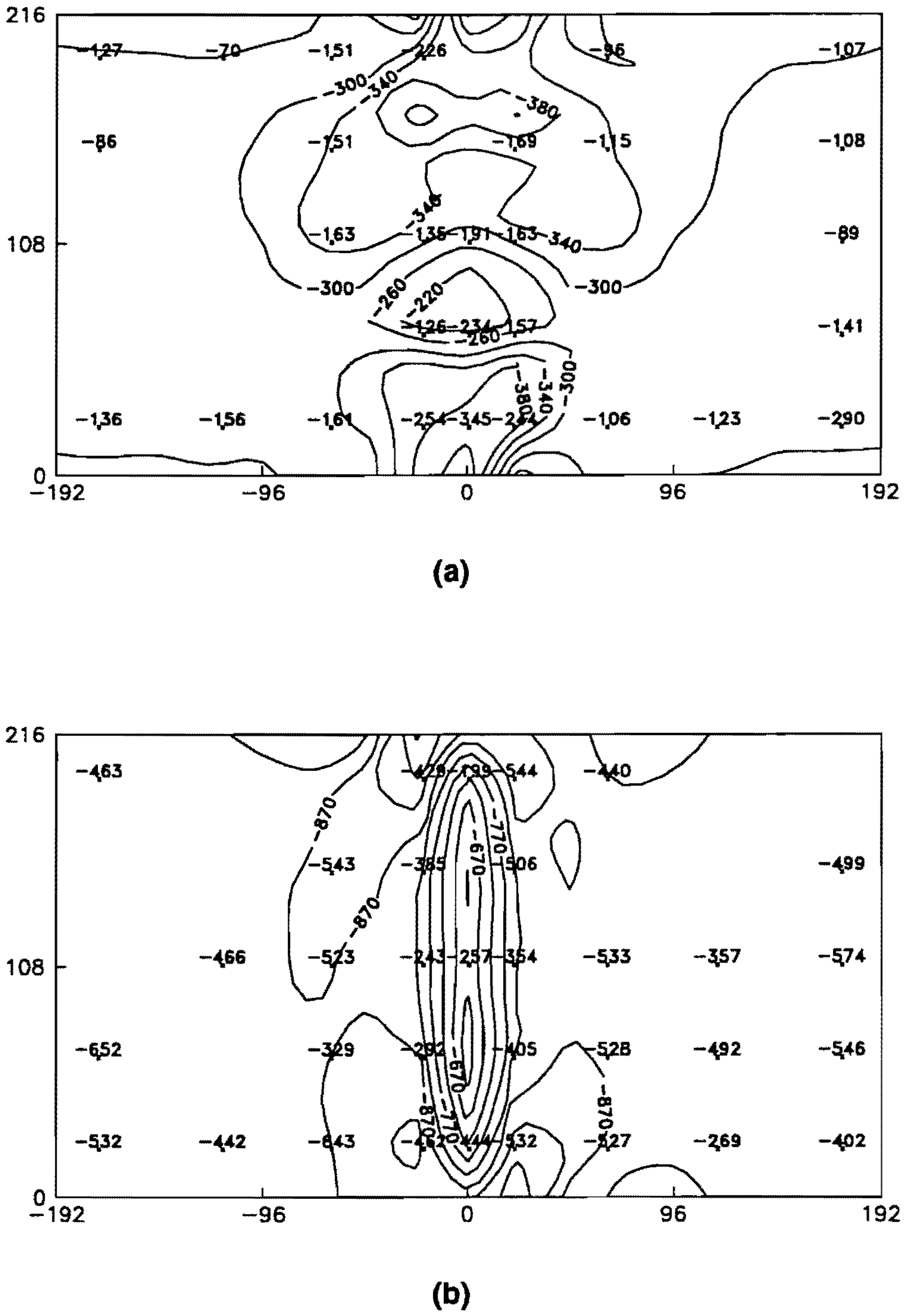

FIG. 43. Strains near Top Surface due to Longitudinal and Transverse Prestressing and Dead Load at 310 Days After Casting: (a) Transverse; (b) Longitudinal

TABLE 9. Experimental and FEM Strains at 79 Days after Casting

Gage Location (1)	Experimental Strain (μin./in.)		FEM Strain (μin./in.)		Experimental Strain (μin./in.)		FEM Strain (μin./in.)	
	TY[a] (2)	BY[b] (3)	TY[a] (4)	BY[b] (5)	TX[c] (6)	BX[d] (7)	TX[c] (8)	BX[d] (9)
1	-47	-4	-124	-146	-346	-224	-522	-467
2	-	-23	-116	-150	-388	-240	-533	-479
3	-	-	-116	-148	-	-	-537	-486
4	-22	-	-118	-145	-200	-	-532	-480
5	-56	-26	-125	-144	-306	-203	-523	-467
6	-48	-	-125	-150	-331	-290	-522	-467
7	-	-49	-126	-165	-	-250	-540	-484
8	-	-87	-134	-166	-325	-368	-544	-490
9	-	-23	-129	-154	-	-	-540	-488
10	-43	-	-125	-146	-	-337	-519	-467
11	-90	-71	-125	-162	-385	-251	-527	-489
12	-	-105	-150	-204	-338	-232	-554	-488
13	-21	-125	-180	-214	-313	-223	-543	-466
14	-49	-113	-165	-182	-358	-211	-555	-495
15	-63	-	-113	-153	-	-197	-528	-489
16	-142	-136	-200	-271	-279	-350	-583	-505
17	-52	-229	-164	-224	-180	-299	-520	-464
18	-79	-	-203	-180	-181	-279	-507	-465
19	-	-	-208	-200	-242	-177	-503	-459
20	-145	-314	-197	-290	-300	-146	-602	-520
21	-258	-231	-238	-339	-212	-372	-459	-571
22	-107	-143	-160	-218	-	-389	-362	-565
23	-215	-122	-190	-171	-140	-285	-387	-572
24	-	-	-197	-181	-	-204	-386	-541
25	-	-47	-214	-364	-161	-385	-428	-604
26	-153	-119	-210	-280	-321	-337	-592	-513
27	-84	-209	-174	-233	-252	-339	-491	-456
28	-62	-101	-205	-178	-246	-113	-496	-463
29	-97	-135	-198	-190	-282	-363	-505	-466
30	-	-103	-187	-285	-358	-325	-564	-511
31	-67	-	-113	-155	-331	-208	-516	-479
32	-	-	-150	-200	-352	-173	-547	-483
33	-	-67	-182	-217	-370	-230	-531	-458
34	-41	-61	-167	-189	-	-	-538	-485
35	-51	-57	-126	-164	-294	-255	-514	-481
36	-45	-58	-124	-151	-282	-258	-515	-449
37	-	-69	-124	-163	-285	-329	-538	-468
38	-	-93	-135	-168	-298	-	-541	-472
39	-	-	-134	-159	-	-	-535	-469
40	-	-3	-128	-150	-	-365	-518	-451
41	-109	-	-125	-148	-270	-	-524	-445
42	-35	-110	-117	-151	-336	-290	-534	-458
43	-17	-84	-117	-150	-328	-281	-538	-464
44	-17	-	-120	-149	-335	-295	-533	-460
45	-51	-26	-126	-147	-219	-320	-524	-447

[a] TY = Transverse direction, top layer
[b] BY = Transverse direction, bottom layer
[c] TX = Longitudinal direction, top layer
[d] BX = Longitudinal direction, bottom layer

TABLE 10. Experimental and FEM Strains at 310 Days after Casting

Gage Location (1)	Experimental Strain (µin./in.) TY[a] (2)	Experimental Strain (µin./in.) BY[b] (3)	FEM Strain (µin./in.) TY[a] (4)	FEM Strain (µin./in.) BY[b] (5)	Experimental Strain (µin./in.) TX[c] (6)	Experimental Strain (µin./in.) BX[d] (7)	FEM Strain (µin./in.) TX[c] (8)	FEM Strain (µin./in.) BX[d] (9)
1	-136	-84	-291	-326	-532	-462	-844	-745
2			-273	-345	-652	-754	-855	-758
3			-275	-341			-859	-767
4	-86		-284	-332			-852	-761
5	-127	-72	-297	-326	-463	-336	-841	-744
6	-156		-287	-325	-442	-445	-841	-757
7		-142	-273	-375		-415	-859	-765
8		-152	-294	-366	-466	-367	-862	-781
9			-298	-342		-668	-858	-776
10	-70		-297	-326		-369	-834	-747
11	-161		-292	-328	-643	-284	-864	-784
12			-267	-431	-329	-257	-866	-792
13	-163		-356	-427	-523	-358	-877	-751
14	-151		-343	-369	-543	-279	-880	-800
15	-151		-278	-334		-326	-841	-779
16	-254		-380	-439	-462	-533	-916	-832
17	-126		-271	-426	-292	-336	-855	-792
18	-135		-329	-385	-243	-361	-815	-779
19			-384	-363	-385	-231	-810	-764
20	-226	-486	-366	-494	-429	-393	-946	-842
21	-345		-418	-498	-444	-567	-723	-945
22	-234		-246	-416		-405	-591	-938
23	-191		-295	-387	-257		-602	-945
24		-393	-352	-340		316	-610	-886
25			-377	-550	-199	-410	-695	-975
26	-244	-129	-395	-462	-532	-595	-940	-842
27	-157	-219	-283	-439	-405	-805	-811	-776
28	-163	-256	-319	-379	-354	-235	-811	-780
29	-169	-86	-370	-348	-506		-812	-777
30		-141	-358	-476	-544	-491	-883	-837
31	-106		-277	-319	-527	-422	-852	-764
32		-229	-267	-425	-528	-491	-864	-794
33		-79	-359	-430	-533	-341	-861	-742
34	-115	-89	-346	-378			-855	-790
35	-96	-91	-297	-348	-440	-536	-820	-773
36	-123	-178	-286	-323	-269	-356	-833	-737
37			-267	-373	-492	-376	-858	-749
38		-119	-294	-370	-357		-858	-761
39			-305	-349		-532	-850	-753
40			-301	-329		-424	-830	-730
41	-290	-103	-293	-324	-402	-463	-848	-720
42	-141	-256	-272	-345	-546	-485	-858	-733
43	-89		-276	-344	-574	-493	-861	-743
44	-108		-287	-336	-499	-448	-852	-737
45	-107		-299	-328		-434	-841	-720

[a] TY = Transverse direction, top layer

[b] BY = Transverse direction, bottom layer

[c] TX = Longitudinal direction, top layer

[d] BX = Longitudinal direction, bottom layer

Comparison of top surface strains with bottom surface strains indicates that the structure is very well "load balanced," i.e., top and bottom strains are of the same magnitude at mid-span and, therefore, dead load moment is balanced by prestress moment (see Figs. 41 and 42). Also, as seen in Fig. 40, if the center bent did not displace vertically there would be very small initial deflections at the mid-spans. Since creep strain is a function of initial strain, if strain through the thickness of the slab is constant at the time of loading, then the creep strain occurs in the plane of the slab, and change in deflection of the slab is a result of loss of force in the prestressing steel. Changes in normal strain from 79 days to 310 days indicate that this loss would amount to approximately 0.03% of the initial prestress force. This loss would result in only a small amount of additional deflection. Fig. 44 indicates that this is the case since only small differential deflection of the bridge deck are observed between 14 and 230 days. Maximum change in deflection of the slab is approximately 0.06 in. (0.15 cm). This corresponds to 0.2 in. (0.5 cm) for a full scale structure. Because time-dependent effects are not a large factor in the vertical deflection of the laboratory slab, the analysis should accurately predict deflection at any time. As an example Fig. 45 shows a very good comparison of FEM's predicted deflection with measured values at 310 days after casting.

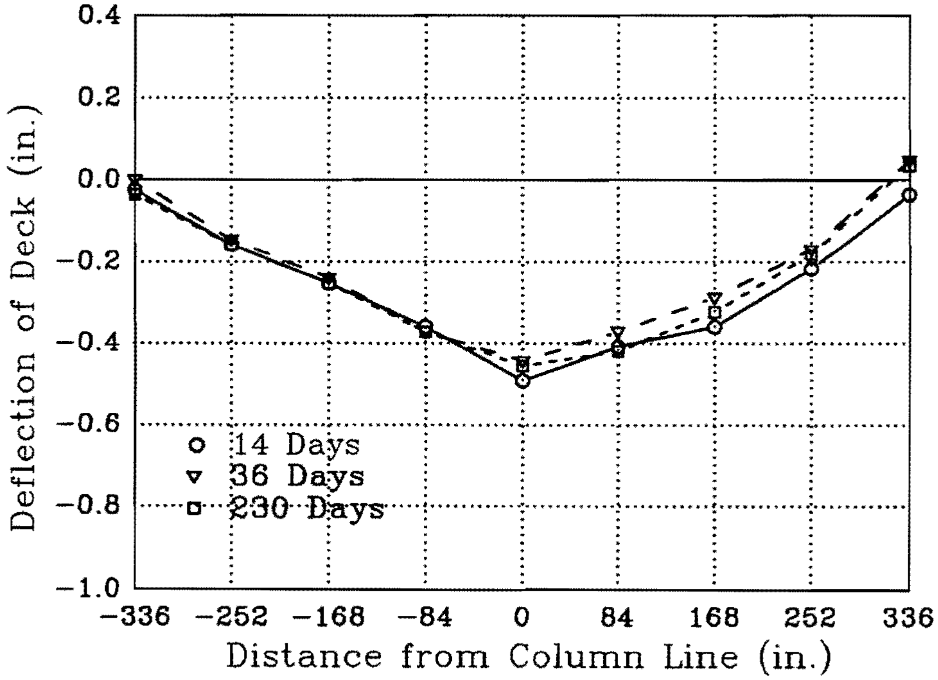

FIG. 44. Deflection of Bridge Deck due to Time-Dependent Effects

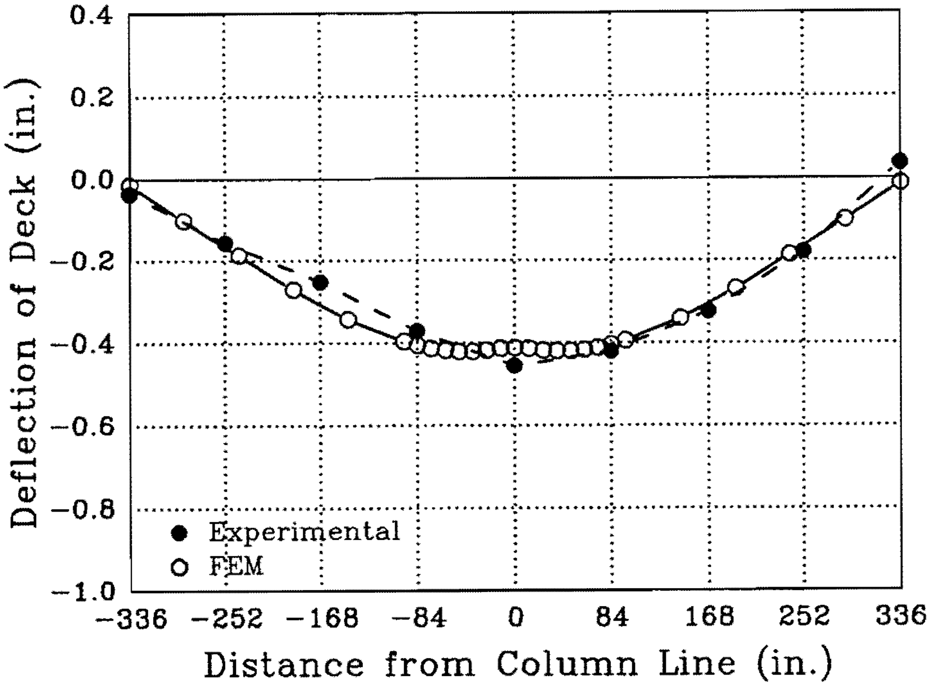

FIG. 45. Deflection of Bridge Deck 3' from the Edge

It is possible to make some general observations about the time-dependent behavior of the model by studying the strain measurements. Loading is not as complicated near the edge of the slab at the column line in the transverse direction. Fig. 46 shows a comparison of measurements of creep strain for gage locations 21 and 26 with those predicted using ACI Committee 209 recommendations (ACI 1971). More of the loading phases are incorporated in determining the strain history at these gage locations than are possible with the analysis program. This is accomplished using measured strain readings at each phase. Shrinkage strains and instantaneous strain are removed from the measured values shown. Although an exact relationship is still not made, normal strains due to creep are of the same order of magnitude. NOPARC also uses the ACI recommendations and should be able to predict creep strains for structures that have less complicated construction procedures.

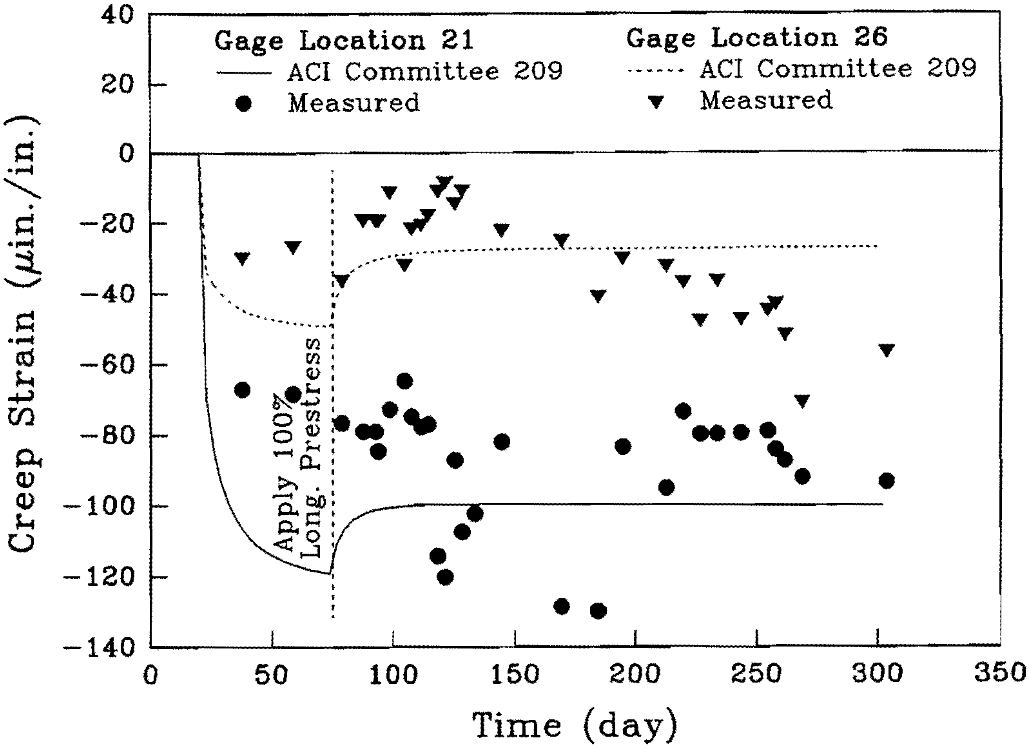

FIG. 46. Comparison of Measured and Predicted Creep Strain

Shear lag is a problem in structures that have regions of high stress gradients. At and near the edge of the slab around the banded transverse prestressing, such a region exists. Fig. 47 shows shearing strains calculated from strains measured at gage locations 26 and 31. Shearing strain at both locations changes at a similar rate with respect to time; this contrasts with the fact that longitudinal strain due to creep increases at a higher rate than the transverse strain due to creep. However, the shearing strain at location 31, which is opposite in sign to that at location 26, has a larger value. This larger strain could cause distress at this location, which was studied during the repetitive load test (see section 8.4).

8.3 AASHTO Design Loads

As mentioned previously, this test is to determine the response of the structure to design live loads, and to test the accuracy of the analysis program in predicting the response. To maximize the effect of the applied loads, 2 lanes of load are placed on the edge of the slab. This is to achieve maximum deflection, and create the largest tensile strain in the transverse direction between two outside columns. Initial loading with the described live loads resulted in strains too low in magnitude to measure accurately. This is not an unexpected result considering the large depth of the slab and the distance it spans. Dead load is the primary loading for this design.

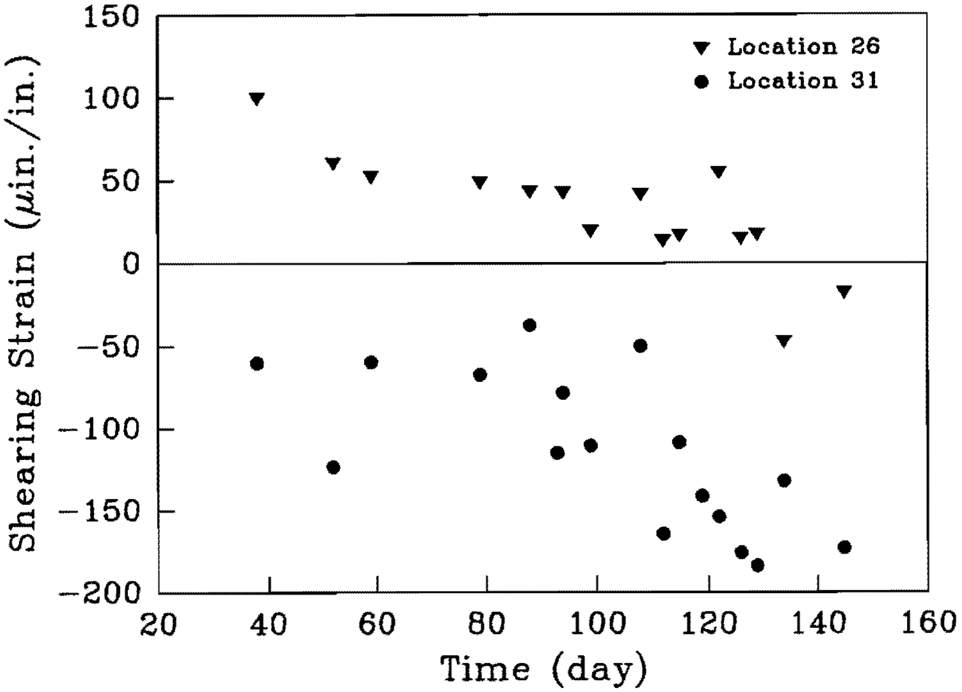

FIG. 47. Shearing Strain near Banded Prestressed Region

However, it is desirable to test the accuracy of the analysis program in predicting structural response to this type of loading. In order to accomplish this, a higher concentrated load is applied (in addition to the distributed lane load) in an attempt to achieve measurable strains. The chosen concentrated load is 2.5 times the initial load. The loads are placed equidistant from the column line in both spans at 10 ft (3 m), 8 ft (2.4 m), and 6 ft (1.8 m) (see Fig. 24). Table 11 shows the deflections of the slab along the center of the loads, measured by LVDTs located under the slab at elevation locations 20, 21, 22, 24, 25, and 26 (Fig. 8), along with predictions from FEA. These results are shown graphically in Fig. 48. Computer predictions agree with deflections measured in the model to within 10% for most locations. Further accuracy could be achieved with refinement of the finite element model. It should also be noted that the model slab did not behave symmetrically under applied loading; this increased inaccuracies in the right span.

Table 11. Comparison of Measured and Predicted Deflection for AASHTO Live Load

Distance from Jacking End (in.) (1)	Distance of Line Loads from Center Bent					
	10 ft		8 ft		6 ft	
	Model 2 (in.) (2)	FEA (in.) (3)	Model 2 (in.) (4)	FEA (in.) (5)	Model 2 (in.) (6)	FEA (in.) (7)
84	-0.066	-0.072	-0.056	-0.062	-0.050	-0.052
168	-0.088	-0.095	-0.077	-0.082	-0.066	-0.067
252	-0.054	-0.054	-0.050	-0.050	-0.045	-0.043
420	-0.050	-0.055	-0.046	-0.050	-0.038	-0.043
504	-0.087	-0.095	-0.073	-0.082	-0.058	-0.068
588	-0.068	-0.072	-0.060	-0.063	-0.048	588

Note: 1 in. = 0.0254 m; 1 ft = 0.305 m.

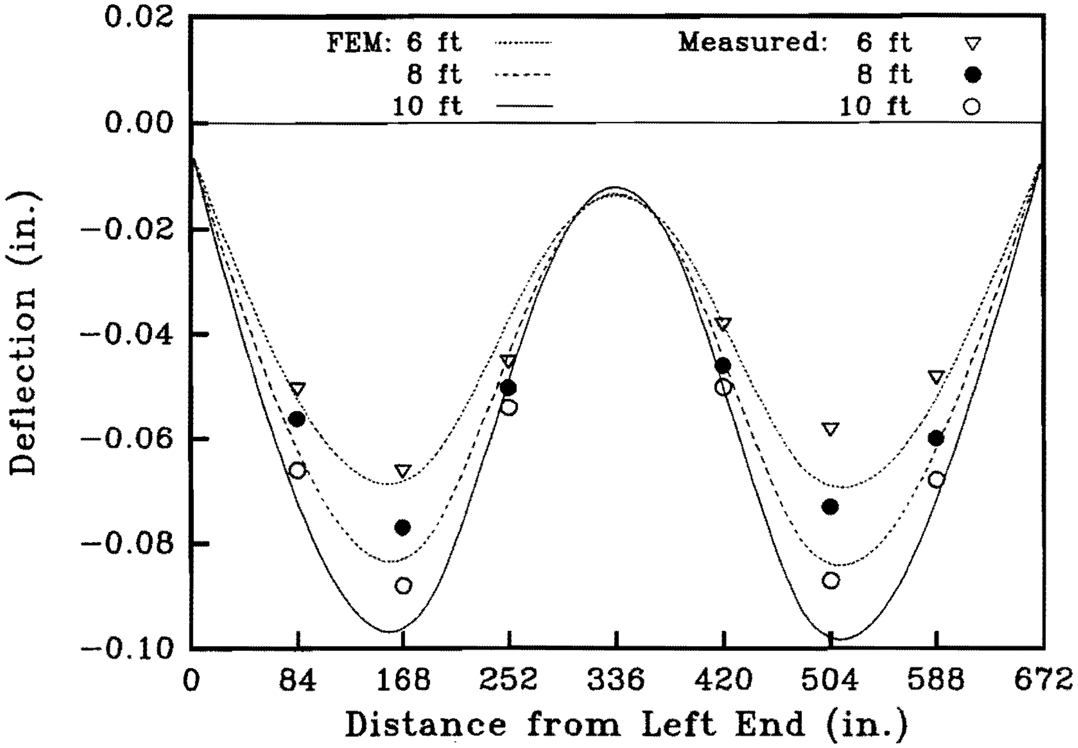

Fig. 48. Deflection Caused by AASHTO Live Load

Figs. 49 and 50 show contours plots of the measured and predicted changes in strain for the top and bottom layers of the slab. Point values indicate strain gage readings, and the predicted values are shown as contours. The figures show general agreement in strain distribution between FEA predictions and those recorded during the test. However, some discrepancies are present. Since the small magnitude of the strain changes are of the same order as errors that may occur when measuring strain with strain gages, it is not possible to determine the accuracy of the program's strain prediction algorithm using this test. Although larger loads could have been applied, they would not simulate realistic live loading on the prototype. Further evaluation is made during the ultimate testing phase of the slab to determine the accuracy of the program (see chapter 9).

8.4 Serviceability and Fatigue Considerations

The concern in this test is that the strain reversal caused by the banded prestressing might create regions in the slab that are especially susceptible to fatigue-induced cracking that would affect serviceability of the structure. In order to evaluate this problem 200,000 cycles of service load, as described in section 7.3, are applied to the model.

Fig. 51 shows the measured deflection of the slab for one cycle of load, and the theoretical deflection predicted using the mathematical model described in section 7.3. Some additional spikes occur in the experimental curve due to interaction of the dynamic response of the slab with the loads applied by the actuators. The curve could be smoothed out with a slower application of the load; however, the additional spikes represent a more severe case of stress in the continuum than a smooth curve.

Fig. 52 shows a comparison of the initial deflection curve and one recorded at 200,000 cycles. There are only small changes in the general shape and maximum deflection of the curves.

Comparisons of static deflection and change in strain are shown in Figs. 53 and 54, respectively. Strain shown is measured at gage 24BY (see Fig. 7). There is an initial change in deflection. However, differences in strain at this location are barely measurable. This suggests a shift in the slab's response to the loading, but not a weakening of the structure. Visual inspection of the slab supports this conclusion, since no cracking is noticed in either the top or bottom surface.

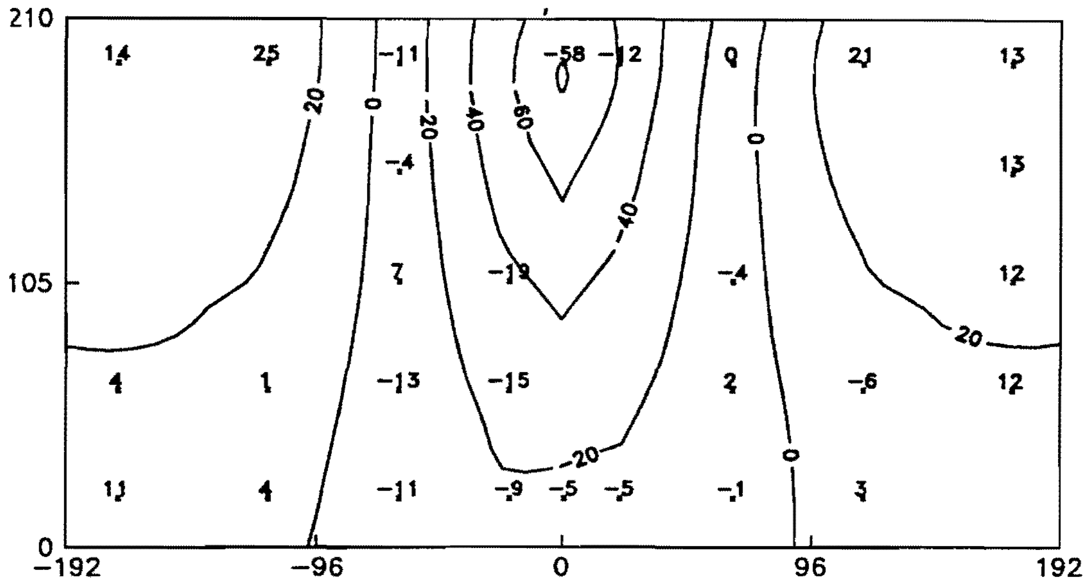

FIG. 49. Change in Longitudinal Strain Due to AASHTO Live Load at the Bottom Layer of Steel

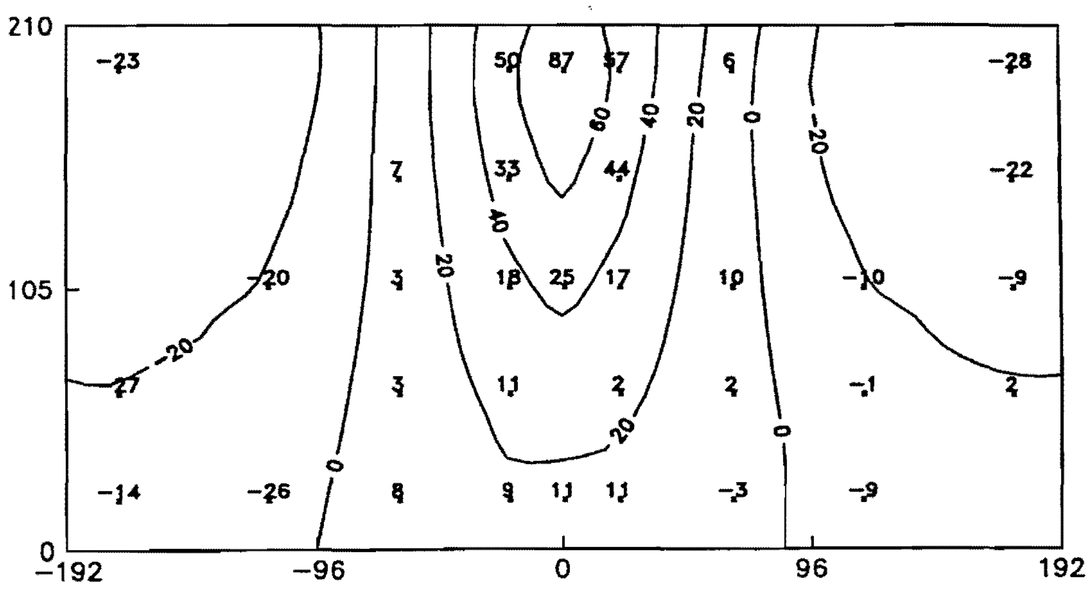

FIG. 50. Change in Longitudinal Strain Due to AASHTO Live Load at the Top Layer of Steel

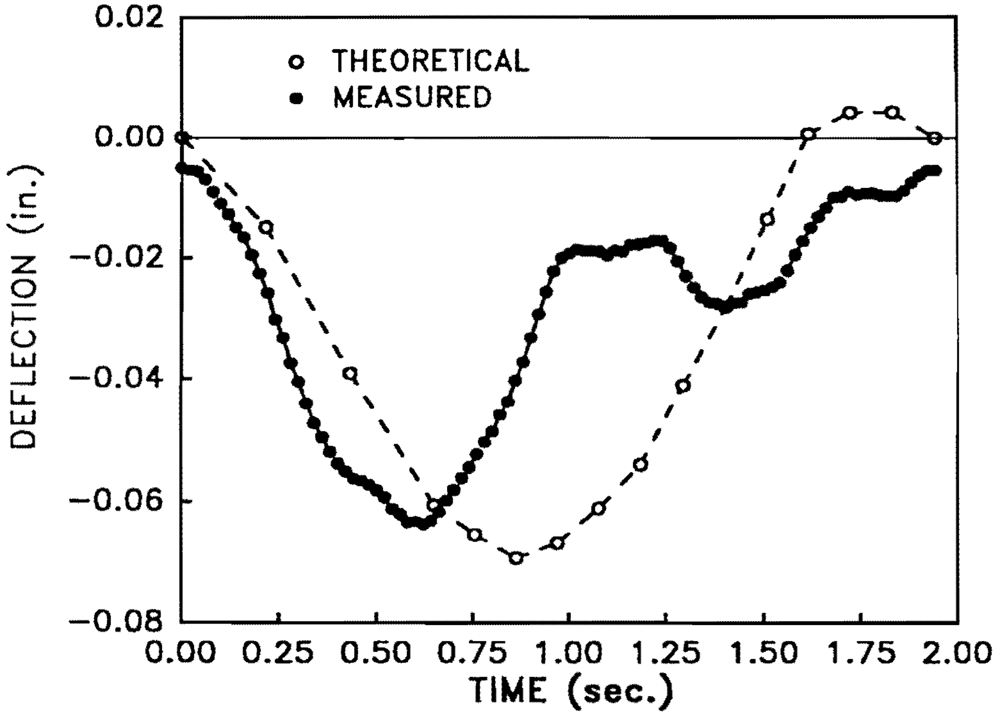

FIG. 51. Comparison of Experimental and Theoretical Deflection for One Truck Passage

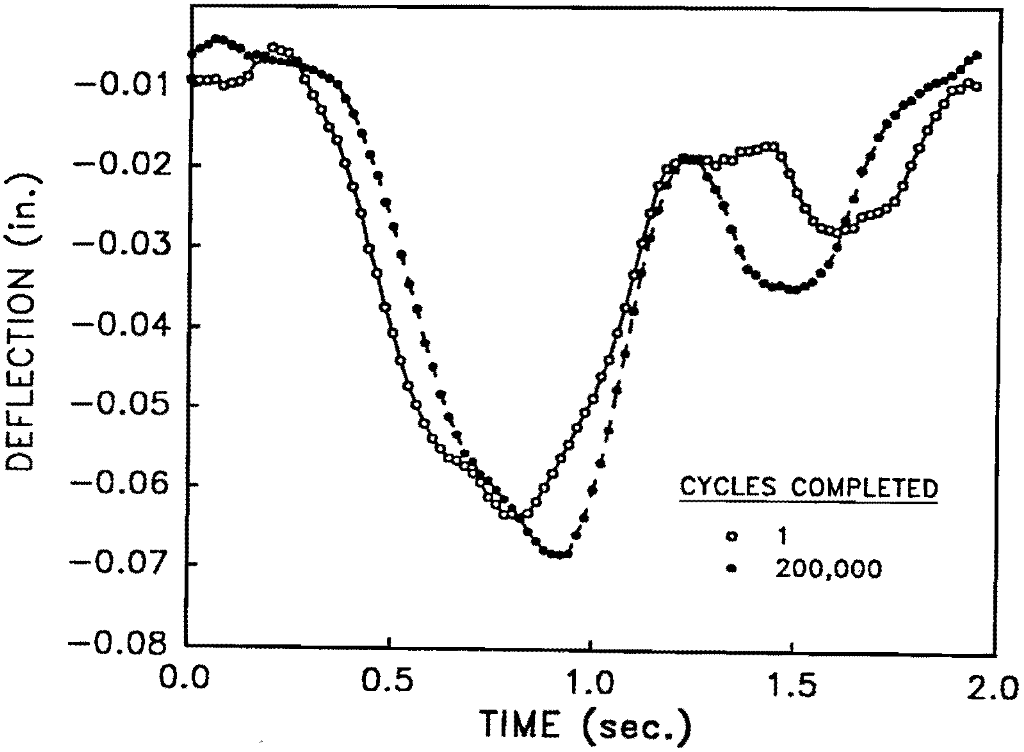

FIG. 52. Comparison of Deflection at First and Last Cycle

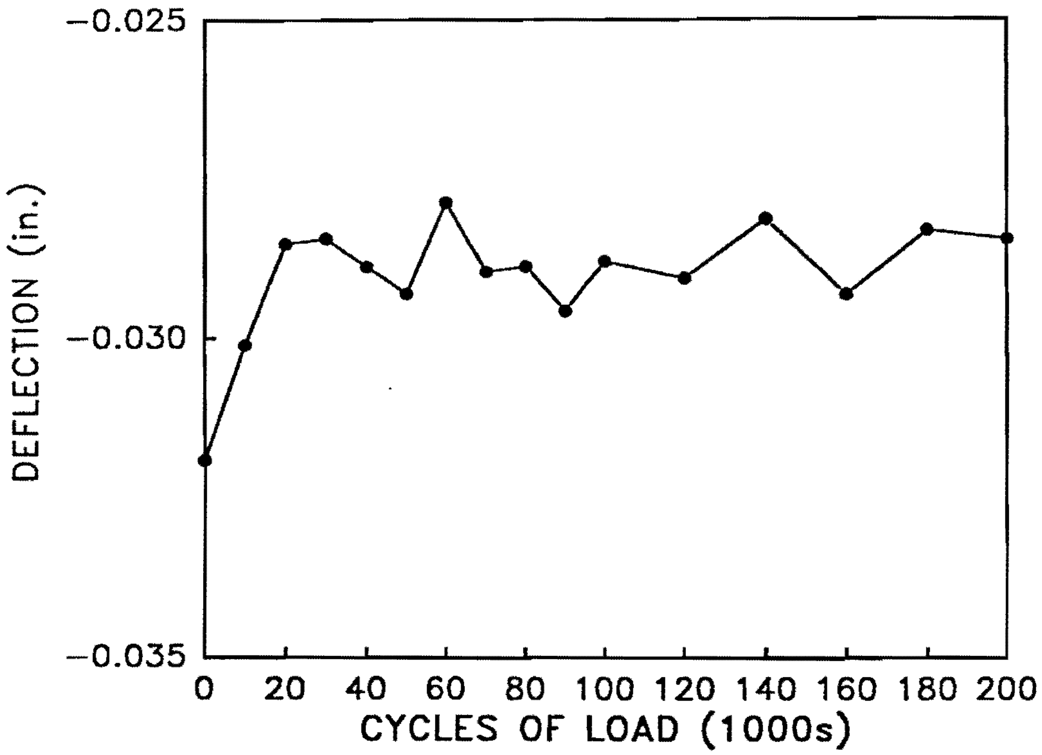

FIG. 53. Static Deflection versus Cycles of Load

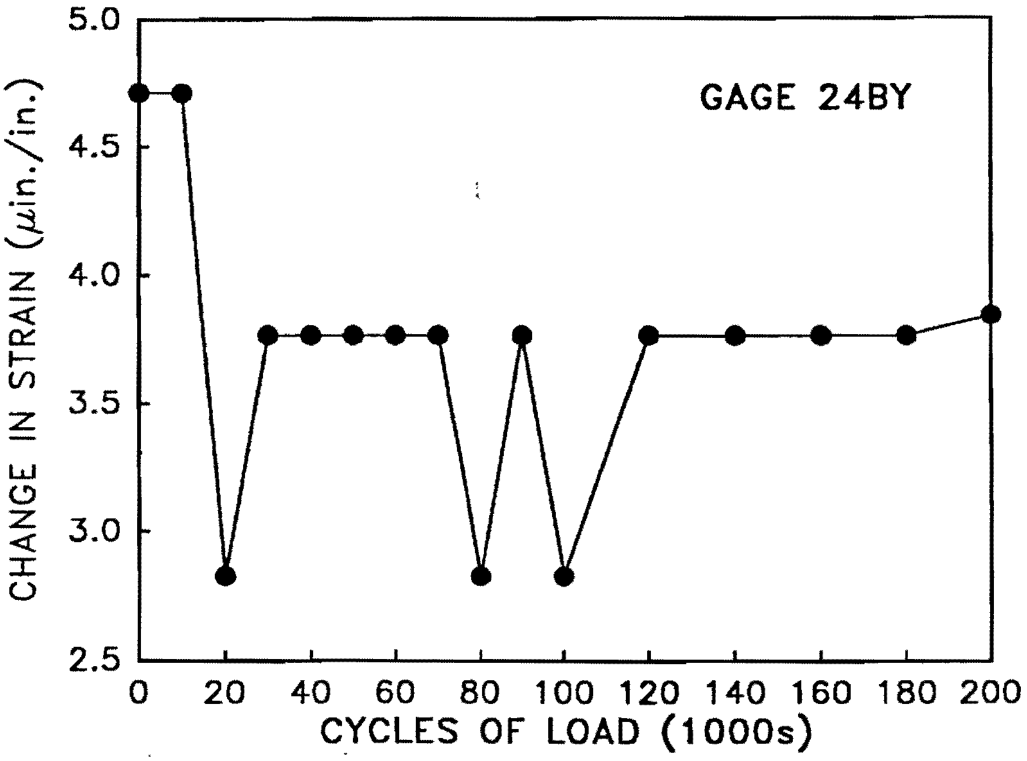

FIG. 54. Change in Strain at Gage 24BY versus Cycles of Load

8.5 Overloads

8.5.1 Introduction

Several heavy loads are applied to the slab in order to check on resistance to loads that substantially exceed design service loads. Overloads, as they are termed, occur when vehicles use a structure and cause stresses higher than those from AASHTO loading. Section 3.22.5 in AASHTO (*Standard* 1989) states that "structures may be analyzed for an overload that is selected by the operating agency." TxDOT does not have any standard criteria that define overloads, but considers heavy loads on structures as circumstances arise. This study does not attempt to dictate an overload policy; rather, motivation for this phase of the study is due to availability of a large laboratory model and testing equipment that is capable of imposing loads that considerably exceed service conditions.

Table 12 summarizes the experimental overloads placed on the slab and lists corresponding dates of importance. Due to extended length of the study, many strain gages in the model are suspect or inoperable at the time overloads are applied. However, wherever possible, results from strain gages and other transducers used during the overload tests are compared to FEM analyses in the sections that follow (see also Appendix IV).

TABLE 12. Schedule of Events for Overload Testing

Date (1)	Days after Casting (2)	Event (3)
1/31/91	477	Attempt to equalize reactions of column supports. South edge of model jacked up and shims placed under column support.
1/31/91	477	Overload test: Negative moment.
2/1/91	478	Overload test: Negative moment.
2/4/91	481	Overload test: Positive moment.
2/8/91	485	Arrange load frame for maximum positive moment test.
2/10/91	487	Overload test: Positive moment. Verify load procedure and instrumentation.

8.5.2 Numerical Modeling of Overloads

A separate FEM model is constructed to compare with experimental results from the overload test. Dimensions of the slab geometry and location of

TABLE 13. Laboratory and FEM Differential Strains for Overload

	Experimental Results						FEM Output					
	Strain (με)				Moment (k-in./in.)		Strain (με)				Moment (k-in./in.)	
Gauge (1)	XT (2)	XB (3)	YT (4)	YB (5)	MX (6)	MY (7)	XT (8)	XB (9)	YT (10)	YB (11)	MX (12)	MY (13)
1	-29	37	8	-10	3.6	-0.9	-29	33	8	-9	3.3	-0.8
2	-39	41	14	-15	4.4	-1.4	-35	39	11	-14	4.0	-1.2
3							-46	51	10	-13	5.2	-1.1
4	-53	72	-3	3	6.8	0.3	-65	72	-3	5	7.4	0.4
5	-74	95	-1	1	9.2	0.1	-75	84	3	-1	8.6	-0.2
6	-14	23			2.2		-20	20	5	-5	2.2	-0.5
7		23			1.3		-23	24	7	-7	2.5	-0.7
8	-27	27			3.2		-26	28	5	-6	2.9	-0.5
9	-25	25			3.0		-29	31	2	-2	3.2	-0.2
10	-27	32			3.5		-32	34	3	-4	3.6	-0.4
11	-5	5			0.6		-2	9	0	-1	0.7	-0.1
12	-4	5			0.5		-1	11	2	-3	0.8	-0.3
13	-3	2			0.3		1	11	3	-3	0.7	-0.3
14	0	3			0.2		2	12	2	-3	0.7	-0.3
15	1	-1			-0.1		2	12	1	-3	0.7	-0.2
16	8	-9			-1.1		14	-6	-1	2	-1.2	0.2
17	12	-9			-1.3		16	-9	1	-1	-1.6	-0.1
18	14	-15			-1.9		21	-12	0	0	-2.1	0.0
19	22	-19			-2.6		26	-17	1	-2	-2.7	-0.2
20	24	-1			-1.5		27	-15	4	-2	-2.7	-0.3
21	12	-11	-5	4	-1.5	0.5	10	-7	0	3	-1.1	0.2
22	17	-19	-2	3	-2.4	0.3	15	-14	-1	1	-1.9	0.2
23	20	-27	-8	3	-3.1	0.6	21	-20	-1	2	-2.6	0.2
24	42	-33	-3	1	-4.9	0.2	29	-28	0	0	-3.6	0.0
25	64	-49	5	-9	-7.3	-0.8	45	-39	16	-8	-5.3	-1.3
26	14	-14			-1.9		8	-12	-1	3	-1.2	0.3
27	14	-14			-1.8		12	-16	-1	2	-1.8	0.2
28	18	-23			-2.8		16	-22	-1	2	-2.4	0.1
29	31	-27			-3.8		22	-28	3	0	-3.2	-0.2
30	37	-31			-4.4		31	-33	3	3	-4.1	0.0

Note: 1 kip = 4.45 kN.

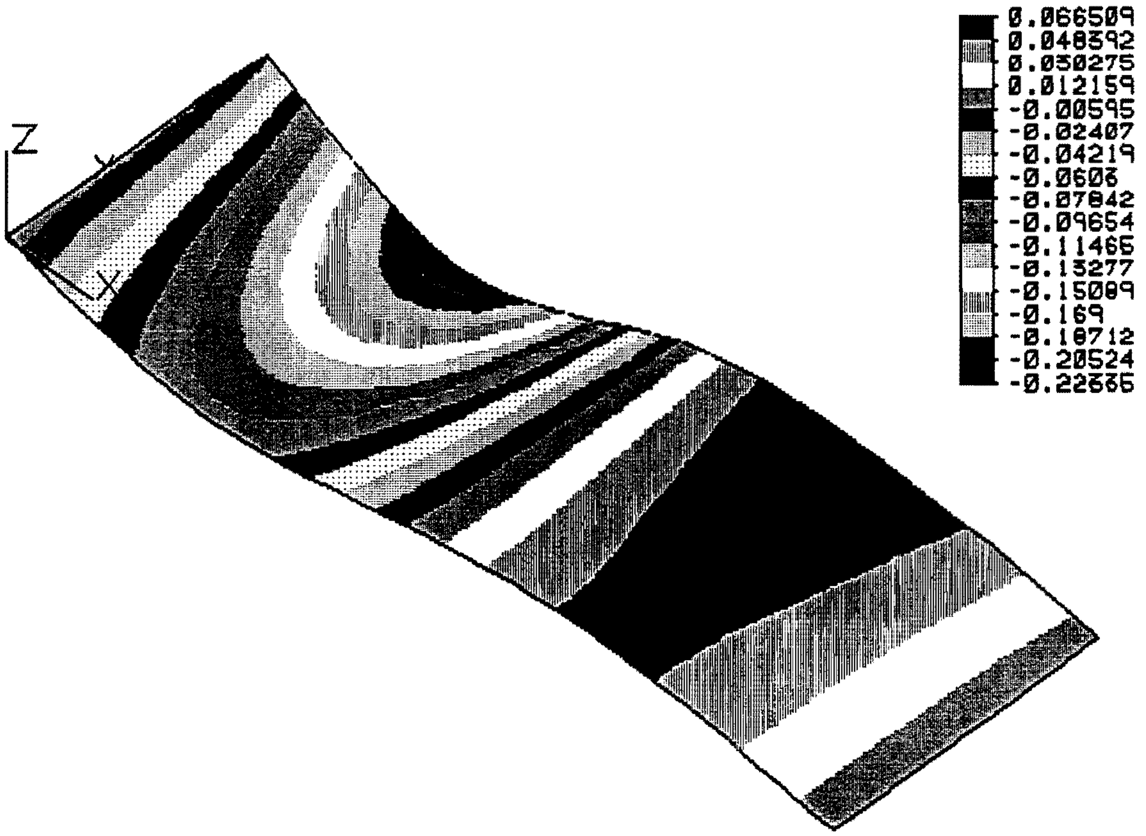

FIG. 56. Deflection Due to Overloads

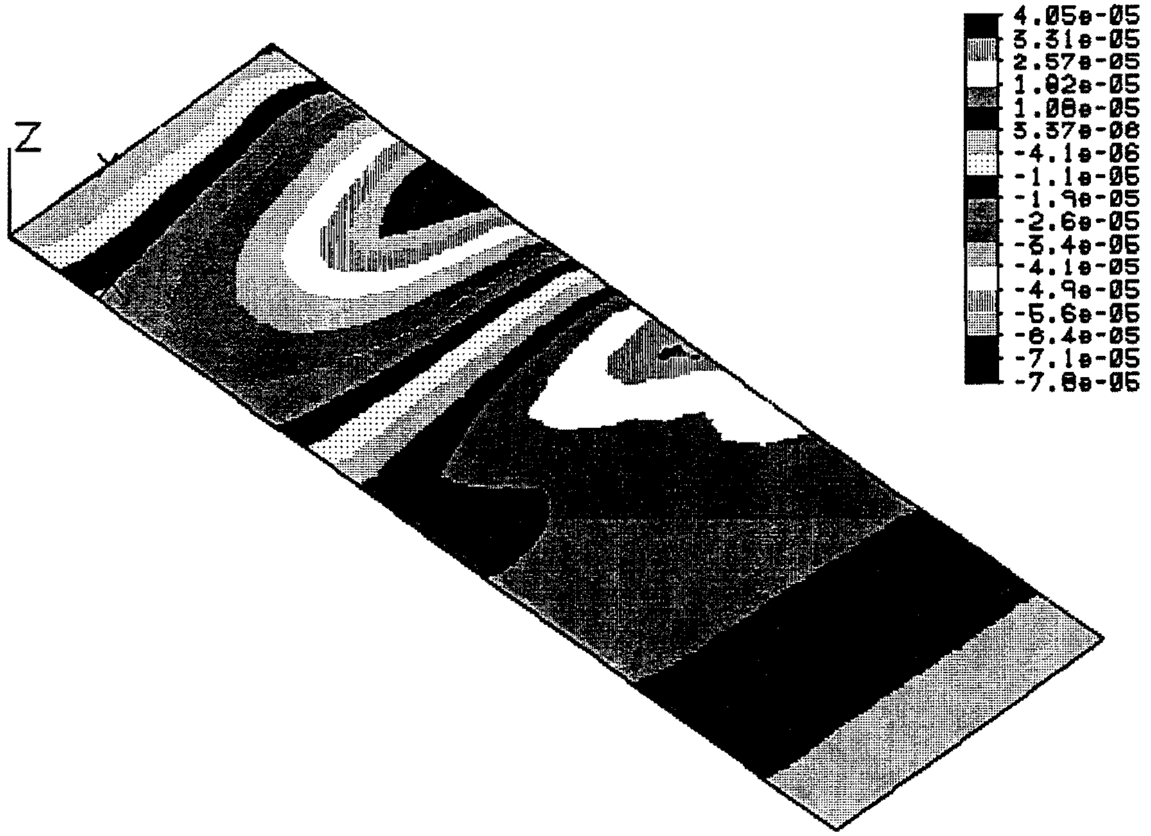

FIG. 57. Change in Strain Due to Overloads

9. ULTIMATE LOAD

9.1 Introduction

Ultimate strength of post-tensioned slab bridges is usually not a critical design consideration. Typically, checks are made on ultimate strength after an initial design has been completed that limits stresses and deflections to acceptable levels. However, because of availability in the laboratory of the large-scale Model 2 and the interest in comparing experimental values to existing ultimate strength formulas and FEM predictions, several tests are conducted with ultimate load. Sections that follow describe results of these tests and, where possible, make comparisons with numerical simulation and simplified design calculations.

9.1.1 Ultimate Testing

In order to compare experimental results with ultimate strength design values and predictions of FEM, ultimate load testing of the laboratory model is performed. This loading is performed after service loads and overload testing have taken place, neither of which caused any notable damage to the model. Sufficient time (more than one year) has elapsed so that the rate of change of long-term effects caused by creep and shrinkage are minimal.

Failure of this type of structure can occur in several modes depending on the loading configuration. Among other considerations the first phase of this project dealt with finding ultimate load capacity of the slab for punching shear (Roschke and Inoue 1990). The model studied, Model 1, was a $3/10^{\text{ths}}$ scale slab supported on a single column. Both longitudinal and transverse prestressing was used with transverse prestressing being identical to that of the model studied in this report. Experimental punch-through failure of the slab occurred at 207 kips (921 kN). Remaining failure modes to be studied for this type of slab are general shear and moment failure. Each of these modes is a subject of investigation in this final phase of the laboratory study.

9.1.1.1 Moment Capacity

Design of prestressed concrete attempts to limit stress and deflection to allowable values for the particular situation. Ultimate strength capacity is computed and used to verify the availability of reserve strength for cases of overload conditions. TxDOT uses design calculations for ultimate capacity to set minimum requirements and attest to the capacity of the finished design. AASHTO provisions are used to determine magnitude of loads used for checks on the ultimate strength. From Table 3.22.1A, (*Standard* 1989), the following expression is used to compute ultimate moment:

$$M_u = 1.3\left(M_{DL} + \frac{5}{3}M_{(LL+I)}\right) \qquad (33)$$

where M_{DL} = moment caused by dead load; and $M_{(LL+I)}$ = maximum moment caused by live load with the addition of impact. Maximum live load moment is taken to be the moment resulting from the load configuration that produces highest stress. Two specific load configurations are used to determine maximum moment: AASHTO HS20-44 truck loading and lane loading. In this study approximations of these configurations are used to create maximum moments necessary to cause failure of the model.

Ultimate moment capacity of prestressed concrete can be predicted by multiple methods. TxDOT design follows AASHTO specifications for highway bridges (*Standard* 1989), section 9.17.2, that is intended for rectangular sections. As stated, design flexural strength shall be calculated by:

$$\phi M_n = \phi\left[A^*_s f^*_{su} d\left(1 - 0.6\frac{p^* f^*_{su}}{f'_c}\right)\right] \qquad (34)$$

where ϕ = a strength reduction factor; A_S^* = area of prestressing steel; f^*_{su} = average stress in prestressing steel at ultimate load; d = distance from extreme compressive fiber to centroid of the prestressing force; p^* = ratio of prestressing steel; and f'_C = compressive strength of concrete at 28 days.

Average stress in prestressing steel at ultimate load, $f^*_{su,}$ is specified by AASHTO, section 9.17.4.1, for bonded members as:

$$f^*_{su} = f_s\left(1 - 0.5\frac{p^* f'_s}{f'_c}\right) \qquad (35)$$

where p^* and f'_C are as previously defined; and f'_S = ultimate strength of prestressing steel. A more detailed analysis to determine f^*_{su} can be performed and substituted in place of the value given by Eq. 35. A modified form of Eq. 34 is used by TxDOT:

$$\phi M_n = \phi\left[A^*_s f^*_{su}\left(d - \frac{a}{2}\right)\right] \qquad (36)$$

where a = the depth of the compression block given by:

$$a = \frac{A_s^* f_{su}^*}{0.85 f_c' b} \qquad (37)$$

where b = width of the section to be analyzed. Eqs. 34 and 36 compute almost exactly the same results with the variation between them being a reduced notation.

9.1.1.2 Shear Capacity

TxDOT follows AASHTO provisions to compute shear capacity. AASHTO states that all members subject to shear be designed so that

$$V_u \leq \phi(V_c + V_s) \qquad (38)$$

where V_u = factored shear force at the section considered, V_c = nominal shear strength provided by concrete, and V_s = nominal shear strength provided by web reinforcement (*Standard* 1989). Since plate elements in the FEM analysis program do not include terms for shear deformation, special care should be taken in regions of high shearing forces.

Although no web reinforcement is provided in the laboratory model, shearing strength of a solid slab bridge of this type is expected to be very high. Roschke and Inoue (1990) provide experimental values of punch-through shear in the column region for this type of slab. They compare predictions of AASHTO, ACI, and several other investigators and show that AASHTO's prediction of 125 kips (556 kN) is very conservative with respect to the punch-through shearing force of 207 kips (921 kN) from the laboratory model.

It is shown in what follows that shearing strength is not a critical design parameter and that the current method of design is conservatively correct. Shearing strength of concrete is the focus of this discussion. AASHTO states in section 9.20.1.1 that prestressed concrete flexural members that have the shape of a solid slab are not required to provide shear reinforcement (*Standard* 1989). AASHTO guidelines suggest that two types of shearing capacities be examined: V_{ci} and V_{cw}. The lesser of the two shall be taken as V_c. Shearing strength V_{ci} is computed by

$$V_{ci} = 0.6\sqrt{f_c'}\, b' d + V_d + \frac{V_i M_{cr}}{M_{max}} \qquad (39)$$

where b' = width of the member; d = distance from extreme compressive fiber to centroid of the prestressing force; V_d = shearing force at the section due to unfactored dead load; V_i = factored shear force due to externally applied loads; M_{max} = maximum factored moment at the section; and M_{cr} = moment causing flexural cracking at the section due to externally applied loads that is given by

$$M_{cr} = \frac{I}{Y_t}\left(6\sqrt{f_c'} + f_{pe} - f_d\right) \quad (40)$$

where I = moment of inertia about the centroid of the cross section; Y_t = distance from the centroidal axis of the gross section to the extreme fiber in tension; f_{pe} = compressive stress in concrete due to effective prestressing force at extreme fiber of section where tensile stress is caused by externally applied loads; and f_d = the stress due to the unfactored dead load at the extreme fiber of the section where tensile stress is caused by externally applied loads.

The shearing strength V_{cw} is computed by

$$V_{cw} = \left(3.5\sqrt{f_c'} + 0.3f_{pc}\right)b'd + V_p \quad (41)$$

where f_{pc} = the compressive strength of concrete at centroid of cross section resisting externally applied loads; and V_p = the vertical component of effective prestressing force. The smaller of the two strengths is to be used at the location under consideration.

9.2 Experiments and Numerical Simulation

Experimental work conducted after the service and fatigue testing took place is discussed. Method of instrumentation, loading arrangement, and numerical modeling are modified from that used in service and fatigue experiments to better accommodate the last stage of testing. A schedule of main events for this stage of testing is shown in Table 14.

9.2.1 Instrumentation

Recognition of several problems associated with the method of data acquisition used for the service and overload tests, led to a modification of the data acquisition procedure. The primary change is that the number of strain gages being read is reduced so that no switching of connectors through switchboxes is required. In addition, seven external strain gages with gage length equal to 2.0 in. (5.08 cm) are attached to the top and bottom surfaces of the slab. Gage length of 2.0 in. (5.08 cm) is adequate to provide an accurate reading since this length is more than twice the maximum aggregate size, which is 0.75 in. (1.91 cm). Selected internal strain gages attached to the reinforcing steel and the external gages attached to either the top or bottom of the slab are monitored. Locations of the internal and external gages are shown in Figs. 58(a) and 58(b), respectively. A total of 30 strain gages are read at each load increment.

TABLE 14. Schedule of Events for Ultimate Loading

Date (1)	Days after Casting (2)	Event (3)
2/12/91	489	Ultimate load test for positive moment. Cycles 1,2, and 3.
2/18/91	495	Modify load frame configuration.
2/28/91	505	Ultimate load test for positive moment. Attempts 2 and 3.
3/13/91	518	Ultimate load test for positive moment. Attempt 4.
3/22/91	527	Test for load between columns.
4/2/91	538	Ultimate negative moment load test.
4/24/91	560	Load 100 kip (445 kN) between two center columns.
5/7/91	573	Load until shear failure occurs on north edge at column.

Eighteen LVDT's are used to measure deflection at the array of locations shown in Fig. 59. Because of the concrete blocks hanging under the deck, LVDT's could not be located directly under the center of the line of load but were located 6.0-in. (15.2-cm) toward the column line. The three LVDT's on each side of the load line are moved from measuring displacement under the bridge to being supported on top of the slab by a wooden frame. This is done so that researchers could climb under the bridge to check for cracks without disturbing the LVDTs. As a check on their accuracy and also for a permanent deflection reference, three metal scales with graduations accurate to 1/16th in. (1.58 mm) are mounted on each edge of the slab for the span being loaded. One scale is mounted on each side of the slab at the load line to provide deflections where LVDT's are not present. Nylon string is stretched from the column bent to the west abutment to provide a constant level line from which deflection can be noted by the change in location of the string on the graduated scale. Additional scales are fixed to the edges of slab at the west abutment to monitor horizontal movement of the slab with respect to the abutment.

Reactions at abutments and columns are recorded by means of ten 50-kip (222.5-kN) load cells. A single load cell is provided at each column and three load cells are located along each abutment. With only three load cells at the abutments, prototype support conditions of multiple neoprene pads are not modeled precisely; however, since the primary regions of interest are not near the end spans this deemed to be acceptable. Load cells are not provided at the load points. Instead, it is assumed that the load specified by the Material Testing System (MTS) controller is applied to the bridge by the actuators.

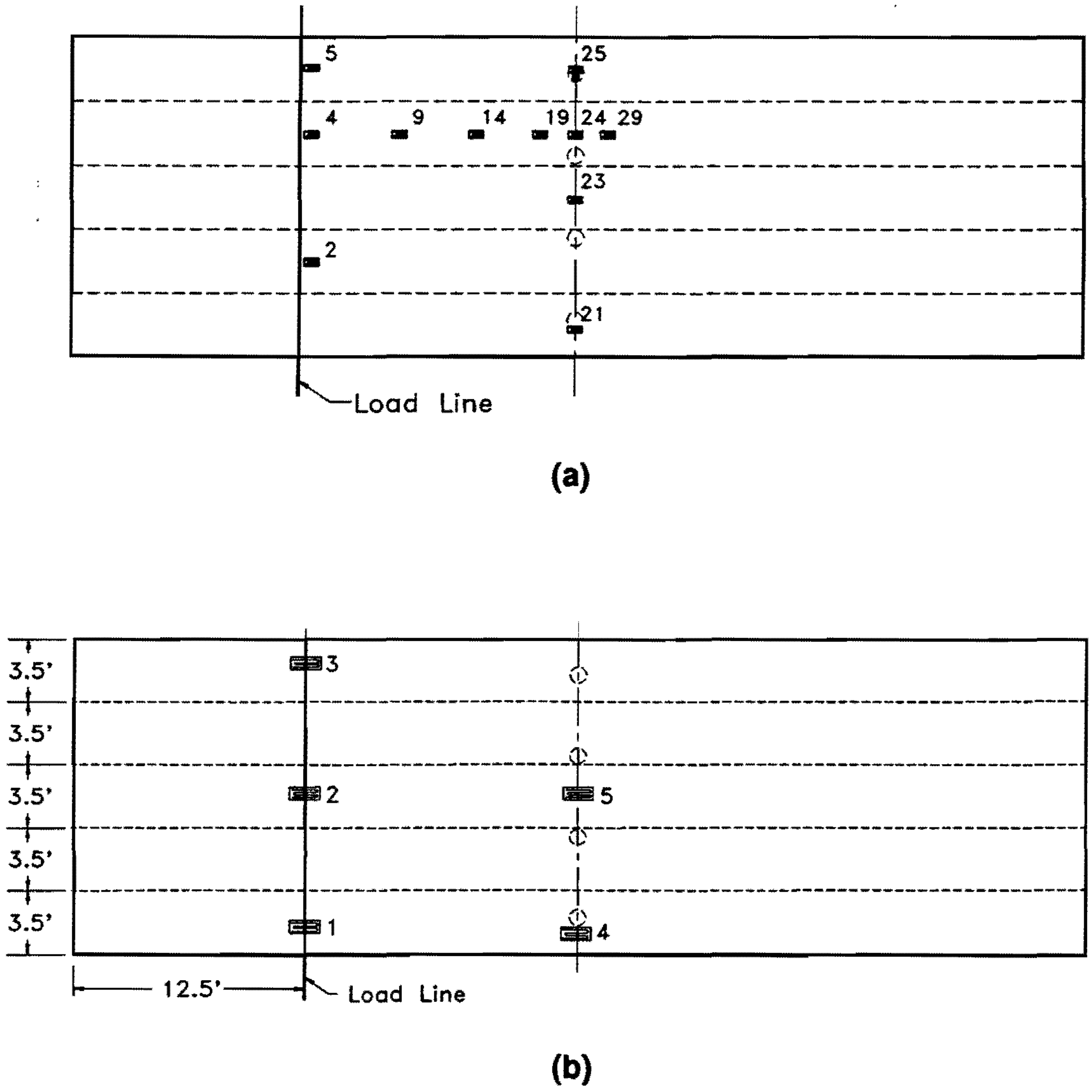

FIG. 58. Strain Gage Locations: (a) Internal; (b) External

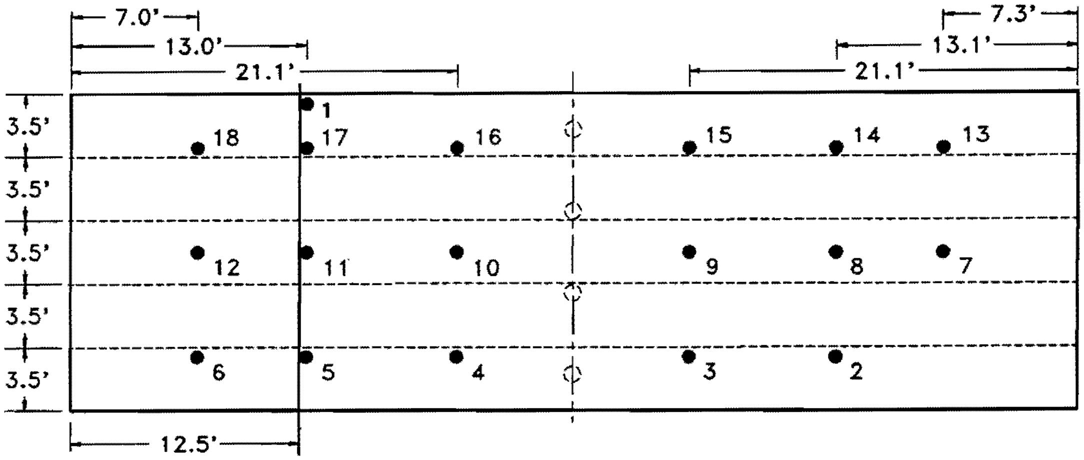

FIG. 59. Location of LVDT's

9.2.2 Experimental Setup

Load is applied to the model by means of hydraulic actuators. A plan view of the slab, position of the load line, and hole pattern in the floor of the laboratory is shown in Fig. 60. This setup consists of two 110-kip (489-kN) actuators and one 55-kip (245-kN) actuator. It is important to maintain constant load on the model during data acquisition. To achieve this, the actuators are set to the load-control mode. This means that the amount of load specified by controller is the amount of load that is applied continuously until the applied load is changed or failure results. Since applied load for each 110-kip (489-kN) actuator is divided into two individual load points, the magnitude of force for each 110-kip (489-kN) actuator is twice that of the 55-kip (245-kN) actuator that has a single load point. Control of the amount of load applied to the bridge by each actuator is done manually. The two outside actuators are loaded simultaneously to a specified load; this is followed by adjusting the center actuator to its desired load. Unsymmetrical loading is kept to a minimum by this method. In addition, variation of loading between actuators is minimized by using incremental loads to accomplish the specified total load step. Data acquisition is conducted after all load is applied for a specified load step. Finally, concrete structures are subject to creep as the stress level is varied, and they continue to deflect after the intended load is applied. Data acquisition shows that creep of the structure for this series of tests is not excessive.

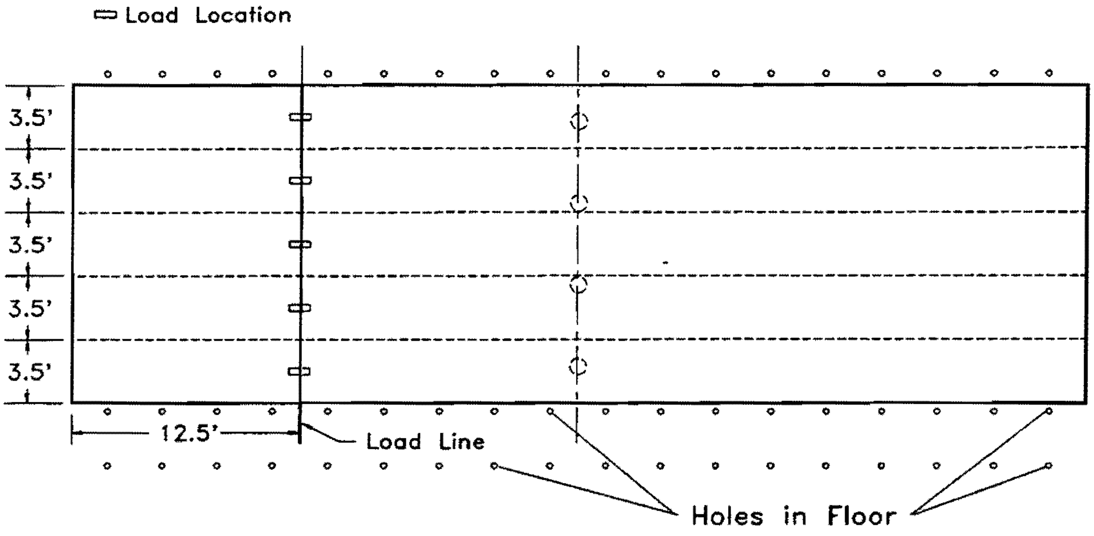

FIG. 60. Experimental Test Setup

9.2.3 Computer Simulation

Numerous computer simulations are conducted in order to compare predictions with experimentally obtained results. Several finite element models different from those discussed previously are used for this purpose. Comparison between trial models with varying degrees of discretization and loading configurations resulted in selection of a model that produces reasonable results within a reasonable amount of computer time. In particular, the model chosen to predict the ultimate response for positive moment is discussed. Computer simulations are not performed for the ultimate negative moment and shear loading. After the ultimate positive moment test, the structure is severely damaged and numerical modelling is not feasible. Also, because NOPARC is not able to predict shear failure, computer simulations are not performed for testing of ultimate shear.

The model used to simulate ultimate positive moment loading consists of a non-uniform mesh with non-uniform loading (Fig. 61). A non-uniform mesh is used to minimize analysis time as is discussed later. The discretization is made such that a fine mesh exists in areas of interest and a less fine mesh in areas of less importance. In addition, element size at the point of loading corresponds to the size of the loaded areas so that pressures may be applied to the model instead of concentrated loads. Pressures are used to represent the load applied in each lane except the center lane. Two concentrated loads on each side of the load line are applied to nodes in the center lane. Application of the additional dead load and placement of supports is the same as for the overload model.

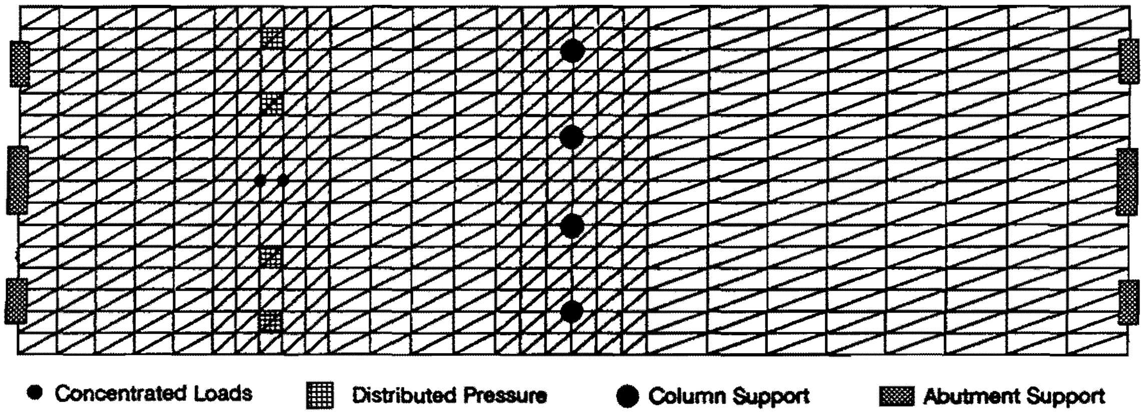

FIG. 61. FEM Mesh Used to Model Ultimate Positive Moment Behavior

Because ultimate loading causes large deflections, the nonlinear geometry option in NOPARC must be used. Initial simulations performed without using nonlinear geometry resulted in premature failure of the model. The geometric stiffness matrix is also updated during the ultimate analysis. The reader is to referred to the NOPARC reference manual (van Greunen 1979) for a further description of each of these features. In addition, because large deflections are expected, the convergence tolerances are relaxed. Tolerance for deflection and rotation are 0.05 in. (0.13 cm) and 0.10 rad., respectively, which are an order of magnitude larger than the counterpart values used in the service and overload simulations. Reducing the tolerances results in fewer iterations that are required to reach convergence; this, in turn, means reduced computer time.

Performing an ultimate analysis requires application of loads such that failure of the model results. Reaching the ultimate load involves numerous load steps. The total load is subdivided into three smaller incremental steps for analysis. Within each analysis step, several additional steps are used to reach the prescribed level of load. The first analysis step applies 70% of the ultimate load. The second step adds 24% more of the load required to reach the ultimate level. The remaining 6% is applied in the third step. An iterative process that varies the amount of load applied in the third load step is carried out in order to converge to the maximum attainable load.

9.3 Testing Results and Comparisons

9.3.1 Positive Moment Loading

Ultimate loading of the structure is performed on model's west (leftmost) span. The east span had notable areas on the bottom surface of the slab where concrete was incorrectly placed and left a minor number of reinforcing steel and tendon ducts partially exposed. A slight hump on the bottom surface of the slab due to settling form work was also noted on the east span. Other than the mentioned construction defects, both spans are identical Positioning of loads such that maximum moment could be obtained was governed by laboratory configuration. Without restriction due to spacing of holes in the laboratory floor, loads would be placed four-tenths of the length of a single span from the end support. However, floor hole spacing is fixed at a distance of 3.0 ft (0.914 m) center-to-center (see Fig. 60). As a result the position of model did not allow placement of load at the optimal location. Instead, an FEM study shows that maximum moment is obtained when the load is placed 12.5 ft (3.81 m) from the west support. This is equivalent to 0.45 times the span length.

As previously mentioned loading is applied to the bridge by means of three hydraulic actuators, two with 110-kip (489-kN) capacity and the third with 55-kip (245-kN) capacity. Fig. 62 shows the load frame and actuators used for the positive moment loading. The load frame is constructed with steel W-sections and supports the weight of the actuators. Columns supporting the beam are bolted to the laboratory floor. Load is transferred to the bridge by a series of steel spreader beams attached separately to the actuators. Five points of loading are applied to the slab from the actuators: two load points for each 110-kip (489-kN) actuator and a single point for the 55-kip (245-kN) actuator. Loads at each point are assumed to be of equal magnitude. Pieces of structural grade plywood 3.0 in. (7.6 cm) in width transfer load to the bridge deck.

Five lanes of loading are simulated by this configuration (Fig. 63). Each lane in the scale model is 3.5-ft (1.07-m) wide with the concentrated load placed at the center of the lane. AASHTO specifies a lane width in the prototype structure to be 12.0 ft (3.66 m). Applying the three-tenths scaling factor used to construct Model 2 gives 3.6 ft (1.10 m) which is close to the actual value. A total of 5 lanes on this structure is unlikely and, in this respect, is not representative of the prototype, but it provides a convenient and uniform way to apply required load effectively.

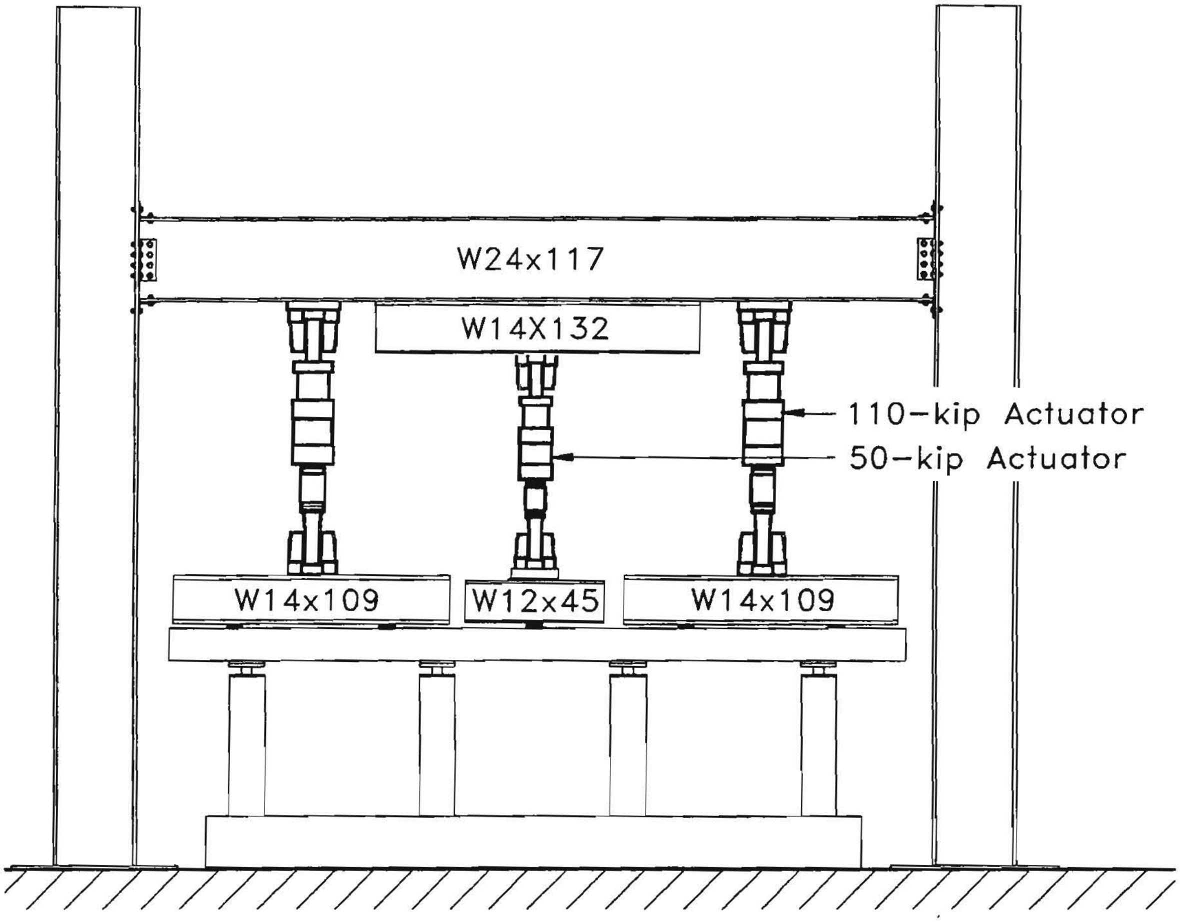

FIG. 62. Load Frame for Positive Moment Test

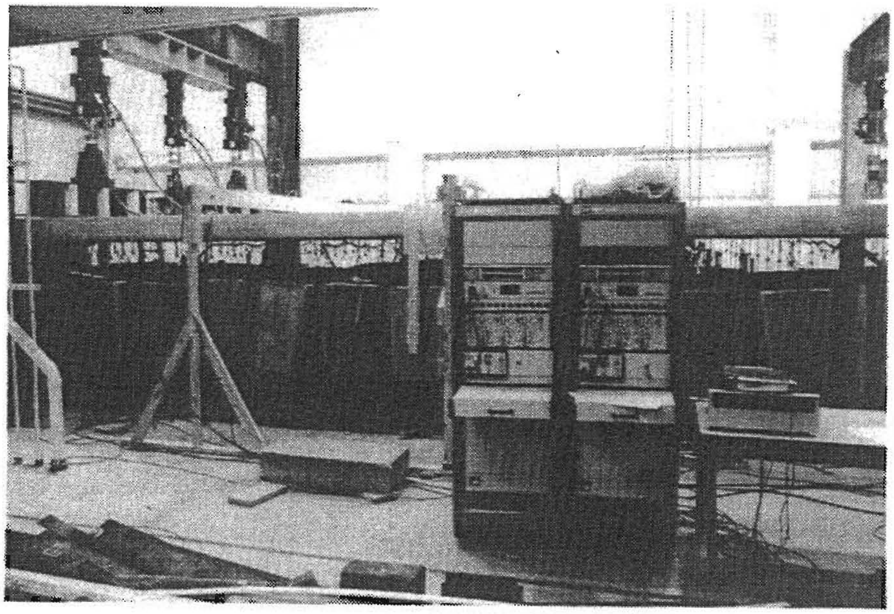

FIG. 63. Load Configuration for Positive Moment Test

9.3.1.1 Cycle One

Before causing extensive and permanent damage to the model, a load causing a moment equivalent to that resulting from Eq. 33 is applied. This stage of testing is termed cycle one. Following AASHTO provisions, the maximum moment resulting when either an HS20-44 lane loading or a truck loading is applied shall be used. To compute which loading causes maximum stress, the computer program BMCOL51 (Roschke, Epperson, and Aftab 1988) is used. Five lanes of loading and five trucks are applied to the model to produce these moments. The appropriate AASHTO load reduction factor of 75% as specified in section 3.12.2 (*Standard* 1989) is used. Positive moment due to lane and truck loading results in a maximum moment of 138 k-ft (187.2 kN-m) and 295 k-ft (400.1 kN-m), respectively. This number is arrived at by placing five AASHTO HS20-44 truck loads with a rear axle spacing of 14.0 ft (4.27 m) on the slab. Since the actual load configuration is not representative of AASHTO, the total load necessary to produce the same moment in the model is computed. The equivalent load positioned according to the experimental setup that produces a positive moment of 295 k-ft (400.1 kN-m) is 52 kips (231.4 kN). A close approximation to the 52 kips (231.4 kN), namely, 50 kips (222.5 kN) is used in the experiment to simplify control of the actuators.

Loading of the model proceeds as previously discussed. Ten equal load increments of 5 kips (22.2 kN) each are applied in order to reach a total of 50 kips (222.5 kN). Strains, deflections, and reactions from the load cells are recorded at each increment. The maximum load is reached in an uneventful fashion and then the model is unloaded. Unloading takes place in increments of 12.5 kips (55.6 kN). Checks for cracks are made but none are found.

Examination of recorded data reveals that the structure behaves linearly. Fig. 64 shows the vertical deflection of the model as recorded by the LVDT closest to the point of loading. Also shown are FEM predictions for the same loading configuration. FEM results tend to be less stiff and predict more deflection than actually occurred. However, comparison of values from the experimental and numerical simulation shows good agreement. The modulus of the concrete may be modeled incorrectly and may contribute to this discrepancy.

Strain gage readings taken from external concrete strain gages that are located at the load line are shown in Fig. 65 and compared with FEM simulation. Both top and bottom strains taken from the externally attached strain gages at location two (see Fig. 58) are shown. Careful inspection shows that the strains are of equal magnitude on each face of the slab. Tensile strains on the bottom appear to begin to deviate slightly from a linear relationship after approximately 40 kips (178 kN). Concrete at the bottom of the slab goes into tension near this level of load. The stress at a load of 50 kips (222.5 kN) is computed to be 300 psi (2.068 MPa).

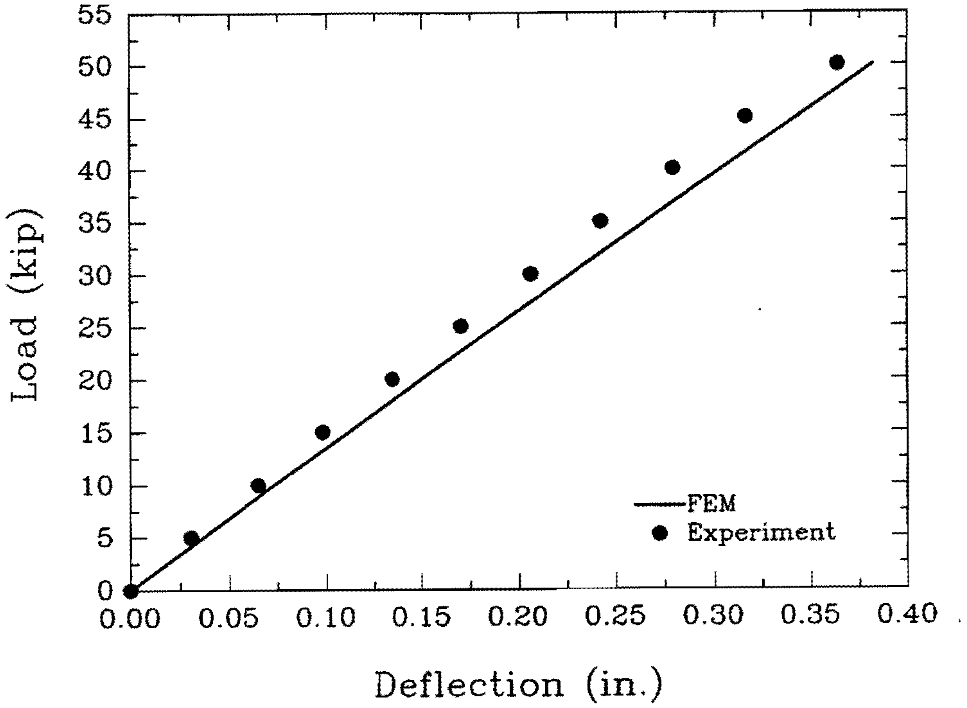

FIG. 64. Vertical Deflection for Cycle One

Further examination of the collected data is made. Fig. 66 shows the deflected shape of the model with 50 kips (222.5 kN) of applied force. This is the deflected shape resulting from the live loading only. Again, FEM results that are plotted along longitudinal lines of LVDTs tend to be slightly higher than the experimental readings; a maximum error of 20% occurs in the east (unloaded) span. It is also noteworthy that deflections are nearly uniform across the width of the slab. This indicates that the loading is equal at each of the load points. Readings along the longitudinal centerline are slightly smaller than readings along the edge, which is expected because the plate stiffness is larger in the center region.

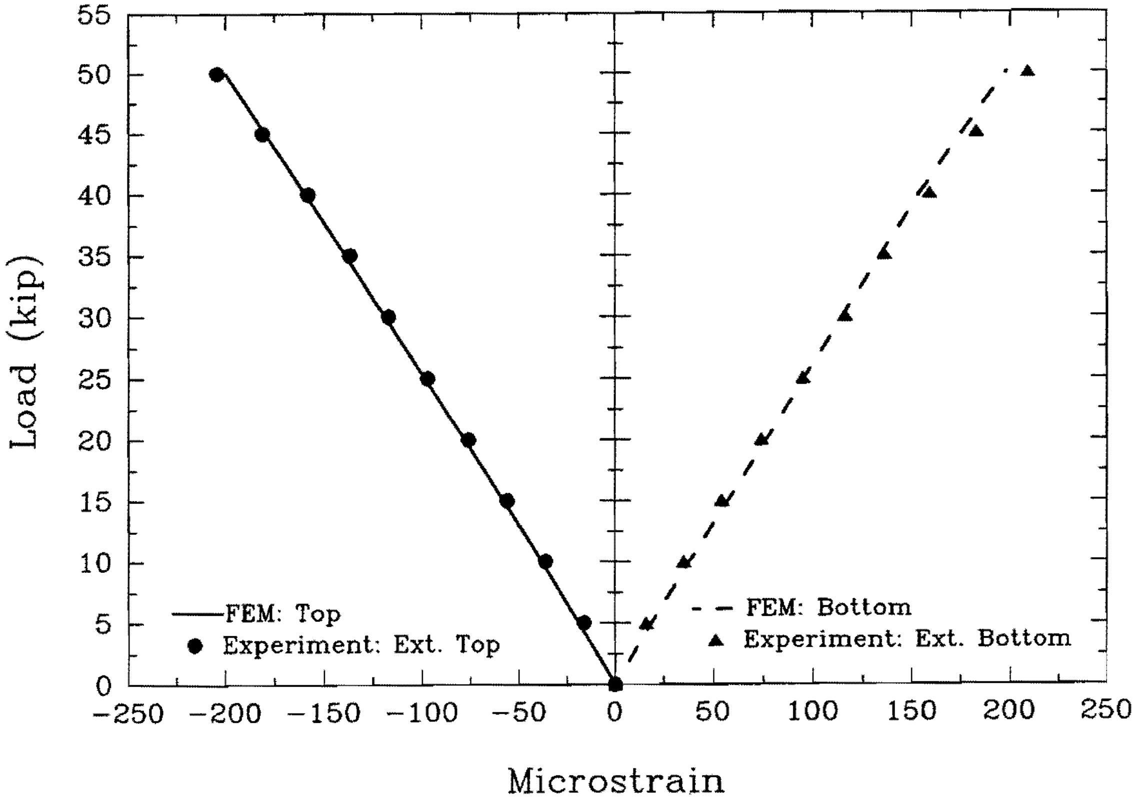

FIG. 65. Concrete Longitudinal Strains at Load Line for Cycle One

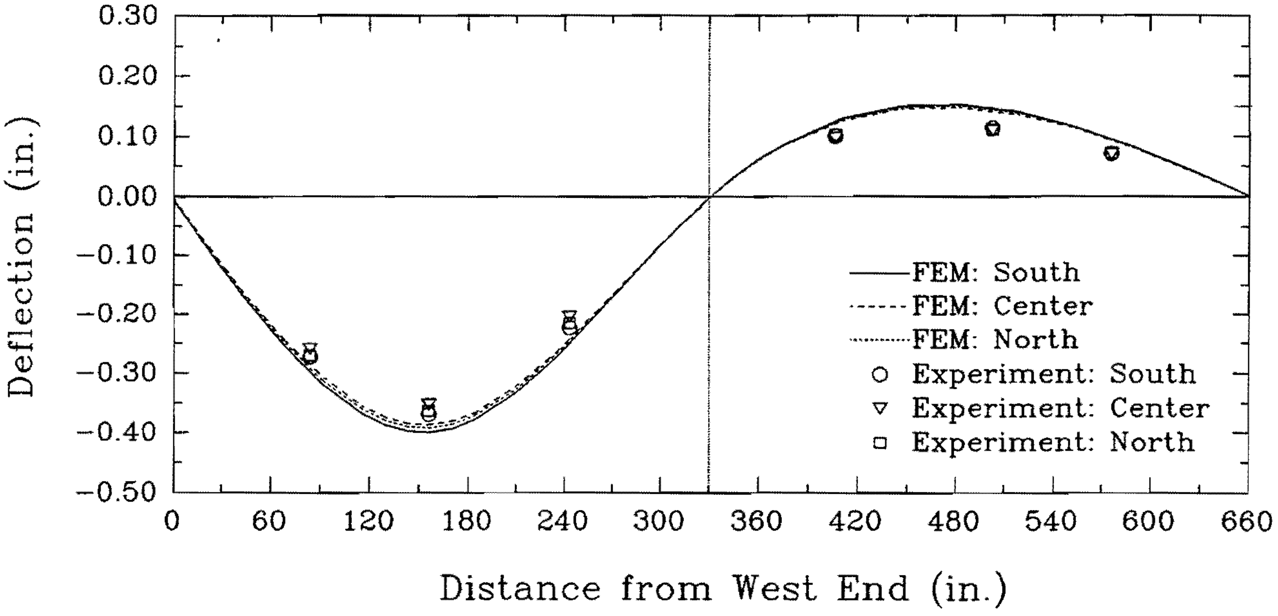

FIG. 66. Deflected Shape at 50 Kips

A comparison of strains along longitudinal lines is made in Fig. 67. Both top and bottom strains in the longitudinal direction are shown. Experimental values are taken from strain gages mounted on the longitudinal reinforcing bars (Fig. 58(a)). It can be discerned that strains on the bottom and top lines of elements are not totally symmetric. The skewed triangular mesh contributes to this phenomenon. In addition, because of construction problems the steel layers are not perfectly equidistant from the centroid of the cross section and, therefore, a small discrepancy arises in the strain gage readings.

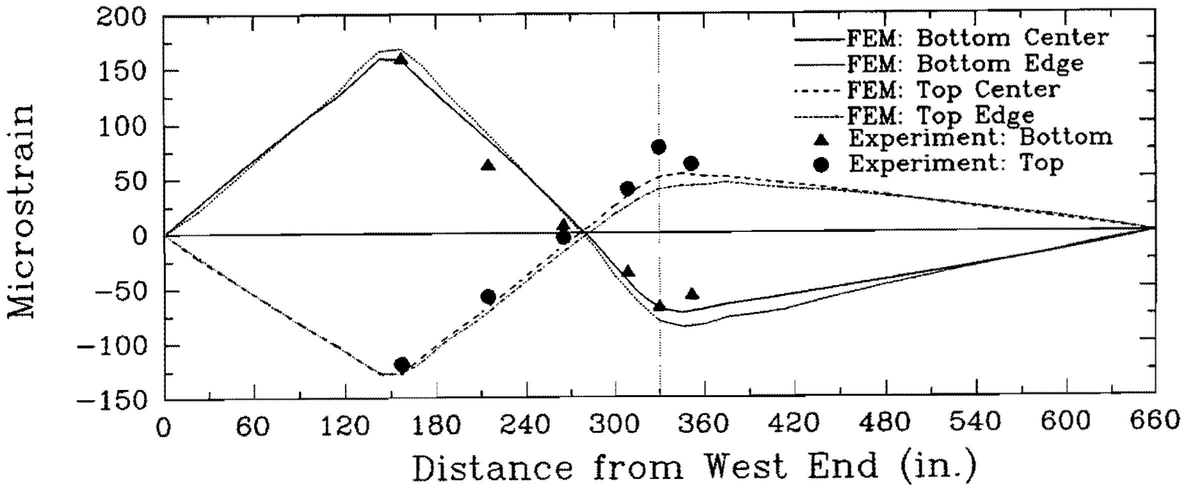

FIG. 67. Change in Strain at 50 Kips

Moment is computed from the normal strains in Fig. 67 and is shown in Fig. 68. Experimental values tend to agree well with numerically simulated counterparts except at the column bent. Maximum moments computed experimentally and numerically are 266 kip-ft (360.7 kN-m) and 277 kip-ft (375.6 kN-m), respectively. This is nearly as large as the computed ultimate positive moment of 295 kip-ft (400.0 kN-m); however, the structure appears to be unharmed. Readings are taken after all of the load is removed; all internal strain gages returned to very near their initial readings. All external strain gages did likewise except for the top gage at location 4 (see Fig. 58). The exception showed a residual of 34 microstrains. Vertical deflections from LVDTs returned to within 0.01 in. (00.254 mm) of the initial readings.

9.3.1.2 Cycle Two

After test cycle one, the model is loaded again until visible cracks appear. A close inspection of the fissures is made and the load is again removed. This stage of the testing is termed cycle two. The purpose of this test is to cause visible damage in the slab and then to release the load to see what residual effects remain. Loading takes place in four increments of 12.5 kips (55.6 kN), two increments of 10 kips (44.5 kN), and nine increments of 5 kips (22.2 kN) to reach a total of 115 kips (511.8 kN). Fig. 69 shows a plot of load versus maximum vertical deflection for cycle two. An error in data collection at 75 kips (333.8 kN) and 80 kips (356 kN) accounts for the absence of data points at those loads. Numerical simulation is also performed for cycle two and results are shown in the same figure. Fig. 70 shows the variation of strain with the increase in load for gages 2, 4, and 5 as well as their FEM counterparts.

The experimental data show that the vertical deflection becomes nonlinear after approximately 60 kips (267 kN). The simulation predicts more deflection at all levels of load until 115 kips (511 kN) is reached. At this load the FEM prediction intersects the actual data points from the experiment. This means that the numerical model initially uses a lower stiffness than is actually the case. Some degree of tension stiffening related to the formation of cracks in the physical slab may contribute to this discrepancy. Tension stiffening is discussed in section 2.4.

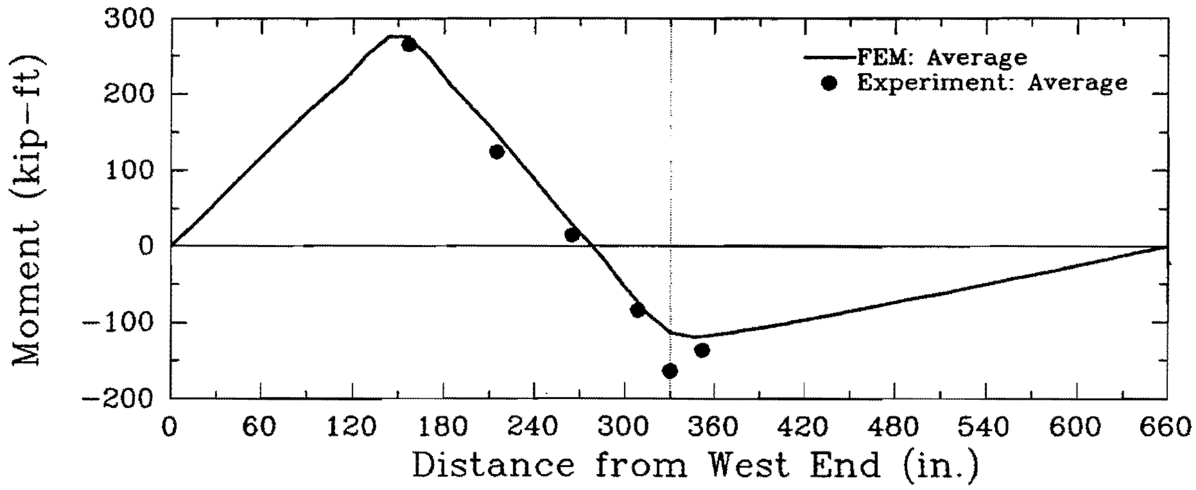

FIG. 68. Resultant Moment at 50 Kips

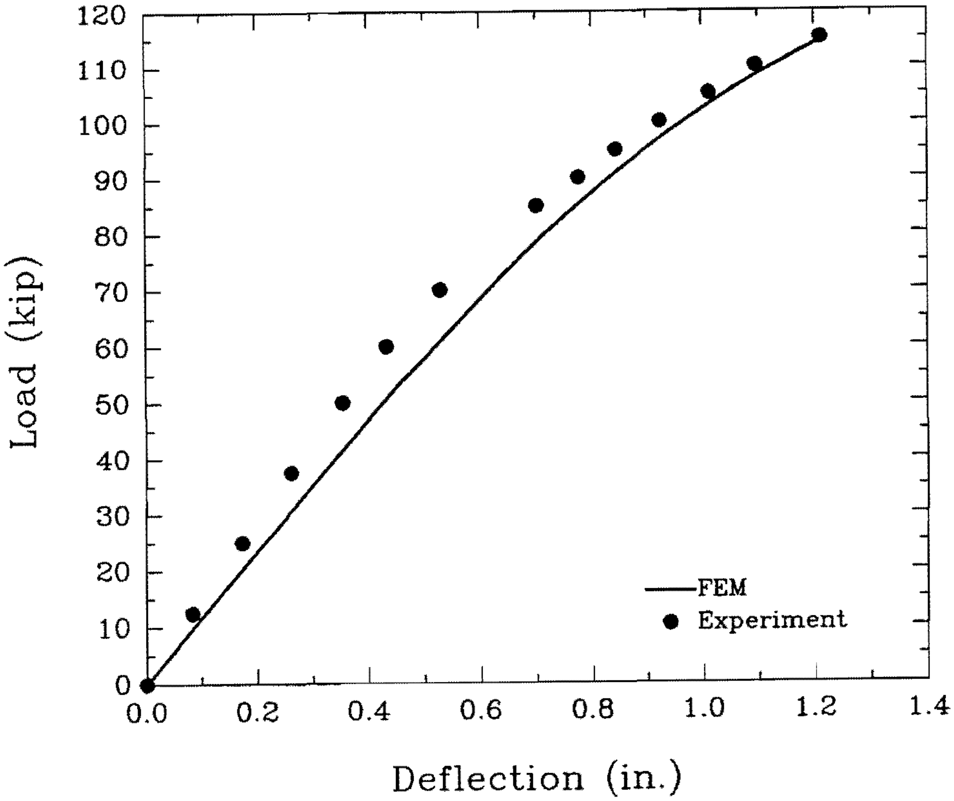

FIG. 69. Maximum Deflection History for Cycle Two

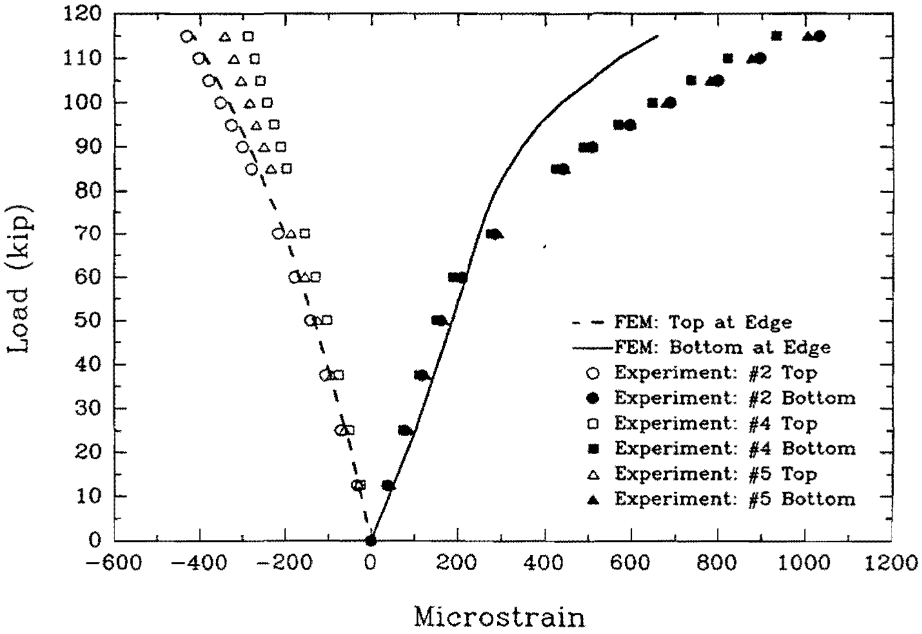

FIG. 70. Strain History During Cycle Two Loading

Cracking is not detected visually until a load of 95 kips (423 kN) is applied. The first crack observed appears on the top surface over the columns. External strain gages indicate that cracking occurred earlier than this load level. Strain at the bottom gage at location 1 (Fig. 58(b)) began to decrease after a load of 50 kips (222.5 kN) is applied. Delamination of the strain gage and the concrete resulted, probably because of minute cracks at that location. Likewise, at 50 kips (222.5 kN) the bottom external gage at location 2 shows an abrupt increase in strain. External strain gages at locations 2 and 4 that were in tension became inoperable at 70 kips (333.5 kN) and 60 kips (267 kN), respectively. Even though cracking is observed, loading continues up to 115 kips (511.8 kN). Cracks continued to appear at the column bent. They were confined to a region within 3.0 in. (7.6 cm) on either side of the column bent. Cracks are first observed on the bottom of the slab at the load line at 110 kips (489.5 kN). Numerical simulation predicts the concrete to crack first under the load at 60 kips (267 kN) to 65 kips (289 kN). After 115 kips (511.8 kN) is applied, there is approximately a 4 minute period of instability, during which time cracks are observed to grow. Equilibrium is obtained, readings of transducers and other data recording devices are taken, and the load is removed. The maximum deflection reached is 1.2 in. (3.05 cm). A maximum residual deflection of 0.09 in. (0.23 cm) is observed. Average residual strains at the load line and the column bent are ±30 and +40 microstrains, respectively. Bottom external strain gages at locations 1 and 2 and the top strain gages at locations 4 and five are no longer functional.

9.3.1.3 Cycle Three

Cycle three is the last phase of positive moment testing. The goal is to apply additional load on the model until a moment-induced failure results. Load is applied in three increments of 20 kips (89 kN), three increments of 15 kips (66.8 kN), and the remaining increment in 5 kips (22.3 kN) until failure results. Fig. 71 shows the load deflection curve resulting from cycle three and results from the analytical prediction. As can be observed, failure did not occur. The test is stopped at 200 kips (890 kN) because of concern about deformation of the steel base plates of the columns supporting the load frame. This stoppage necessitated yet another test. However, following the third load cycle additional permanent deformation of the model is observed.

Even though no catastrophic failure occurs in this cycle several items merit discussion. Shallow surface cracks continue to appear and grow transversely across the slab. The cracks are marked at each load increment. All cracks are recorded at completion of the test. Some slight tensile popping of concrete is observed at 135 kips (600.7 kN). Noticeable crack widening is observed along the load line at 175 kips (778.8 kN). A prominent crack appears at the south edge under the load at 180 kips (801 kN). This crack is not as noticeable at the north edge. The crack on the north edge is more noticeable at 185 kips (823 kN) and it extends further toward the center of the slab. At 195 kips (867.8 kN), the model creeps for several minutes after the load is applied. At 200 kips (890 kN), the model continues to creep until the actuators run out of stroke. The test is stopped at 200 kips (890 kN) because of problems with the load frame.

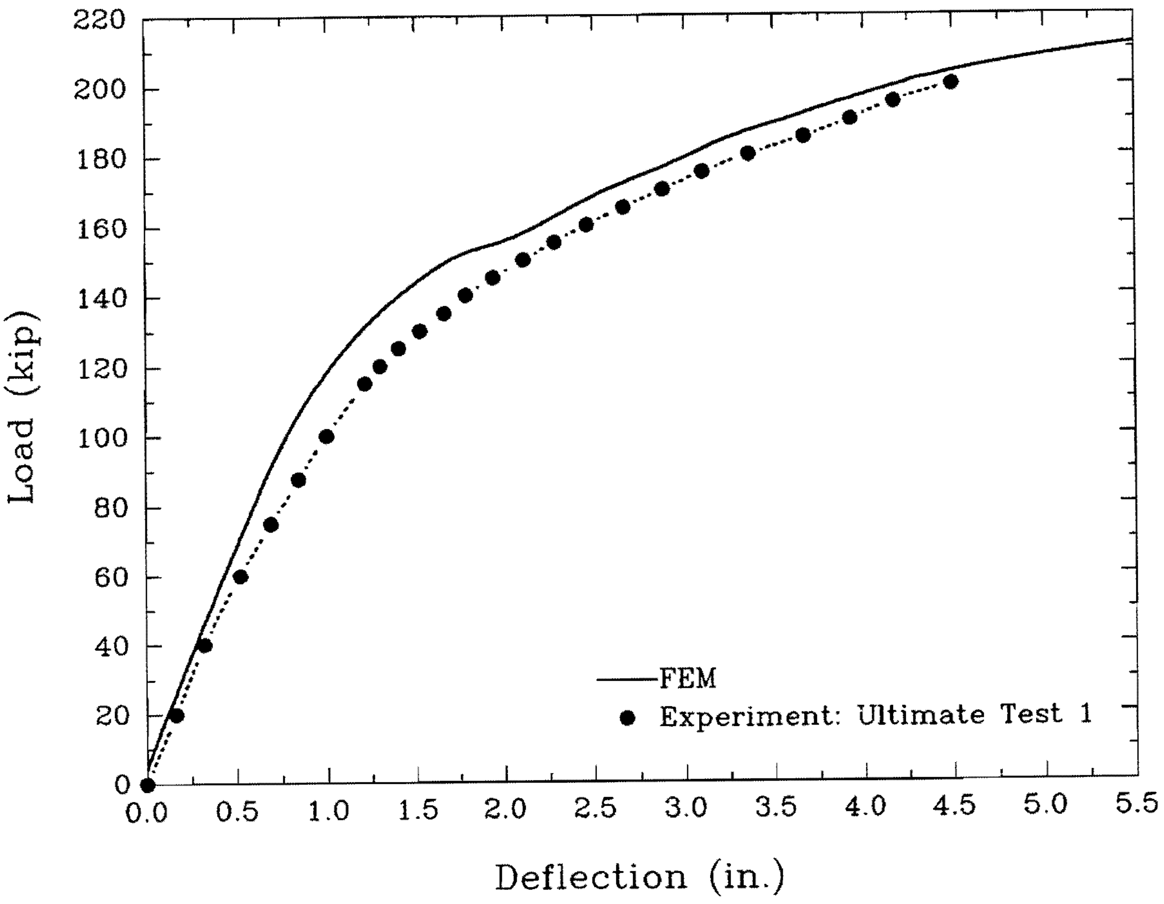

FIG. 71. Load Deflection History for Cycle Three

Some interesting observations are made from examining the data that was collected. External strain gage 2 shows that there are 3,300 microstrains of compression at the top surface of the slab due to the added load only. Adding the 150 microstrains of compression that existed prior to loading shows a total of 3,450 microstrain. This total is greater than is considered to be the ultimate strain for 8,000 psi (55.1 MPa) concrete. Another interesting phenomena is that there is a decrease in compressive strain in the top longitudinal gages at 175 kips (778.8 kN). That is, readings from strain gage start to tend toward tension in an obviously compressive strain location. Also, a maximum deflection of 4.75 in. (12.1 cm) is obtained at 200 kips (890 kN). Immediately after unloading, the maximum residual deflection is 0.63 in. (1.60 cm). Very large residual strains (approximately 6,000 microstrain) remain in the bottom longitudinal reinforcing steel in the region near the line of load. Two days later a residual deflection of 0.5 in. (1.27 cm) remains. Finally, it is noted that cracks that are visible with the load applied are not visible in the unloaded condition.

9.3.1.4 Other Ultimate Positive Moment Tests

After a small modification to the load frame, another attempt at ultimate moment failure is made. No longer are small pieces of plywood used to transfer the load to the deck. Large pieces of plywood are cut and used as shims so that adequate stroke capacity of the actuators is available and deflection may be obtained that causes failure. Pieces of plywood are cut to match the size of the spreader beams.

The attempt to fail the model a second time is termed ultimate test two. The model is loaded to 80 kips (356 kN) in four 20-kip (89-kN) increments. Data is collected at each increment. At 80 kips (356 kN), shims are placed under each spreader beam while the other actuators hold down the model such that maximum shimming is possible. After shimming, load is brought back to 80 kips (356 kN) and data is collected. Loading continues in 20-kip (89-kN) increments up to 140 kips (623 kN). Four additional 10-kip (44.5-kN) increments bring the total load to 180 kips (801 kN). Load is now applied in 2.5-kip (11.1-kN) increments until failure occurs. At 207.5 kips (923.3 kN) two thunderous sounds are heard and load in one of the actuators is suddenly released. A tendon is thought to have broke or some other internal failure occurred but there is no visible damage. The load is removed, but because of the extra shims, the actuators still compress the bridge. Load is applied to one of the actuators so that the shims may be taken away from under the other actuators. After all the load is removed an additional 0.4 in. (1.02 cm) of deflection remains as a result of this test. Later, from a video tape that filmed the event, it is observed that the dead weights hanging beneath the model shook when the noise is heard. It is believed that because of the large deflection of the bridge (approximately 5 in. (12.7 cm)), the concrete blocks rubbed against one another until, at that particular time, the force of friction was overcome, which released one block and caused an impact load to be applied to the structure; in turn, the other weights that were rubbing together were released. The impact caused one of the actuators to be interrupted; this cut off the oil pressure and relieved all force that the actuator applied.

Again, several points of interest concerning this test are discussed. At a load of 80 kips (356 kN), the model continues to creep. Maximum crack width is about 0.01 in. (0.25 mm). Loading continues up to 120 kips (534 kN) at which time the testing is stopped for 30 minutes to adjust LVDT's, allow for more deflection readings, and mark cracks under the slab. Following this pause, testing resumes and loading continues. Continued creep of the structure is noted at all remaining load increments. Deflection readings are taken several times at each load increment with careful note being made of the creep. At each load step, data collection is delayed until additional creep becomes minimal. Creep deflection at LVDT 17 is noted to be approximately 0.02 in. (0.5 mm) to 0.05 in. (1.27 mm) at each load increment. Maximum crack width is 1/16th in. (1.59 mm) at a load level of 195 kips (867.8 kN). At 205 kips (912.2 kN), the structure creeps for 6 minutes and accumulates an additional 0.07 in. (1.8 mm) of deflection. At 207.5 kips (923.4 kN), the model creeps for about five minutes before the load is interrupted. Creep deflection is noted to be 0.09 in. (2.29 mm). Maximum deflection is recorded to be an additional 5 in. (12.7 cm) with a total deflection of 5.4 in. (13.7 cm). Residual deflection resulting from this test is 0.4 in. (1.02 cm). Maximum total residual deflection is 0.7 in. (1.78 cm).

After it was decided that total failure did not occur, a third attempt is made. This attempt is termed ultimate test 3. Three 50-kip (222.5-kN) load increments are used to return the load to 150 kips (667.5 kN). Then a 25-kip (111.3-kN) increment brings the total load to 175 kips (778.8 kN). Small load increments are now made the rest of the way to failure. A load of 210 kips (934 kN) is applied without any failure. At 210 kips (935 kN) the actuators run out of stroke. With creep continuing, applied load begins to decrease and stabilize at 208 kips (925.6 kN).

The maximum additional deflection due to this load attempt is 5.3 in. (13.5 cm). Total deflection for the entire test including the residual deflection is 6 in. (15.2 cm). The residual deflection for this test is 0.15 in. (0.38 cm).

A fourth attempt at reaching the ultimate load is made (Ultimate Test 4). Positive moment failure occurs when the applied load reaches 212.5 kips (945 kN). A sudden failure resulting in crushing of concrete at the top of the slab is observed. No evidence of any breakage of prestressing tendons exists. Once the slab failed, the actuators pushed down until their stroke was expended. The maximum deflection for this test before the collapse occurred is 6.1 in. (15.5 cm). Thus, combining the residual deflections from the previous test, the total deflection is more than 7 in. (17.8 cm). The compressive strain in the top surface at the load line for this test is recorded to be 3,370 microstrains. Adding to this number the residual strains that existed prior to this test, a total of 5,000 microstrains of compression is obtained before failure results. Fig. 72 shows the load versus vertical deflection curves at the load line for all four ultimate tests. An FEM simulation is also provided for comparison. It should be noted that the computer simulation uses an initially undamaged model to predict the response. The experimental results are obtained after much testing is performed and severe damage incurred. The simulation predicts the model to have a capacity of 220 kips (979 kN).

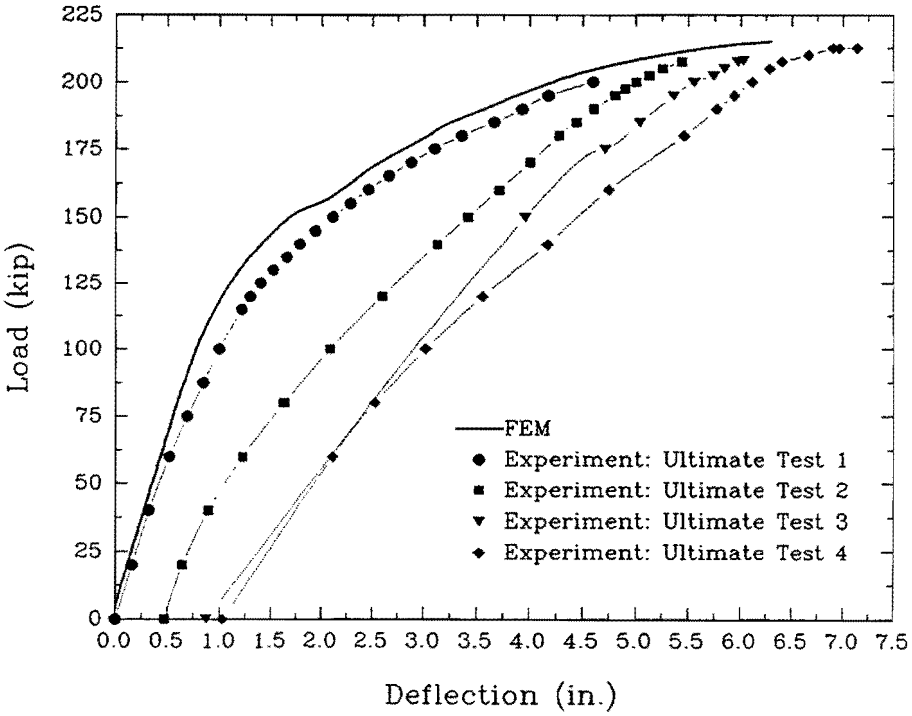

FIG. 72. History of Maximum Deflection for the Ultimate Tests

Physical damage to the model is generally confined to the west span at the load line. However, cracks are observed on much of the model. Fig. 73 shows the cracks that are marked on the bottom surface under the load. Note that crack lines stop before completely crossing the width of the bridge. Because marking the cracks requires load to be applied, they are not shown to be continuous because of safety reasons. For comparison, Fig. 74 shows the cracks on the top surface. It is noted that the cracks extend a considerable distance toward the north end.

Examination of the failure zone shows that indeed failure did occur because of concrete crushing. The most pronounced area of distress occurred on the south edge of the model (Fig. 75). The maximum depth of the failure zone is 2.0 in. (5.08 cm). Cracks extend up from the bottom to meet the region of distress as shown in Fig. 76. Failure occurred across the entire width of the slab as indicated in Fig. 77.

Another interesting event worthy of noting can be seen in Fig. 78. It is observed that the reinforcing steel buckled upward. This probably occurred after the concrete crushed, which relieved the restraint imposed on the reinforcing steel and thus allowed it to buckle. However, buckling may have been occurring earlier in the test; this may explain the reversal in strains occurring in the top reinforcing steel as is mentioned earlier. Several prestressing tendons across the width of the slab under the failed concrete are cut out of the concrete and examined. The metal conduit housing the tendons is carefully removed and the grout exposed. The grout is in perfect condition and a good bond appears to exist. None of the tendons examined are broken.

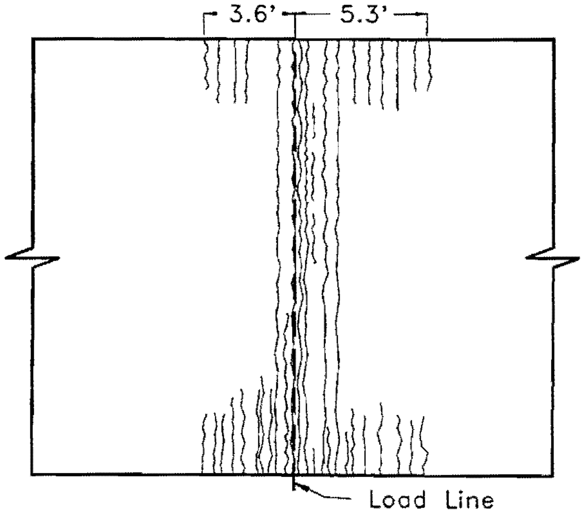

FIG. 73. Cracks on Bottom Surface of Slab Under Load

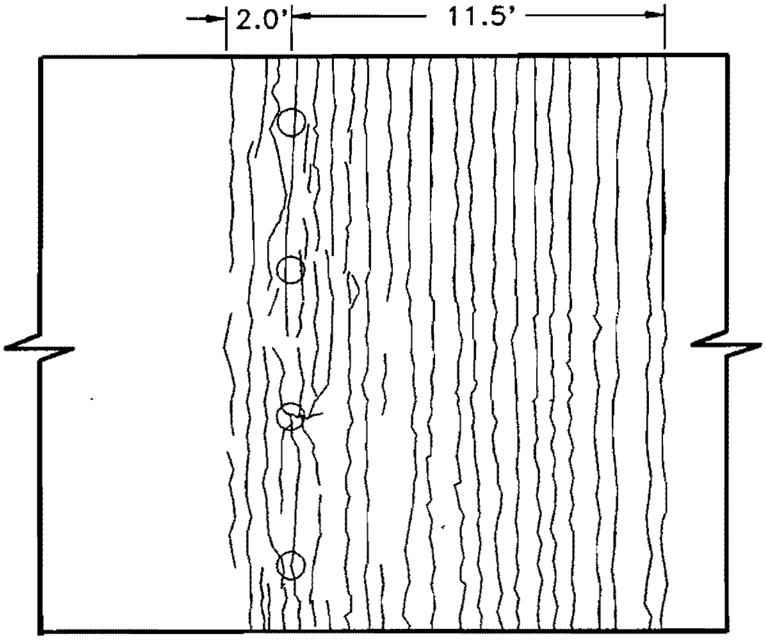

FIG. 74. Cracks on Top Surface of Slab

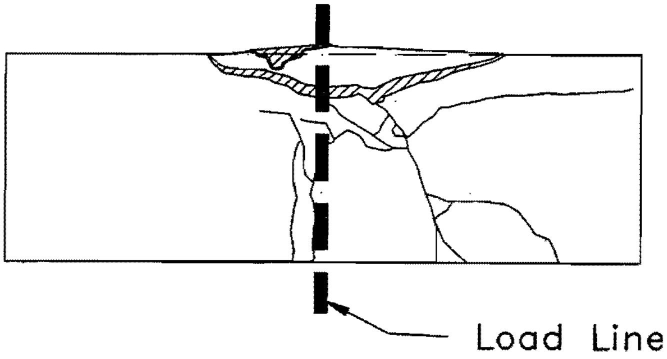

FIG. 75. Crack Pattern on South Edge Failure Region

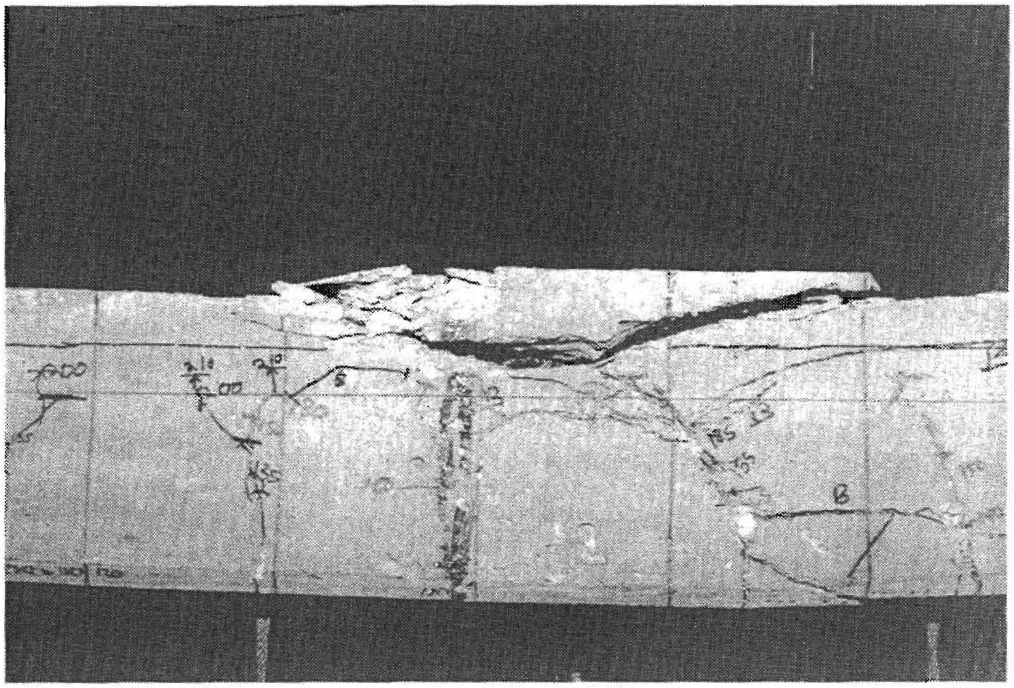

FIG. 76. South Edge Failure Region

FIG. 77. Failure at Load Line Completely Across the Width

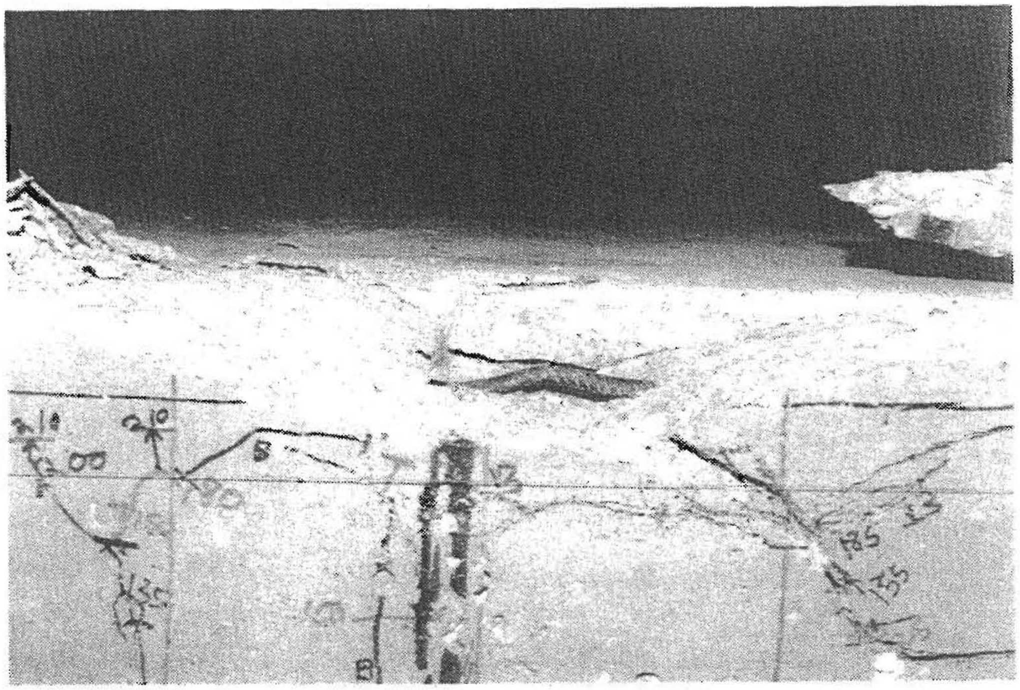

FIG. 78. Buckling of Reinforcing Steel

9.3.2 Negative Moment Failure

After positive moment failure is obtained, a check is made on the reserve capacity of the bridge subject to negative moment loading. Load frames are set up across both spans. The frames are positioned such that loads are applied at a distance of 0.38 and 0.44 of the east and west span lengths, respectively. Two actuators are used per span for this test. Load is distributed to the bridge deck by the spreader beams.

Load is applied to both spans in equal load increments. Testing begins by applying six increments of 10 kips (44.5 kN) per span. Next, three load increments of 5 kips (22.25 kN) per span are added, bringing the load to 75 kips (333.5 kN) per span or 150 kips (667.5 kN) total. On the fourth increment, while attempting to apply 80 kips (356 kN) per span, equilibrium of the actuators could not be maintained at approximately a total load of 154 kips (685.3 kN). Instability was attributed to increasing rotations occurring at the column bent. Loading had to be decreased to acquire equilibrium. Equilibrium is obtained at 140 kips (623 kN), which is comprised of 80 kips (356 kN) and 60 kips (267 kN) on the east and west spans, respectively. Excessive rotation at the column bent increased; this caused crushing of the concrete on the bottom surface of the slab when even small additional load was applied on the west span. Load was held constant on the west span with an attempted increase of load on the east. After several attempts to obtain a higher load, none were successful. As load was increased on the east span, decreasing the load on the west was required to stop the rotation. The maximum load attainable for this load configuration was 154 kips (685.3 kN). A computer simulation was not performed as previously mentioned.

9.3.3 Shear Failure

Even though it is improbable that this type of structure would fail in shear prior to a moment failure, availability of the model and testing apparatus calls for a localized shear test to be performed. As mentioned previously, a test for punch-through shear failure was previously carried out on this type of slab using Model 1 (Roschke and Inoue 1990). Load required to cause a single column to punch through the slab was 207 kips (921 kN). The magnitude of load required to cause a punch-through failure with additional columns is not attainable with the current laboratory equipment. Rather, an attempt to fail the slab in shear along an edge at the column bent is made.

Load frames used for negative moment loading are repositioned so that they straddle the column bent. A cross beam is attached to the two load frames and the two 110-kip (489.5-kN) actuators are fastened side by side to the cross beam. With this configuration, loading can be applied to the edge of the slab at the column line (Fig. 79). Because existing beams are used to construct this load frame, the load applied is not evenly balanced on each side of the column bent. An offset of 2 in. (5.08 cm) toward the left span (west) exists. The model is loaded and the maximum load obtained is 177 kips (787.7 kN). Failure begins with flexure cracks extending out from above the outermost column toward the edge of the slab at a load of 140 kips (623 kN). Cracks continued to grow. The load increment from 170 kips (756.5 kN) to 180 kips (801 kN) could not be imposed. Deflection continued without resistance with any additional increase in load. The failure pattern is shown in Fig. 80. It should be remembered that this testing is done after much previous testing, and the model had many cracks along with damage in the region where the load is applied.

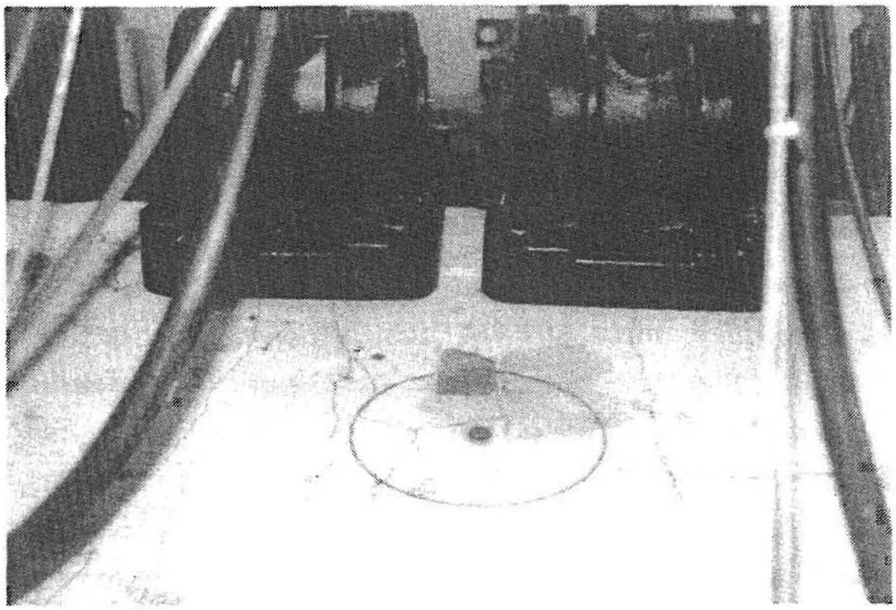

FIG. 79. Experimental Setup Used to Apply Shear Failure Load

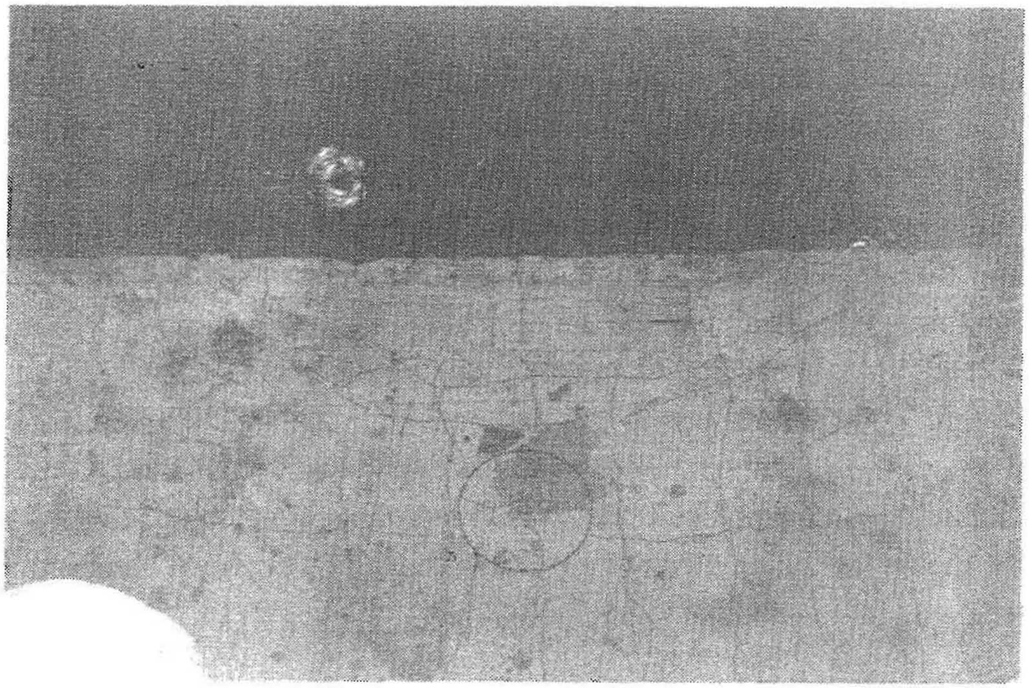

FIG. 80. Crack Path of Shear Failure

9.4 Discussion of Ultimate Loads

Durability and ductility are two words that can be used to describe Model 2. Many loads exceeding the expected capacity are applied and, in turn, cause large deflections and a large number of cracks; however, structural integrity is maintained even after concrete failure occurs. Although the concrete failed by crushing, the prestressing tendons maintain structural integrity and total collapse is avoided. Fig. 81 is a view looking down the edge of the slab during application of ultimate load. The bridge is shown to be rather ductile with deflections of up to 7.0 in. (17.8 cm) being recorded. While this scenario is unlikely to occur at a real bridge site, it is encouraging to note that the slab is ductile and can remain serviceable even under extreme conditions.

Although the ultimate moment equations that were presented earlier are well accepted and can be used to compute the ultimate moment capacity of flexural members, peculiarities associated with continuous flat slab structures are worth examination. The maximum positive and negative moment corresponding to the ultimate recorded load for the positive moment test are 1,590 k-ft (2,152 kN-m) and 950 k-ft (1,285 kN-m), respectively. These values are derived from equilibrium equations using the reactions obtained from the load cells. Capacities computed by Eq. 34 are 1,210 k-ft (1,637 kN-m) and 1,150 k-ft (1,556 kN-m) at the location of applied load and the column bent, respectively. Computation of these moment capacities involves using actual model parameters in some cases. The concrete strength is measured prior to testing and the average compressive strength is found to be 8,000 psi (55 MPa). The depth to the centroid of the steel d is measured to be 7.58 in. (18.3 cm) after all testing has taken place and when the model is sawn apart. More capacity at the load line exists than is computed. This is expected because Model 2 is a continuous structure and Eq. 34 is developed for simple structures.

Continuous prestressed concrete structures have some added complexities that simple structures do not share. The presence of secondary moments that are by-products of prestressing a continuous structure may increase or decrease the capacity (Burns and Lin 1981). For Model 2, secondary moments are small, but when taken into account, increase the positive moment capacity. Also formation of plastic hinges increases the load carrying capacity of continuous structures. In addition to including these parameters, use of a more detailed analysis of the cross-section can further improve accuracy of the results.

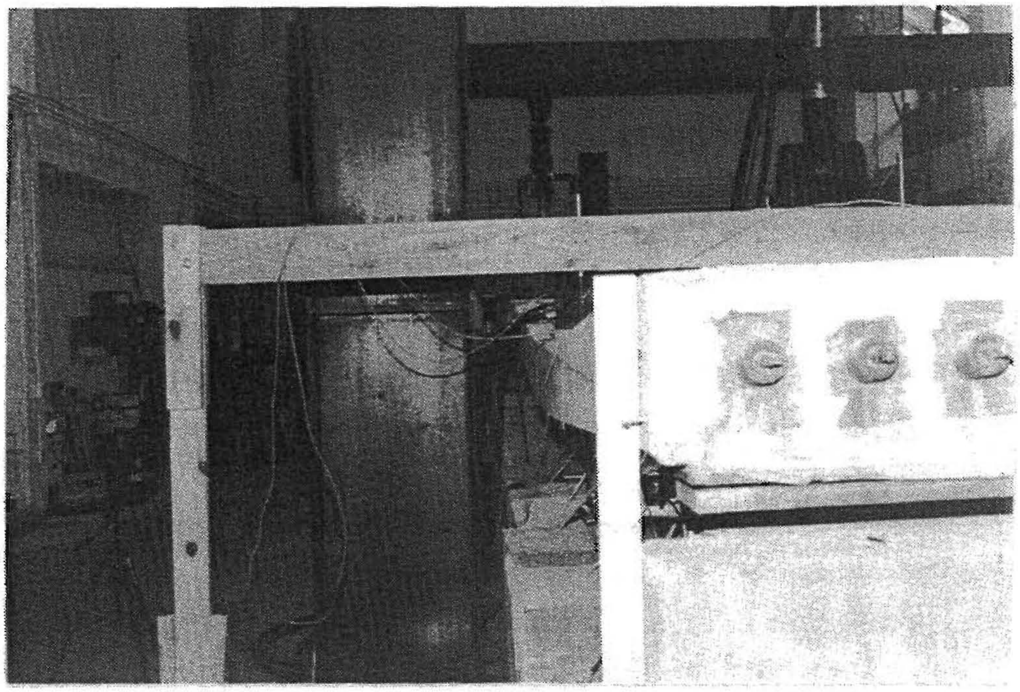

FIG. 81. Deflections Along North Edge During Ultimate Test

Use of the ultimate shear equations for verification of results of the experimental shear test did not yield satisfactory results. Further study of the type of shear failure that occurred is desirable. However, it is noted that the ultimate load of 177 kips (796 kN) could not be feasibly applied on a full-scale structure in the manner in which it is used for this test. Thus, the importance of the test is to further show that this type of shear is not a problem for continuous flat slab bridges.

9.5 Disposal of Materials

After testing of the slab is complete, a circular saw is used to reduce the slab into sections that can be hauled away on a flatbed trailer (see Fig. 82). Inspection of the cross-sections reveals no voids or damage to the grout surrounding the tendons. The large slab sections of concrete are being used as abutments and retaining walls in a county bridge. Concrete blocks used for dead weight and live loadings are serving as traffic control devices in a municipality.

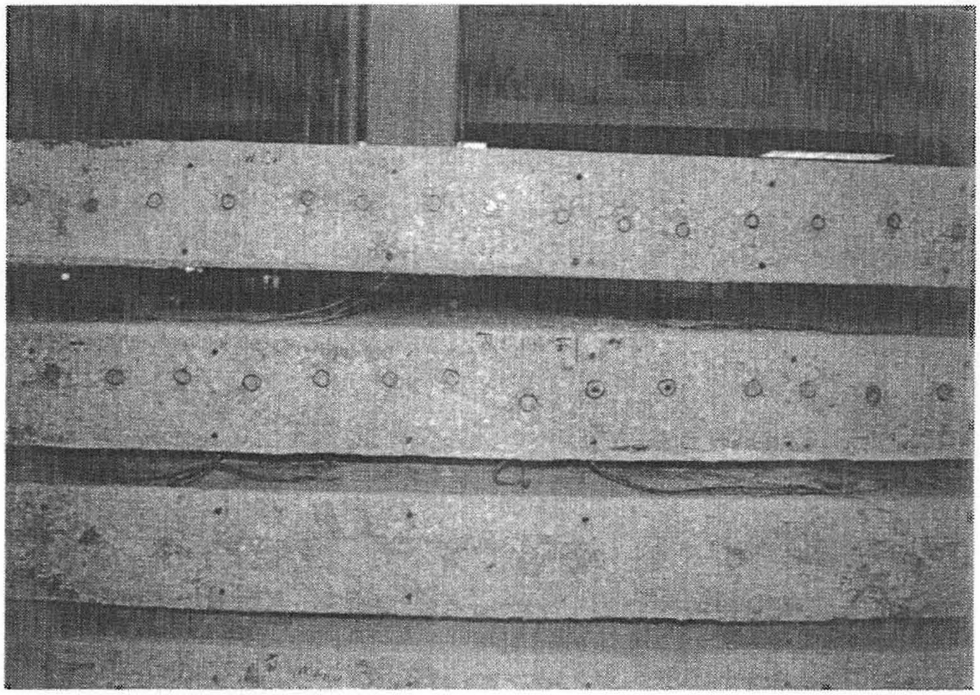

FIG. 82. Edge View of Sections of Slab

10. CONCLUSIONS

A 3/10ths scale model of an existing flat slab bridge existing in Wichita Falls, Texas, was constructed, instrumented, and tested to failure. Time dependent properties of creep and shrinkage were monitored for more than one year. Structural response was observed for a variety of loading conditions. AASHTO design loads were applied to the model and the response was measured. Model 2 was instrumented with 18 LVDTs to measure deflection, 185 foil strain gages attached to the mild reinforcing steel to measure strain, and 10 load cells provided magnitudes of reactions at the supports. Deflections were regularly monitored in order to determine if a change in camber is a problem. By serendipity the model was in an almost perfectly load-balanced condition. Because of this balance, deflections remained small and camber was not a problem for the slab in the laboratory. Compressive strain in the transverse direction was shown to be significantly larger in the center of the banded region than predicted using a one-way strip approach. Dynamic loads were applied in a fashion that simulates the passing of an overloaded AASHTO HS20-44 truck. Loads exceeding design loads were applied at various locations on the bridge and the response was observed. Finally, the model was loaded in several stages to cause an ultimate moment failure. After positive and a negative moment failure, a unique shear test was performed on the edge of the slab at the column bent.

In addition to experimental testing, numerical simulation was performed using the software package *TEXSLAB*. This software was developed for TxDOT with the intent for use in analysis of post-tensioned flat slab bridges. The results originating from the experimental work done in this phase of the project in conjunction with these from Model 1 and the field study were used to verify the accuracy of the analysis code. Numerical modeling correlates well with survey data that shows time-dependent deflections to be small. Strain distributions and, consequently, stress distribution are accurately predicted using FEM and elasticity theory; degree of accuracy is similar to results of analyses carried out on the first laboratory model (Roschke and Inoue 1990). Also, the analysis code successfully uses ACI formulas to compute shrinkage strains, which increases confidence in the simulation capability of the code.

Construction details of the model made study of creep and shrinkage difficult. Because of inappropriate curing conditions, shrinkage was not accurately modeled during the early period of the test program. As time progresses, shrinkage is shown to follow the ACI formula.

Creep strains in the model slab, which have an effect on the long range adequacy of the design, are not accurately predicted using FEM due to the complicated construction sequence necessary to protect the structural integrity of the laboratory slab. However, it is determined that procedures recommended by ACI Committee 209 do adequately predict long term time-dependent effects if the strain history is known. These same procedures are incorporated into the analysis program to predict creep strains (van Gruenen 1979).

Post-tensioned flat slabs such as the prototype for this study are shown to be a viable alternative to satisfy problems with lack of allowable section depth, even for spans up to 100 ft (30 m). Dead load is the primary controlling design load as would be expected. Load balance design with 100% of the dead load balanced gives, in the case of the model in this study, a design that virtually eliminates out-of-plane deflections due to time-dependent effects. As known previously, but worthy of noting: the load-balancing approach to design basically inhibits the problem of excess deflections due to camber. By using the software package *TEXSLAB*, accurate modeling of the prestressing can be carried out and the load-balanced condition is readily obtainable. Of course, the model is a simplification of the prototype structure that has a three-span, skewed deck. Load balancing is more difficult for the latter case.

Shear lag at the edges of the banded region is apparent, but does not cause any adverse effects in the serviceability of the model bridge deck. 200,000 cycles of repetitive loading resulted in no apparent damage in this region, as well as the rest of the deck. However, skew effects, which may increase the shear strains in this area, are not present in the model. Designers should consider reducing the force in the band of transverse tendons and also varying the spacing between tendons from the center of each line of columns. Spreading the tendons would decrease the magnitude of shear lag.

All cases involving dead load, service live load, and fatigue load show small changes in strain that are not a threat to the integrity of the slab. Even 200,000 cycles of a heavy truck passing through a region of high stress gradients resulted in almost no detectable difference in slab response. Application of ultimate positive moment, negative moment, and shear generally show a ductile response. Positive moment capacity of the slab is 31% larger than predicted by an AASHTO equation.

APPENDIX I. REFERENCES

ACI Committee 215 (1974). "Considerations for design of concrete structures subjected to fatigue loading." *ACI Journal*, 71(3), 97-121.

ACI-ASCE Committee 423. (1974). "Tentative recommendations for prestressed concrete flat plates." *ACI Journal*, 71(2), 61-71.

Alami, Z. Y., and Ferguson, P. M. (1963). "Accuracy of models used in research on reinforced concrete." *ACI Journal*, 60(11), 1643-1661.

Branson, D. E., and Christianson, M. L. (1971). "Time dependent concrete properties related to design-strength elastic properties, creep, and shrinkage." *ACI Publication SP-27*, 257-277.

Breen, J. E., Burdet, O., Roberts, C., Sanders, and Wollmann, G. (1991). "Anchorage zone reinforcement for post-tensioned concrete girders," *NCHRP Report 10-29*, Washington, D. C.

Burdet, O. (1990). "Analysis and design of post-tensioned anchorage zones in concrete bridges," thesis presented to The University of Texas, at Austin, Tx., in partial fulfillment of the requirements for the degree of Doctor of Philosophy.

Burns, N. H., and Hemakom, R. (1985). "Test of post-tensioned flat plate with banded tendons." *Journal of Structural Engineering*, ASCE, 111(9), 1899-1915.

Darwin, D., and Pecknold, D. A. (1977). "Nonlinear biaxial stress-strain law for concrete." *Journal of Structural Engineering*, ASCE, 103(EM2), 229-241.

Guyon, Y. (1953). *Prestressed Concrete*, John Wiley and Sons, Inc., New York, N. Y.

Kupfer, H., Hilsdorf, H. K., and Rusch, H. (1969). "Behavior of concrete under biaxial stresses." *ACI Journal*, 66(8), 656-666.

Lin, T. Y., and Burns N. (1981). *Design of prestressed concrete structures*, third edition, John Wiley, Inc., New York, N. Y.

Naaman, A. E. (1982). *Prestressed concrete analysis and design: fundamentals.* McGraw-Hill Co., New York, N. Y.

Okada, K., Okamura, H., and Sonoda, K. (1978). "Fatigue failure mechanism of reinforced concrete bridge deck slabs." *Transportation Research Record No. 664*, Transportation Research Board, 136-144.

Perdikaris, P. C., Beim, S. R., and Bousias, S. N. (1989). "Slab continuity effect on ultimate and fatigue strength of reinforced concrete bridge deck models." *ACI Structural Journal*, 86(4), 483-491.

Phipps, A. R. (1985). "Structural effects of transverse prestressing in bridge decks." *Research Report 316-2*, Center for Transportation Research, The University of Texas at Austin, Austin, Texas.

Poston, R. W., Carrasquillo, R. L., and Breen, J. E. (1987). "Durability of post-tensioned bridge decks." *ACI Materials Journal*, 84(4), 315-326.

Preece, B. W., and Davies, J. D. (1964). *Models for structural concrete*, C. R. Books Ltd, London, United Kingdom.

Roschke, P. N., Epperson, B., and Aftab, S. (1988). "Graphically-Oriented Analysis of Beam Columns with Movable Loads on Microcomputers." *Report No. FHWA/TX-90/1183-1*, Texas Transportation Institute, Texas A&M Univ., College Station, TX.

Roschke, P. N., and Inoue, M. (1991). "Effects of banded post-tensioning in prestressed concrete flat slab." *Report No. FHWA/TX-90/1182-1*, Texas Transportation Institute, Texas A&M Univ., College Station, TX.

Roschke, P. N., and Pruski, K. R. (1992). "Graphically oriented analysis of post-tensioned bridges on microcomputers." *Report No. FHWA/TX-90/1182-4F*, Texas Transportation Institute, Texas A&M Univ., College Station, TX.

Roschke, P. N., Pruski, K. R., and Sripadanna, N. (1992). "Experimental and Analytical Study of a Post-Tensioned Bridge." *Report No. FHWA/TX-90/1182-3*, Texas Transportation Institute, Texas A&M Univ., College Station, TX.

Scordelis, A. C., Lin, T. Y., and Itaya, R. (1959). "Behavior of a continuous slab prestressed in two directions." *Amer. Conc. Inst. J.*, 56(6), 441-459.

Standard specifications for highway bridges. 14th ed. (1989). American association of state highway and transportation officials, Washington, D.C.

Su, E. C. M., and Hsu, T. T. C. (1988). "Biaxial compression fatigue and discontinuity of concrete." *ACI Materials Journal*, 85(3), 178-188.

Troxell, G. E., Rapheal, J. M., and Davis, R. E. (1958). "Long-time creep and shrinkage tests of plain and reinforced concrete." *ASTM Proceedings*, 58, 1101-1120.

Van Greunen, J. (1979). "Nonlinear geometric, material and time dependent analysis of reinforced and prestressed concrete slabs and panels." *Research Report No. UC SESM 79-3*, University of California, Berkeley.

Zia, P., White, R. N., and Vanhorn, D. A. (1970). "Principles of model analysis." *ACI Publication SP-24*, 19-39.

Zienkiewicz, O. C. (1977). *The finite element method*, third edition, McGraw-Hill Co., New York, N. Y.

APPENDIX II. NOTATION

The following symbols are used in this paper:

a = one-half slab thickness;
a' = one-half bearing plate width;
A_c = area of concrete;
A_j = load applied by actuator j;
A_s = area of passive steel reinforcement;
A_{ps} = area of prestressing steel;
C_t = creep coefficient;
C_u = ultimate creep coefficient (determined from experimental data);
D = effective transverse prestressing area;
e = eccentricity of tendon;
E_c = initial tangent modulus of concrete;
E_m = initial tangent modulus of model concrete;
E_p = initial tangent modulus of prototype concrete;
E_{ps} = initial tangent modulus of prestressing steel;
$f_c'(28)$ = compressive strength of concrete at 28 days;
$f_c'(t)$ = compressive strength of concrete at any time t;
f_{ci}' = compressive strength of concrete at initial prestressing operation;
f_{pci} = stress in concrete at time of initial prestressing force;
f_{pu} = ultimate strength of prestressing strand;
f_{sp} = splitting tensile strength;
f_{yps} = 0.1% offset; yield strength of prestressing steel;
f_{ys} = yield strength of reinforcing steel;
F_1 = prestressing force at jacking end;
F_2 = prestressing force at dead end;
f_{1ja} & f_{1jb} = flexibility coefficient at each actuator location for left and right loads;
f^*_{1ja} & f^*_{1jb} = flexibility coefficient at each actuator location for left and right wheel loads;
I = impact fraction;
K_s = correction factor for slump;
K_h = correction factor for the size of the concrete member determined from experimental curves;
K_H = correction factor for relative humidity;

K_t = age at loading correction factor;
L = length in feet of the portion of the span that is loaded to produce the maximum stress in Eq. 24;
L = live load in Eq. 25;
L_m = length dimension of model;
L_p = length dimension of prototype;
p_m = uniform load acting on model;
p_p = uniform load acting on prototype;
$P_{cr_{(plate)}}$ = critical prestressing force for allowable bearing;
P_j = axle load;
P_m = concentrated load acting on model;
P_p = concentrated load acting on prototype;
s = slump in inches;
S_f = stress scale factor;
S_L = geometric scale factor;
sz = minimum dimension of member in inches;
t = time in days;
u_{1a} = deflection of slab at actuator for left load;
u_{1b} = deflection of slab at actuator for right load;
v_m = velocity of vehicle on model;
v_p = velocity of vehicle on prototype;
W = width of slab;
α = accumulated change in angle over the length of the tendon;
$\varepsilon_c(t)$ = strain corresponding to peak stress f_c' at t days after casting;
ε_m = strain in model;
ε_p = strain in prototype;
$\varepsilon_{sh}(t)$ = shrinkage at any time t;
ε_{shu} = ultimate shrinkage strain;
μ = curvature coefficient;
ρ_m = density of model;
ρ_p = density of prototype;
σ_m = stress in model;
σ_p = stress in prototype;
τ = age at loading in days;
θ = slope of tendon at anchor.

APPENDIX III. COMPILATION OF MATERIAL TEST RESULTS

Tables 15 through 20 show results of compression tests on 6 × 12-in. (15.4 × 30.5-cm) cylinders. The cylinders were prepared and tested according to ASTM standards. Cylinders tested at 7, 10, and 14 days show strengths that are lower than predicted by ACI recommended formula for strength versus age (Eq. 13). Lower strengths are caused by inadequate capping material used during testing of the higher strength concrete. Upon increasing the strength of capping material, concrete strengths also increase. Approximate error is found to be 15 - 20% as reported by Davis, Troxell, and Hauck (1982).

TABLE 15. Compressive Strength of Concrete at 7 Days

Batch (1)	Cylinder (2)	Load (lbf) (3)	Stress (psi) (4)	Average Stress (psi) (5)
1	1	101,950	3,606	3,832
	2	120,000	4,244	
	3	103,110	3,647	
2	1	93,910	3,321	3,360
	2	96,110	3,399	
	3	ÄÄ[a]	ÄÄ	
3	1	113,720	4,022	4,085
	2	112,820	3,990	
	3	120,000	4,244	
4	1	95,820	3,389	3,286
	2	90,520	3,201	
	3	92,420	3,269	
5	1	112,380	3,975	3,935
	2	110,130	3,895	
	3	——[a]	——	
6	1	95,940	3,393	3,550
	2	96,572	3,416	
	3	108,630	3,842	

[a] Cylinders did not fail in compression

Note: 1 lbf = 4.45 N; 1 psi = 6.89 kPa

TABLE 16. Compressive Strength of Concrete at 10 Days

Batch (1)	Cylinder (2)	Load (lbf) (3)	Stress (psi) (4)	Average Stress (psi) (5)
1	1	107,960	3,818	3,818
2	1	99,900	3,533	3,533
3	1	99,320	3,513	3,513
4	1	99,020	3,502	3,502
5	1	140,850	4,981	4,981
6	1	137,550	4,865	4,865

Note: 1 lbf = 4.45 N; 1 psi = 6.89 kPa

TABLE 17. Compressive Strength of Concrete at 14 Days

Batch (1)	Cylinder (2)	Load (lbf) (3)	Stress (psi) (4)	Average Stress (psi) (5)
1	1	142,085	5,025	4,653
	2	133,850	4,734	
	3	118,730	4,199	
2	1	179,780	6,358	6,185
	2	170,000	6,013	
	3	ÄÄ[a]	ÄÄ	
3	1	ÄÄ[a]	ÄÄ	5,403
	2	146,450	5,180	
	3	159,100	5,627	
4	1	145,320	5,140	4,310
	2	96,500	3,413	
	3	123,780	4,378	
5	1	133,890	4,735	4,756
	2	140,480	4,968	
	3	129,090	4,566	
6	1	145,170	5,134	4,628
	2	127,370	4,505	
	3	120,020	4,245	

[a] Cylinders did not fail in compression

Note: 1 lbf = 4.45 N; 1 psi = 6.89 kPa

TABLE 18. Compressive Strength of Concrete at 35 Days

Batch (1)	Cylinder (2)	Load (lbf) (3)	Stress (psi) (4)	Average Stress (psi) (5)
1	1	202,047	7,146	7,294
	2	208,310	7,367	
	3	208,341	7,369	
2	1	214,357	7,581	7,474
	2	210,109	7,431	
	3	209,488	7,409	
3	1	202,295	7,155	7,106
	2	208,279	7,366	
	3	192,186	6,797	
4	1	199,070	7,041	7,135
	2	210,140	7,432	
	3	192,186	6,932	
5	1	211,938	7,496	7,037
	2	188,930	6,682	
	3	196,000	6,932	
6	1	178,233	6,304	6,708
	2	195,132	6,901	
	3	195,659	6,920	

Note: 1 lbf = 4.45 N; 1 psi = 6.89 kPa

TABLE 19. Compressive Strength of Concrete at 64 Days

Batch (1)	Cylinder (2)	Load (lbf) (3)	Stress (psi) (4)	Average stress (psi) (5)
	1	222,140	7,857	
1	2	200,325	7,085	7,471
	1	219,826	7,775	
2	2	172,450	6,099	6,937
	1	179,480	6,348	
3	2	197,758	6,994	6,671
	1	214,446	7,584	
4	2	208,945	7,390	7,487
	1	209,342	7,404	
5	2	205,093	7,254	7,037
	1	214,018	7,569	
6	2	198,369	7,016	7,293

Note: 1 lb = 4.45 N; 1 psi = 6.89 kPa

TABLE 20. Compressive Strength of Concrete at 170 Days

Batch (1)	Cylinder (2)	Load (lbf) (3)	Stress (psi) (4)	Average Stress (psi) (5)
	1	200,060	7,076	
1	2	214,915	7,601	7,338
	1	211,689	7,487	
2	2	241,581	8,544	7,878
	3	214,946	7,602	
	1	230,861	8,165	
3	2	231,256	8,179	8,017
	3	217,922	7,707	
4		not available		
5		not available		
	1	202,255	7,153	
6	2	230,667	8,158	7,393
	3	194,168	6,867	

Note: 1 lbf = 4.45 N; 1 psi = 6.89 kPa

APPENDIX IV. OVERLOAD TEST - COMPUTER AND EXPERIMENTAL COMPARISON

As discussed in chapter 8, loads that have larger magnitudes than service loads are applied to the model and data is collected. These loads are called overloads. This testing is done primarily to verify data acquisition and testing procedures. Since data is collected, numerical simulation is also made to compare the experimentally collected values with theoretical values. Four tests are presented. The first test is described in chapter 8. Three additional tests are described in this appendix. Strains that were collected from these tests are listed in the following tables. Moments are computed by assuming uncracked sections and perfect bonding between concrete and reinforcing steel. Figures showing locations of applied loads are also included.

Overload case two consists of applying a single 25-kip (112.5-kN) concentrated load on the west span. The load is located 15 in. (38.1 cm.) from the north edge. Five load increments of 5 kips (22.5 kN) per increment are made to reach the final load. The response is linear. Location of the load is shown in Fig. 83 and the data values are listed in Table 21.

Overload case three represent a negative moment load configuration. A single load is applied on each span. Each load is located 18 in. (45.7 cm) from the north edge. The position of each load is shown in Fig. 70. Two load increments of 10 kips (45 kN) are made to reach 20 kips (90 kN) per load point. The collected data is listed in Table 22.

Likewise, overload case four represents a negative moment load configuration and consists of applying four concentrated loads per span. Positions of the loads are shown in Fig. 71. Three increments of 2.5 kips (11.25 kN), for a total of 7.5 kips per load point are applied. The collected data is shown in Table 23.

Observing the results presented in Tables 21-23, it can be seen that the experimentally collected values correspond well to FEA predictions. These results further verify the accuracy of *TEXSLAB* to analyze flat slab bridges in the linear range. In chapter 9, it is shown that *TEXSLAB* values for displacements closely match deflections measured during ultimate loading. This type of loading caused the structure to behave nonlinearly. Thus, on this basis, nonlinear analysis is also feasible using *TEXSLAB*.

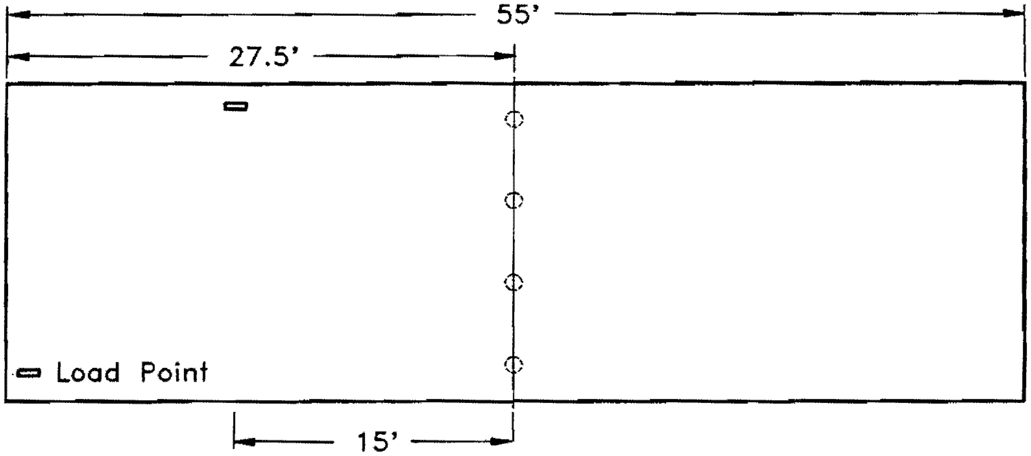

FIG. 83. Load Locations for Overload Test Two

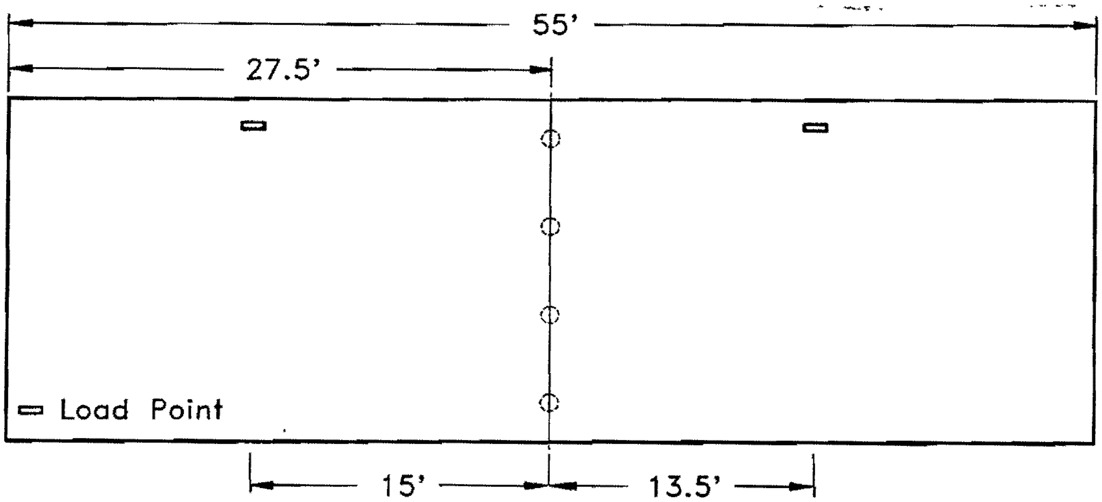

FIG. 84. Load Locations for Overload Test Three

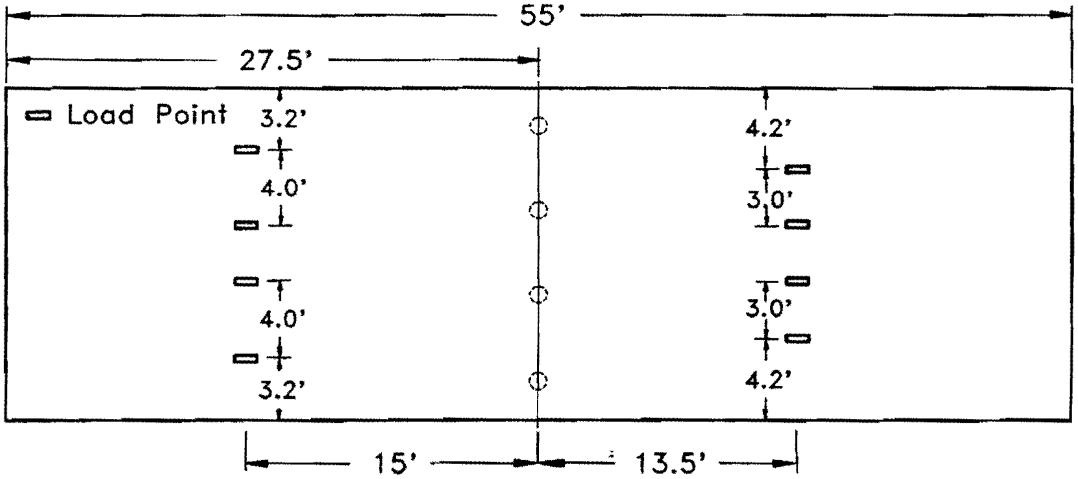

FIG. 85. Load Locations for Overload Test Four

TABLE 21. Strain and Moment Comparison for Overload Case Two

	Experimental Results						FEM Output					
	Strain (με)				Moment (k-in./in.)		Strain (με)				Moment (k-in./in.)	
Gauge (1)	XT (2)	XB (3)	YT (4)	YB (5)	MX (6)	MY (7)	XT (8)	XB (9)	YT (10)	YB (11)	MX (12)	MY (13)
1	-32	40	13	-10	3.9	-1.2	-33	41	10	-13	3.9	-1.1
2	-44	44	22	-23	4.9	-2.2	-41	50	17	-22	4.8	-1.9
3							-54	67	23	-29	6.5	-2.5
4	-66	86	31	-40	8.3	-3.4	-75	94	22	-29	9.1	-2.4
5	-115	152	5	-11	14.5	-0.8	-111	143	0	1	13.6	0.1
6	-17	24			2.4		-22	28	6	-8	2.7	-0.7
7		26			2.9		-28	35	12	-16	3.4	-1.4
8	-36	34			4.1		-34	43	15	-20	4.1	-1.6
9	-36	33			4.1		-39	50	12	-17	4.8	-1.4
10	-34	42			4.4		-42	55	7	-10	5.2	-0.8
11	18	8			-0.5		-8	7	1	-2	0.8	-0.2
12	-5	3			0.5		-7	10	5	-7	0.9	-0.6
13	-3	2			0.3		-7	9	7	-10	0.8	-0.8
14	-2	8			0.7		-5	7	7	-9	0.6	-0.8
15	2	-3			-0.4		-2	2	3	-4	0.2	-0.3
16	8	-5	2	5	-0.8	0.2	3	-7	-4	3	-0.5	0.3
17	11	-11	0	-2	-1.4	-0.1	9	-11	0	0	-1.0	0.0
18	16	-21	1	-2	-2.4	-0.2	16	-21	2	-2	-2.0	-0.2
19	30	-28	4	11	-3.7	0.5	25	-33	3	-4	-3.1	-0.3
20	39	-1	8	-41	-2.4	-2.9	31	-44	3	-3	-3.9	-0.3
21	8	-8	-6	6	-1.1	0.7	5	-9	-5	7	-0.7	0.6
22	14	-18	-3	3	-2.1	0.3	15	-20	-1	2	-1.9	0.2
23	23	-33	-11	1	-3.8	0.7	24	-33	0	1	-3.0	0.1
24	60	-46	-3	0	-6.8	0.2	36	-49	2	-1	-4.5	-0.1
25	101	-75	13	-16	-11.3	-1.7	53	-73	8	-8	-6.7	-0.8
26	14	-14		5	-1.9	0.6	12	-18	-4	6	-1.6	0.5
27	16	-17	-4	4	-2.2	0.5	18	-24	-3	4	-2.2	0.3
28	22	-28	0	1	-3.3	0.0	26	-35	0	1	-3.2	0.1
29	41	-36	3	2	-5.0	-0.1	34	-47	2	-1	-4.3	-0.2
30	55	-44	1		-6.5	0.0	42	-58	1	0	-5.3	-0.1
31	20	-17			-2.5		17	-24	-4	6	-2.2	0.4
32	18	25			0.6		20	-27	-4	5	-2.5	0.4
33	15	-27			-2.8		23	-31	-1	2	-2.9	0.2
34	25	-25			-3.3		26	-35	0	0	-3.3	0.0
35	21	-32			-3.5		31	-41	-4	3	-3.8	0.3
36	13	-20			-2.1		17	-23	-4	5	-2.2	0.4
37	18	-21			-2.5		18	-24	-3	4	-2.3	0.4
38	17	-20			-2.4		19	-25	-2	3	-2.4	0.2
39	23	-22			-2.8		20	-26	-2	1	-2.5	0.1
40	21	-21			-2.7		22	-28	-3	3	-2.7	0.3
41	9	-17	-3	5	-1.6	0.4	13	-18	-3	3	-1.7	0.3
42	10	-16	-2	4	-1.6	0.3	14	-18	-3	3	-1.7	0.3
43	8	-14	-2	3	-1.4	0.3	14	-18	-2	2	-1.7	0.2
44	12	-15	-2	2	-1.7	0.2	15	-18	-2	2	-1.8	0.2
45	9	-13	-2	4	-1.4	0.3	15	-19	-3	3	-1.8	0.3

Note: 1 kip = 4.45 kN.

TABLE 22. Strain and Moment Comparison for Overload Case Three

	Experimental Results						FEM Output					
	Strain (με)				Moment (k-in./in.)		Strain (με)				Moment (k-in./in.)	
Gauge (1)	XT (2)	XB (3)	YT (4)	YB (5)	MX (6)	MY (7)	XT (8)	XB (9)	YT (10)	YB (11)	MX (12)	MY (13)
1	-15	18	8	-5	1.8	-0.7	-15	18	6	-7	1.8	-0.6
2	-25	24	16	-17	2.7	-1.6	-21	25	11	-15	2.5	-1.2
3							-31	39	16	-20	3.7	-1.7
4	-51	56	21	-27	5.9	-2.3	-48	60	14	-18	5.8	-1.6
5	-82	102	5	-7	10.0	-0.5	-75	96	-3	4	9.1	0.4
6	-3	4			0.4		-4	3	2	-2	0.4	-0.2
7		7			0.8		-7	8	7	-9	0.8	-0.8
8	-10	12			1.3		-11	14	9	-13	1.3	-1.1
9	-13	12			1.5		-14	18	8	-11	1.7	-0.9
10	-11	16			1.6		-15	20	3	-4	1.9	-0.3
11	19	-7			-1.6		8	-14	-3	3	-1.2	0.3
12	13	-19			-2.1		11	-15	0	-1	-1.4	-0.1
13	7	-16			-1.5		14	-18	4	-5	-1.7	-0.4
14	22	-10			-2.0		18	-24	5	-7	-2.2	-0.6
15	24	-27			-3.3		24	-33	-1	1	-3.1	0.1
16	17	-16	-7	7	-2.1	0.8	13	-20	-7	8	-1.7	0.7
17	24	-5	-5	-5	-1.8	0.0	22	-29	-3	4	-2.7	0.3
18	31	-38	4	5	-4.5	0.1	34	-46	1	0	-4.3	0.0
19	52	-47	3	1	-6.4	-0.1	49	-66	3	-4	-6.1	-0.3
20	65	-17	72	-64	-5.0	-7.6	60	-83	3	-2	-7.6	-0.3
21	10	-12	-6	8	-1.5	0.8	9	-14	-8	11	-1.3	0.9
22	21	-27	-5	5	-3.1	0.6	24	-33	-2	4	-3.0	0.3
23	28	-24	-4	3	-3.4	0.4	39	-53	-1	1	-4.9	0.1
24	81	-49	-11	0	-8.3	0.6	59	-80	3	-2	-7.4	-0.2
25	144	-114	18	-23	-16.7	-2.3	86	-119	13	-14	-10.9	-1.3
26	17	-14	-28	7	-2.0	1.9	13	-18	-5	7	-1.6	0.6
27	21	-19	-4	-3	-2.6	0.0	20	-28	-2	3	-2.6	0.2
28	26	-30	2	-1	-3.7	-0.2	32	-44	2	-2	-4.1	-0.2
29	53	-48	3	-1	-6.6	-0.2	46	-63	5	-5	-5.8	-0.5
30	73	-61	6		-8.8	-0.6	58	-80	4	-4	-7.3	-0.4
31	7	13			0.5		7	-10	-1	2	-0.9	0.1
32	9	-5			-0.9		8	-11	2	-3	-1.1	-0.2
33	5	-8			-0.8		11	-15	6	-7	-1.4	-0.6
34	9	-12			-1.4		14	-18	7	-8	-1.7	-0.7
35	14	-17			-2.1		19	-26	0	-1	-2.4	0.0
36	-3	12			0.9		-6	6	3	-4	0.6	-0.3
37	-12	24			2.3		-9	11	8	-10	1.1	-0.9
38	-12	13			1.6		-16	20	12	-15	1.9	-1.3
39	-21	21			2.6		-22	28	10	-13	2.6	-1.1
40	-13	20			2.1		-25	33	4	-6	3.1	-0.5
41	-10	18	4	-6	1.7	-0.5	-15	18	6	-7	1.8	-0.6
42	-17	29	10	-20	2.8	-1.7	-21	25	11	-14	2.5	-1.2
43	-21	37	12	-21	3.5	-1.9	-31	38	16	-20	3.7	-1.7
44	-46	66	18	-31	6.8	-2.7	-48	60	14	-18	5.8	-1.5
45	-69	90	6	-3	9.6	-0.5	-72	92	-2	3	8.8	0.2

Note: 1 kip = 4.45 kN.

TABLE 23. Strain and Moment Comparison for Overload Case Four

	Experimental Results						FEM Output					
	Strain (με)				Moment (k-in./in.)		Strain (με)				Moment (k-in./in.)	
Gauge (1)	XT (2)	XB (3)	YT (4)	YB (5)	MX (6)	MY (7)	XT (8)	XB (9)	YT (10)	YB (11)	MX (12)	MY (13)
1	-56	75	10	-11	7.1	-1.1	-54	63	6	-7	6.3	-0.7
2	-66	69	5	-7	7.5	-0.5	-56	65	1	-1	6.5	-0.1
3							-58	68	-3	4	6.8	0.3
4	-48	66	3	-9	6.2	-0.6	-55	66	1	-1	6.5	-0.1
5	-54	67	8	-13	6.6	-1.0	-52	63	6	-7	6.2	-0.6
6	-11	17			1.6		-17	21	2	-2	2.0	-0.2
7		17			0.9		-16	20	-1	0	2.0	0.1
8	-15	15			1.8		-16	20	-2	2	1.9	0.2
9	-14	15			1.7		-16	21	-1	0	1.9	0.1
10	-12	17			1.7		-17	22	2	-3	2.1	-0.3
11	27	-8			-2.2		21	-34	-3	6	-3.4	0.5
12	24	-22			-2.9		22	-31	-2	2	-3.2	0.2
13	15	-23			-2.5		22	-30	-1	0	-3.2	0.1
14	22	-18			-2.5		22	-30	-1	2	-3.2	0.2
15	20	-27			-3.1		21	-32	-3	5	-3.2	0.4
16	64	-62	-9	7	-8.1	0.8	50	-63	-5	11	-6.9	0.9
17	51	-38	4	6	-5.7	0.1	52	-62	-2	1	-6.9	0.1
18	47	-59	11	4	-6.9	-0.3	53	-62	-2	-4	-7.0	-0.1
19	55	-50	-2	8	-6.8	0.6	52	-61	-2	0	-6.9	0.1
20	54	-2	1	-50	-3.4	-3.0	49	-62	-4	11	-6.8	0.8
21	77	-77	-7	11	-10.0	1.1	64	-46	-1	15	-6.7	0.9
22	63	-72	-15	9	-8.9	1.4	64	-52	-2	0	-7.1	0.1
23	54	-79	-13	8	-8.8	1.2	63	-54	-4	-4	-7.2	0.0
24	96	-65	-17	7	-10.3	1.3	64	-51	-2	0	-7.0	0.2
25	93	-81	-4	-5	-11.4	-0.1	63	-46	0	16	-6.7	0.8
26	-53	55	-9	12	7.2	1.2	48	-61	-5	11	-6.7	0.8
27	-44	40	-3	5	5.5	0.4	50	-60	-2	0	-6.7	0.1
28	-52	44	1	4	6.3	0.2	51	-61	-2	-4	-6.9	-0.1
29	-51	59	-1	8	7.3	0.5	49	-61	-2	1	-6.7	0.2
30	-50	62	-6		7.4	0.3	48	-61	-4	11	-6.6	0.8
31	17	-14			-2.1		16	-25	-2	5	-2.5	0.4
32	7	-14			-1.4		17	-24	-2	3	-2.5	0.3
33	11	-19			-2.0		18	-26	-2	2	-2.7	0.3
34	11	-17			-1.9		17	-24	-2	4	-2.5	0.3
35	-4	-16			-0.8		17	-25	-3	5	-2.6	0.4
36	-16	28			2.8		-23	27	3	-2	3.0	-0.3
37	-26	20			2.9		-22	26	-3	5	2.9	0.4
38	-19	20			2.5		-21	27	-5	7	2.9	0.6
39	-20	22			2.7		-21	26	-3	5	2.9	0.4
40	-16	2			1.1		-22	27	2	-3	3.0	-0.3
41	-38	71	8	-11	6.6	-1.0	-50	58	7	-8	6.6	-0.8
42	-49	86	-1	10	8.1	0.6	-55	64	-5	7	7.2	0.6
43	-42	72	-1	7	6.9	0.5	-57	65	-6	7	7.4	0.7
44	-54	85	-2	9	8.4	0.6	-55	64	-5	6	7.2	0.6
45	-42	57	9	-10	6.0	-1.0	-49	59	7	-8	6.5	-0.8

Note: 1 kip = 4.45 kN.